FOSSIL ENERGY

DOE/BC/14940-5
(DE96001285)

ECONOMIC RECOVERY OF OIL TRAPPED AT FAN MARGINS USING HIGH ANGLE WELLS AND MULTIPLE HYDRAULIC FRACTURES

Annual Report
September 28, 1995 to September 27, 1996

By
Bruce L. Niemeyer

September 1997

Performed Under Contract No. DE-FC22-95BC14940

Atlantic Richfield Company
Bakersfield, California

National Petroleum Technology Office
U. S. DEPARTMENT OF ENERGY
Tulsa, Oklahoma

DISCLAIMER

This report was prepared as an account of work sponsored by an agency of the United States Government. Neither the United States Government nor any agency thereof, nor any of their employees, makes any warranty, expressed or implied, or assumes any legal liability or responsibility for the accuracy, completeness, or usefulness of any information, apparatus, product, or process disclosed, or represents that its use would not infringe privately owned rights. Reference herein to any specific commercial product, process, or service by trade name, trademark, manufacturer, or otherwise does not necessarily constitute or imply its endorsement, recommendation, or favoring by the United States Government or any agency thereof. The views and opinions of authors expressed herein do not necessarily state or reflect those of the United States Government.

This report has been reproduced directly from the best available copy.

Available to DOE and DOE contractors from the Office of Scientific and Technical Information, P.O. Box 62, Oak Ridge, TN 37831; prices available from (615) 576-8401.

Available to the public from the National Technical Information Service, U.S. Department of Commerce, 5285 Port Royal Rd., Springfield VA 22161

DOE/BC/14940-5
Distribution Category UC-122

Economic Recovery Of Oil Trapped At Fan Margins Using High Angle Wells And Multiple Hydraulic Fractures

Annual Report
September 28, 1995 to September 27, 1996

By
Bruce L. Niemeyer

September 1997

Work Performed Under Contract No. DE-FC22-95BC14940

Prepared for
BDM-Oklahoma/
U.S. Department of Energy
Assistant Secretary for Fossil Energy

Jerry Casteel, Project Manager
National Petroleum Technology Office
P.O. Box 3628
Tulsa, OK 74101

Prepared by:
Atlantic Richfield Company
PO Box 147
Bakersfield, California 93302

Table of Contents

List of Figures V

List of Tables VIII

Abstract IX

Introduction 1

Discussion 2

Fracture Treatment Design 2

Design Hydraulic-Fracture Treatment for Test Well and Microseismic-Logging Program for Monitor Well 2

Test Well Selection 2

Local Geology 2

Rock and Mechanical Properties 2

Fracture Azimuth 3

Frac Test Well and Run Microseismic Logs 3

Pump-In Test 3

Data Frac 3

Propped Frac 4

Microseismic Logging 4

Post-Frac Production 5

Fan Margin Characterization and Modeling 6

Geologic Framework 6

Reservoir Compartments 7

Petrophysical Description and Flow Unit Refinement 7

Core Data 7

RFT Data 9

Log Data 9

Flow Unit Refinement 10

Summary of Results 11
Reservoir Modeling 12
Model Grid 12
Areal Grid Definition 12
Layering 12
Local Grid Refinement 12
Gridblock Properties 12
Incorporation of Geologic Model 12
Capillary Pressure 13
Relative Permeability 13
PVT Properties 13
History Matching 13
Regional Match 14
Well Match 14
Flow Unit Match 15
Performance Forecasts 15
Continued Operations 15
North-South Fractured Slant Well 15
East-West Fractured Slant Well 16
Vertical Wells 16
Horizontal Well 17
Number of Fractures 17
Analytical Estimates of Reserves and Initial Rates 17
Development Strategy 18
Project Economics 18
Economic Input 18
Decision Tree Analysis 18
Costs to Drill, Complete, and Operate 18
Production 19
Product Prices 19
Tax Rates 19
Results 19

Technology Transfer 20
Project Evaluation Report 20
Open File 20
Technical Papers, Presentations, Workshops 20

References 21

List of Figures

Figure 1: Map of Yowlumne Field Showing Test Well and Monitor Well

Figure 2: Structure Map of the N-Point Marker Showing Test Well and Monitor Well

Figure 3: North-South Cross-Sectional Schematic Depicting Test Well and Monitor Well

Figure 4: Type Log of Test Well Identifying Flow Units

Figure 5: S_{Hmax} from Borehole Breakout Data

Figure 6: Treating Pressures and Rates from Test Well Pump-In Test

Figure 7: Treating Pressures and Rates from Test Well Data Frac

Figure 8: Post Data Frac Gamma Ray / Temperature Log on Test Well

Figure 9: Treating Pressures and Rates from Test Well Propped Frac

Figure 10: G Function Plot of Test Well Propped Frac Pressure Decline

Figure 11: Directional Surveys of Test Well and Monitor Well (Plan View)

Figure 12: Microsiesmic Events Recorded in Monitor Well (Plan View)

Figure 13: Test Well Production Plot

Figure 14: Map of California Showing Location of the San Joaquin Valley in Relation to Other Oil-Producing Basins in the State

Figure 15: Stratigraphic Section for the Southern San Joaquin Valley Basin Showing the Monterey-Stevens Petroleum System

Figure 16: Map of California Showing the Principle Geomorphic Provinces Surrounding the Southern San Joaquin Basin

Figure 17: Map of the Southern San Joaquin Basin Showing the Distribution of Three Main Depositional Systems Represented by the Stevens Sandstone

Figure 18: Structure Map Drawn on the N-Point Marker Showing the Relationship of Units A and B to the Yowlumne Field Anticline

Figure 19: Map Showing Left-Stepping and Basinward-Stepping Geometries Exhibited by Depositional Lobes that Compose the Yowlumne Fan

Figure 20: East-West Cross-Section Showing the Five Main Reservoir Layers in Unit B Penetrated by the Proposed Slant Well

Figure 21: Cross-Section Showing the Left-Stepping Geometry of the Five Main Reservoir Layers in Unit B

Figure 22: Reservoir Compartments in the Yowlumne Sand in Well 72X-4 Indicated by Pressure Variations in an RFT Survey
Figure 23: Plot of Reservoir Quality Index vs. Pore Ratio for Well 55X-34 Showing Hydraulic Unit Grouping
Figure 24: Hydraulic Units in Well 55X-34
Figure 25: Crossplot of Permeability vs. Porosity for Well 55X-34 Grouped by Hydraulic Unit
Figure 26: Degree of Sorting Indicated by Shape of Mercury Injection Curves
Figure 27: RFT Pressure Gradients for Well 57X-34
Figure 28: Type Log of Well 38X-34RD Showing Five Main Reservoir Layers
Figure 29: Type Log of Well 27X-34 Showing Subdivision of Five Main Reservoir Layers into Ten Layers
Figure 30: Crossplot of Core Permeability (Air) to Porosity
Figure 31: Histogram Showing Frequency of Hydraulic Units in the Yowlumne Sandstone
Figure 32: Cumulative Capacity Plot of Air Permeability
Figure 33: Cumulative Capacity Plot of Effective Porosity
Figure 34: Map of Gross Sand Thickness
Figure 35: Map of Net-to-Gross Sand Ratio
Figure 36: Map of Effective Porosity of Net Sand
Figure 37: Map of Liquid Permeability of Net Sand
Figure 38: Steamline Map Showing Original North-South Slant Well
Figure 39: Areal Location of Partial Field Model Grid
Figure 40: Partial Field Model Grid with Local Grid Refinement
Figure 41: Log and Core J-Functions
Figure 42: Water-Oil Relative Permeability
Figure 43: Gas-Oil Relative Permeability
Figure 44: History Match of Model Area Production Rates
Figure 45: History Match of Model Area Pressure
Figure 46: Water-Oil Pseudo Relative Permeability
Figure 47: History Match of Well 57X-34 Pressure Profile
Figure 48: History Match of Well 38X-34RD Water Saturation Profile

Figure 49: Comparison of Incremental Production Rates for East-West Slant Well and North-South Slant Well

Figure 50: Comparison of Incremental Production Rates for 3 Vertical Wells, East-West Horizontal Well, and East-West Slant Well

Figure 51: Decision Tree Used with Economic Analysis

Figure 52: Sensitivity of Incremental Production Rates to the Number of Fracs for East-West Slant Well

Figure 53: Incremental Production Rate and Recovery for East-West Slant Well (Expected Values)

List of Tables

Table 1: Rock Properties Used for Frac Design of Test Well

Table 2: Mechanical Properties Used for Frac Design of Test Well

Table 3: Cores from Project Area Used in Study

Table 4: Porosity-Permeability Data from Conventional Core Analysis for Well 55X-34

Table 5: Calculation of Pore Throat Diameters from Capillary Pressure Data

Table 6: Ranges of $Log_{10}FZI$ Used to Define Hydraulic Units in Project Study Area

Table 7: Effect of Overburden Pressure on Porosity and Permeability

Table 8: Summary of Reservoir Characteristics of the Yowlumne Sand

Table 9: Model Fluid Property Table Based on Black Oil Study of Sample from Well 32-3

Table 10: Cost Estimate to Drill, Complete, and Equip Slant Well

Table 11: Slant Well Operating Expense Estimate

Abstract

The distal fan margin in the northeast portion of the Yowlumne field contains significant reserves but is not economic to develop using vertical wells. Numerous interbedded shales and deteriorating rock properties limit producibility. In addition, extreme depths (13,000 ft) present a challenging environment for hydraulic fracturing and artificial lift. Lastly, a mature waterflood increases risk because of the uncertainty with size and location of flood fronts.

This project attempts to demonstrate the effectiveness of exploiting the distal fan margin of this slope-basin clastic reservoir through the use of a high-angle well completed with multiple hydraulic-fracture treatments. The combination of a high-angle (or horizontal) well and hydraulic fracturing will allow greater pay exposure than can be achieved with conventional vertical wells while maintaining vertical communication between thin interbedded layers and the wellbore. The equivalent production rate and reserves of three vertical wells are anticipated at one-half to two-thirds the cost.

An analogous well was hydraulically fractured to obtain fracture-treatment design parameters for the proposed high-angle well. This well was the first frac in the northwest fan margin, and it treated with a higher frac gradient (1.06 psi/ft) than the 0.91 psi/ft gradient observed in the northeast fan margin (where the high-angle well is proposed to be drilled).

Microseismic events were passively monitored during the frac from an offset well to determine fracture geometry and azimuth. A NW-SE azimuth was detected, compared to the expected NNE-SSW azimuth. Knowledge of fracture azimuth was useful for determining location and azimuth of the high-angle well.

The reservoir geology of the northeast fan margin was re-evaluated. Petrophysical properties were derived from core, log, and RFT data. In general, only slight modifications of previous interpretations were necessary. As expected, rock properties were shown to deteriorate in a easterly direction, towards the distal margin.

The five major flow units were subdivided into ten layers. Rock properties were calculated and mapped for each layer. The detailed reservoir geology was then inserted in a fine-grid, partial-field reservoir simulation model. The model was history matched, with some layers appearing to be more swept than expected.

Upon completion of history matching, the model was used to test a variety of development alternatives aimed at optimizing project economics. Model forecasts compared slant well performance to more conventional development options and quantified rate impacts from changes in well location, orientation, and completion technique. An east-to-west slant well with multiple hydraulic fractures proved to be the optimal alternative to develop the fan-margin region. Model results indicated the well could initially produce 2180 BOPD and recover 724 MBO of reserves (net of interference).

Introduction

The Yowlumne field is a giant field in the southern San Joaquin basin, Kern County, California. It is a deep (13,000 ft) waterflood operation that produces from the Miocene-aged Stevens Sand. The reservoir is interpreted as a layered, fan-shaped, prograding turbidite complex containing several lobe-shaped sand bodies that represent distinct flow units.

Although a high ultimate recovery factor is expected, significant undrained oil still exists at the fan margins. The fan margins are not economic to develop using vertical wells. Numerous interbedded shales and deteriorating rock properties limit producibility. In addition, depth presents a challenging environment for hydraulic fracturing and artificial lift. Lastly, a mature waterflood increases risk because of the uncertainty with size and location of flood fronts.

This project attempts to demonstrate the effectiveness of exploiting the northeast distal fan margin through the use of a high-angle well completed with multiple hydraulic-fracture treatments. The high-angle well will offer greater pay exposure than can be achieved with vertical wells. The hydraulic-fracture treatments will establish vertical communication between thin interbedded layers and the wellbore. The equivalent production rate and reserves of three vertical wells are anticipated at one-half to two-thirds the cost.

This paper is primarily focused on three major activities, which were completed in preparation for the proposed high-angle well:

(1) An analogous well was hydraulically fractured to obtain fracture-treatment design parameters. Microseismic events were passively monitored from an offset well to determine frac geometry and azimuth. Knowledge of frac azimuth was useful for determining location and azimuth of the high-angle well.

(2) The reservoir geology of the northeast fan margin was re-evaluated. Petrophysical properties were derived from core, log, and RFT data. Existing flow units were subdivided into thinner layers and petrophysical properties were calculated for each layer. The petrophysical properties were then mapped by layer.

(3) The final activity included incorporating the detailed reservoir geology of the fan margin into a fine-grid, partial-field reservoir simulation model. The model was then used to optimize well location, azimuth, and completion strategy.

Discussion

Fracture Treatment Design

An existing well in the field was hydraulically fractured to obtain relevant treatment-design parameters for the proposed slant well.

Design Hydraulic-Fracture Treatment for Test Well and Microseismic-Logging Program for Monitor Well

Test Well Selection

Yowlumne Unit B 84-32, located in the northwest portion of the field, was selected as the test well to be hydraulically fractured (Fig. 1). It has the highest deviation angle of wells located in a similar fan-margin setting to the proposed slant well. Offset water injection well 86-32 was chosen to monitor the frac with microseismic logging tools.

Local Geology

The Yowlumne sand drapes across the north flank of the San Emidio structural nose. In the vicinity of the test well, bedding planes dip approximately 20° to the north (Fig. 2).

A reverse fault separates the test well and monitor well. The test well is on the downthrown side of the fault, which is separated vertically from the upthrown block by 50 ft or less (Fig. 3). Production and pressure data indicate that the fault blocks are in at least partial communication.

The Yowlumne sand is approximately 200 ft thick at the test well location. It is bounded by siliceous shales and is internally subdivided into six flow units (Fig. 4). Correlation of flow units is difficult in the fan margin, as sand packages break up and become interbedded.

Rock and Mechanical Properties

Openhole logs were used to determine interval thicknesses and rock properties, such as shale volume, porosity, and water saturation. Permeability was estimated using porosity-permeability relationships from core data elsewhere in the field. These parameters are shown in Table 1.

Full-wave sonic log data and hydraulic-fracture treating pressures from other wells in the field were used to estimate mechanical properties for the Yowlumne sand and bounding shales[1]. These data were used to predict stress profiles for the test well (Table 2) based upon the following assumptions for pore pressure: (1) no pore-pressure variation by layer, and (2) permeability-thickness weighted-average variation of pore pressures by layer. Pore-pressure variation by layer was the best representation. However, both assumptions

indicated that the frac gradient would fall between 0.9 and 1.0 psi/ft and that frac height would be confined to the Yowlumne sand by the overlying and underlying shales.

Although this technique of estimating the stress profile is often used for tectonically relaxed environments, it is theoretically inappropriate for strike-slip regimes with strong compressional forces[1], such as in the Yowlumne Field. However, it was still useful for observing the relative impact of pore pressures on fracture height.

Fracture Azimuth

Borehole breakouts identified from four-arm dual-caliper dipmeter logs were used to estimate regional stress orientation. Borehole deformations were assumed to be the result of differential horizontal stresses. The azimuth of the shorter axis measured by the dual caliper was assumed to coincide with the direction of maximum horizontal stress[2] (S_{Hmax}).

Breakouts from 12 wells were identified in the reservoir interval (Fig. 5). Eight indicated S_{Hmax} is oriented NNE-SSW. Breakouts from four wells indicated a WNW-ESE S_{Hmax} orientation.

Regional breakout data from surrounding fields suggest the S_{Hmax} is oriented north-south[3], consistent with local fold axes and reverse faulting (including the reverse fault between the test well and monitor well). Therefore, the hydraulic fracture in the test well was expected to propagate NNE-SSW, perpendicular to the reverse fault.

Frac Test Well and Run Microseismic Logs

Prior to pumping the propped-fracture treatment, pump-in/shut-in tests, a reverse step rate test, and a data frac were planned to finalize the frac design for the test well.

Pump-In Test

A pump-in test was performed on the test well using 2% potassium chloride (KCl) water. The objective was to achieve a pump rate of 30 BPM and observe pressure response. However, a maximum pump rate of only 10 BPM could be achieved due to high surface treating pressures (Fig 6). Converting the surface instantaneous shut-in pressure (ISIP) to bottomhole, a frac gradient of 1.05 psi/ft was approximated, much higher than the expected 0.93 psi/ft gradient. Analysis of the pressure decline after shut-in for fracture closure pressure was inconclusive.

Using the same fluid, a reverse step-rate test was attempted to obtain estimates of perforation friction and near-wellbore tortuosity. However, sufficient rate could not be achieved to establish the number of steps required for analysis (Fig. 6).

Data Frac

A data frac was pumped using a linear gel fluid (the same fluid type used as pad in the propped-frac) and no proppant. Once again, a pump rate of 30 BPM was planned, but

only 16 BPM could be achieved due to high surface-treating pressures (Fig. 7). A frac gradient of 1.05 psi/ft and a leakoff coefficient of 0.014 ft/min$^{1/2}$ were calculated.

Fluid pumped during the data frac was tagged with a radioactive isotope (Scandium-46). Temperature and gamma ray logs run immediately after the treatment indicated nearly all the fluid exited the wellbore within a 40 ft section near the base of the 200 ft reservoir interval (Fig. 8). Only a small portion of the gross vertical section appeared to have been stimulated. However, an interpretation based solely on log data might have understated the vertical extent of the fracture, since the fracture possibly grew in a different vertical plane than the north-south plane containing the deviated wellbore. Therefore, the fracture may have not intersected the well over its entire height.

Propped Frac

The initial design of the propped-fracture treatment was adjusted to account for lower injection rates, greater leakoff, and reduced frac growth. The design frac height and half-length were reduced to 60 ft and 185 ft, respectively.

The well was treated with 65,000 gals of crosslinked guar gel containing 145,000 lbs of sintered bauxite (Fig 9). Early in the job, pump rate was limited to approximately 2 BPM due to high treating pressures. As proppant concentration was increased, pump rates began to improve. A pump rate of 22 BPM was achieved for much of the job, with surface-treating pressures falling from 10,000 psi to slightly under 9000 psi.

The frac pressure decline was evaluated with a Nolte G function plot[4] (Fig. 10). The results were in line with those from the pump-in tests and data frac. A high frac gradient (1.06 psi/ft) and a high leakoff coefficient (0.013 ft/min$^{1/2}$) were calculated. Fracture net pressure was determined to be 1500 psi, approximately 1000 psi higher than expected. The higher net pressure could be an indication of a more confined frac.

Commercial fracture-stimulation software was used to model actual treating data. The modeling indicated that the propped fracture half-length might have approached 700 ft. However, embedment could have decreased fracture conductivity such that the effective propped fracture half-length was reduced to approximately 100 ft. Although the effective propped fracture height near the well was approximately 80 ft, the upper one-half of the frac might have been isolated from the lower half by a 15 ft shale break.

Microseismic Logging

Microseismic logging was used to detect microseismic activity created by the hydraulic-fracture treatment in the test well and estimate azimuth, geometric shape, and location of the fractured zone[5]. These data would then be used for siting the proposed slant well location, determining the well azimuth, and designing the hydraulic-fracture treatments.

A three-component geophone sonde was locked onto the casing of the monitor well at a depth of 11,930 ft TVD. The sonde was located approximately 1020 ft above and 1050 ft south of the test well perforations (Figs. 3 and 11). Perforation shots were fired in the test

well to orient the geophone and calibrate the velocity factor used to calculate the distance from the geophone to the source. Microseismic events were passively monitored during the pump-in test, data frac, and propped frac. The detected signals were analyzed for the direction of approach of the P-wave and for the time between arrivals of the P-wave and the S-wave. The analysis assumed a straight line path for the seismic wave from the source to the receiver and a constant velocity structure over the ray path. The back azimuth of the P-wave arrival was taken as direction. The distance from the source to the receiver was estimated by the time between the P-wave arrival and the S-wave arrival and a velocity factor (23.4 ft/ms based upon perf shots). Knowing direction and distance, the coordinates of the source were estimated.

Many events were detected during each of the fracturing activities conducted on the test well. These events were projected onto a horizontal plan view (Fig. 12). The microseismic logging tool is referenced to the origin of the plot, and the test well is located near the center of the plot (where the perf shots are shown).

The data suggest that the fracture was not a single planar fracture. Instead, one fracture wing appeared to be considerably longer than the other. The primary azimuth was NW-SE, compared to the NNE-SSW expected azimuth. Interestingly, the seismic events moved outward in each successive pumping phase. Events from the pump-in tests were nearest the frac well location. Events from the data frac started near the wellbore and extended the fracture outward. Events from the propped-frac were the farthest away from the wellbore. Because of the horizontal projection, fracture lengths are somewhat exaggerated.

The apparent NW-SE fracture azimuth is nearly parallel to known fault planes in this area of the field. Locally, there are a number of faults, including a reverse fault between the frac well and the monitor well (Fig. 2). It is possible that other minor faults exist, which could have impacted fracture geometry, altering the expected fracture azimuth and fracture length. The frac fluid may have broken into a fault plane, ceasing to fracture the higher-stressed reservoir rock.

Post-Frac Production

The post-frac production rate initially improved by 40 BPD, compared to an expected rate increase of 150 BPD (Fig. 13).

Reasons for the less-than-expected rate increase are speculative. After-frac logging and modeling suggest a short effective frac half-length and frac height, and low frac conductivity. Microseismic logging indicates greater frac extension, but local faults could have possibly impacted fracture geometry. This fracture treatment was the first frac in the northwest area of the field. The well treated with a much higher frac gradient (1.06 psi/ft) than the 0.91 psi/ft gradient observed elsewhere. There have been three fracs pumped in the northeast area of the field, near the location of the proposed slant well. Each of these fracs was successful in improving productivity or injectivity. Therefore, hydraulic-fracturing is still expected to be effective as a stimulation treatment for the slant well.

Fan Margin Characterization And Modeling

Interpretations of reservoir geology for the Yowlumne field have been derived from core data, a field-wide digitized well log database, a three-dimensional (3D) seismic survey, and a computer-generated 3D shale volume. The reservoir geology was re-evaluated for the northeast area of the field, for both the center of the fan and its distal margin.

Geologic Framework

The Yowlumne field is a giant oil field in the southern San Joaquin basin of California (Fig. 14) which has produced more than 100 MMBO from the Stevens sandstone, a clastic facies of the Upper Miocene Monterey Shale (Fig. 15). The Stevens is a prolific reservoir in the basin and has contributed nearly one-fourth of the more than 11 BBO that the basin has produced since 1864. Because Stevens oils produced at Yowlumne are believed to derive from Monterey Shale source rocks, the field represents part of the Monterey-Stevens petroleum system[6].

The San Joaquin basin during the Miocene was a forearc basin located between a remnant volcanic arc on the east, represented by the Sierra Nevada Mountains, and a transform margin on the west, represented by the San Andreas fault (Fig. 16). Rapid uplift of the basin margins during Late Miocene orogeny shed large volumes of sand into this basin and resulted in the progradation of three depositional systems in the Stevens - a westward-prograding system on the east side of the basin sourced by the Sierra Nevada, an eastward-prograding system on the opposite side sourced by uplifts along the San Andreas fault, and a northward-prograding system, on the southern margin, sourced by uplifted thrust sheets in the Tehachapi-San Emidio Mountains. The Yowlumne Stevens is part of this northward-prograding system (Fig. 17).

The main reservoir of the field, the Yowlumne sandstone, is a clay-bearing arkosic wacke that contains both potassium and plagioclase feldspars. The clays are predominantly authigenic kaolinite derived from diagenesis of detrital feldspars. Mixed-layer smectite/illite, probably detrital in origin, is also present. The mineralogy of these sandstones indicates derivation from uplifted plutonic and metamorphic terranes located in the Tehachapi-San Emidio Mountains.

Well and 3D-seismic data indicate that the reservoir is fan shaped with the proposed slant well located near the distal, eastern margin of the fan (Figs. 18 and 19). Cores taken from within this fan indicate that it is composed of turbidites[7,8], and deposition at bathyal water depths is generally assumed[9]. In addition, the fan in cross-section is lens shaped and does not significantly incise the underlying strata. Therefore, large-scale channeling is absent, an indication that deposition was primarily as sheet sands transported by sediment-gravity flows. The shape, lithofacies, and microfauna characterize the fan as a basin-slope (Class III) reservoir.

Thin shales within the fan divide it into several layers. Five of these layers, labeled A, B, C, D, and E in order of increasing age, produce oil in Unit B. All five layers will be penetrated by the slant well along with a basal wet layer called the W sand (Fig. 20). When

facing basinward (north), in the presumed direction of sediment transport, these layers are least evident on the left (west) side of the fan and most evident on the right (east).

Interestingly, the five layers of Unit B exhibit left-stepping geometries in cross-section[10,11]. In other words, when facing basinward, the basal layer, sand E, is thickest on the right side of the fan; whereas the top layer, sand A, is thickest on the left (Fig. 21). Because the slant well will be located near the right margin of the fan, it will test sand E near its depositional axis and sand A near its distal margin (Fig. 19).

Reflection geometries evident on a 3D-seismic survey[12] indicate downlap within the Yowlumne fan with basinward progradation to the north as well as lateral progradation to the west. Thus, the Yowlumne reservoir is a fan-shaped turbidite complex with progradational geometries.

Reservoir Compartments

Formation pressures from Schlumberger Repeat Formation Tester (RFT) surveys indicate weak compartmentalization of the Yowlumne reservoir (Fig. 22). Injection into the reservoir of a radioactive tracer (Tritium) by Tenneco in June, 1979 confirmed the presence of separate permeability pathways which transported tracer at different rates. Most likely, these pathways represent different compartments which, for the most part, are in pressure communication over geologic time. Thus, these compartments develop the same oil-water contact over thousands of years yet acquire slightly different pressures as the field is rapidly produced over tens of years[13]. Thin shales separate the compartments, and well log correlations indicate correlation of these compartments to reservoir layers A through E (Fig. 20).

Petrophysical Description and Flow Unit Refinement

Petrophysical properties were derived for the study area from core, log, and RFT data. Existing flow units were subdivided into thinner layers and petrophysical properties were calculated for each layer. The petrophysical properties were then mapped by layer.

Core Data

To evaluate porosity-permeability relationships and pore geometries in the Yowlumne reservoir, core data were used to generate porosity-permeability plots, reservoir quality index values, flow zone indicators, cumulative capacity plots, and pore throat size distributions. The porosity ($Ø_{\%}$) and air permeability (K_a) values used in these derivations were obtained from conventional analyses of 840 one-inch diameter, horizontally oriented plugs collected from whole cores of eight wells in the project study area (Table 3 and Table 4, which shows porosity and air permeability values for well 55X-34). Capillary pressure measurements were taken from two of the eight wells (Table 5).

Prior to 1993, the heterogeneity index (Hi) was used to predict pore geometries from porosity and permeability data[14]. A more recent technique employs the "flow zone indicator" (FZI). Although both Hi and FZI are derived from the mean hydraulic radius (Equation 1), FZI is considered a more reliable indicator of pore geometry because it takes into account

grain shape, pore tortuosity, and surface area per unit grain size[15]. This study used FZI rather than Hi to identify and characterize hydraulic units within the Yowlumne sand.

$$\text{Mean Hydraulic Radius (microns)} = (K_a / Ø_{\%})^{0.5} \quad (1)$$

To derive FZI values, the reservoir quality index (RQI), and pore ratio (PR) were first calculated for different porosity-permeability pairs[15] using Equations 2 and 3.

$$RQI = \pi / 100 * (K_a / Ø_{\%})^{0.5} \quad (2)$$
$$PR = Ø_{\%} / (100 - Ø_{\%}) \quad (3)$$

A hydraulic unit represents a unique pore geometry that plots on a log-log plot of RQI versus PR as a straight line with unit slope[15] (Fig. 23). The intercept of each hydraulic unit line with the PR =1 axis designates a value called the "flow zone indicator" (FZI), which is also calculated with Equation 4. Therefore, hydraulic units can be characterized as ranges of $\log_{10}$FZI. Hydraulic units in the Yowlumne sand were assigned whole numbers based on ranges of $\log_{10}$FZI (Table 6). In general, higher hydraulic unit numbers represent pore geometries characterized by coarser grain size and lower clay content. Hydraulic units for well 55X-34 are listed in Table 4 and shown graphically in (Fig. 24). Figure 25, a crossplot of permeability vs. porosity for well 55X-34, groups the data by hydraulic unit.

$$FZI = RQI / PR \quad (4)$$

Pore throat sizes were determined from $Ø_{\%}$ and K_a by calculating the effective mean grain sizes in centimeters[13] (D_g) using Equation 5. By assuming rhombohedral close packing of equidimensional spherical grains, the minimum pore throat diameters[13] in microns (D_p) were derived using Equation 6. Pore throat sizes calculated with this methodology for well 55X-34 are listed in Table 4.

$$D_g = 0.1 * (1.89 * K_a * Ø_{\%}^{-5.1})^{0.5} \quad (5)$$
$$D_p = 154 * D_g \quad (6)$$

In addition, pore throat sizes were calculated from capillary pressure values[16] in psi (P_c) using Equation 7. Because the shapes of mercury injection curves from which the capillary pressure data are derived indicate that the Yowlumne reservoir is moderately sorted to poorly sorted (Fig. 26), no one pore size was representative for any given core sample. Furthermore, only one injection curve could be extrapolated to a maximum capillary pressure (i.e., minimum pore diameter). Therefore, pore throat diameters were determined for extrapolated entry pressures, the pressures at 50% mercury saturation (Sat_{50}), and the maximum pressure applied during the analyses (35 psi). Pore throat sizes derived from the capillary pressure data are listed in Table 5.

$$D_p = (2 * \sigma * \cos\theta) / (69035 * P_c) \quad (7)$$

The effect of overburden pressure on porosity and permeability was modeled by applying an increasing confining pressure to 14 core plugs from two wells in the study area (Table 7). The 840 porosity and permeability pairs from the conventional core analysis

represent subsurface depths of 11,725 ft to 13,141 ft. Assuming a hydrostatic gradient of .446 psi/ft, these depths represent original burial pressures of 5230 to 5860 psi. Therefore average porosity reductions of 8.7% at 5,000 psi, and average permeability reductions of 42.6 % for the same pressure approximate reductions expected for the Yowlumne reservoir at depth.

RFT Data

Reservoir pressures measured with a Schlumberger Repeat Formation Tester (RFT) were available from four wells in the study area. Although the results of more than a decade of waterflooding demonstrate that the reservoir throughout Unit B is in pressure communication with a common oil-water contact, the pressure variations indicate compartmentalization to some degree (Fig. 27). As noted elsewhere, these variations are probably an artifact of production, and do not represent true compartments separated by impermeable seals[17,18]. Nonetheless, the different RFT pressures are an indication of different flow zones.

Log Data

A database of digitized well log curves was constructed for a study area of approximately 1.5 square miles, centered on the location for the proposed slant well. This database was constructed using TerraScience, an interactive well log correlation and analysis software package.

Shale volumes (Vsh) and sonic porosities ($Ø_{sonic}$) at half-foot depth intervals were calculated from gamma ray (GR) and sonic travel time logs (dt) for 31 wells using Equations 8 and 9. Sonic porosities were converted to effective porosities ($Ø_{eff}$) using Equation 10. For one well in the database for which no sonic data were available, neutron porosities were converted to effective porosities using Equation 11, which was derived from a NPHI to DPHI crossplot.

$$Vsh = (GR - Gr_{ss}) / (GR_{sh} - Gr_{ss}) \quad (8)$$

$$Ø_{sonic} = (dt - tt_{matrix}) / (tt_{fluid} - tt_{matrix}) \quad (9)$$

$$Ø_{eff} = Ø_{sonic} - (Ø_{shale} * Vsh) \quad (10)$$

$$Ø_{eff} = Ø_{DPHI} = Ln\, Ø_{NPHI} * 0.0537 + 0.2265 \quad (11)$$

Baselines for sand (Gr_{ss}) and shale (Gr_{sh}) on the GR curves were determined for each well. $Ø_{sonic}$ was determined using a sand travel time (tt_{matrix}) and fluid travel time (tt_{fluid}) recommended by Dang[19]. Shale porosities ($Ø_{shale}$) were determined for each well by averaging $Ø_{sonic}$ for the Vsh >.9 interval of the upper Stevens (N point marker to base Yowlumne reservoir).

tt_{matrix} = 55.5 µsec/ft
tt_{fluid} = 189 µsec/ft

Water saturations (Sw) were calculated using the Archie equation (Equations 12 and 13) with formation temperatures that were depth adjusted with Equation 14, and

formation water resistivities that were temperature adjusted using Equation 15 (Arps formula). If at a given depth $Ø_{eff} < .005$ or $Sw > 1$, then Sw was set to 1.

$$F = a / (Ø_{eff})^{m} \quad (12)$$
$$Sw = ((F * Rw) / Rt)^{1/n} \quad (13)$$
$$T_{fm} = T_{surf} + \text{gradient} * (\text{depth}/100) \quad (14)$$
$$Rw_{fm} = Rw_{75°F} * (75°F + 6.77) / (T_{fm} + 6.77) \quad (15)$$

Equations 12 through 15 used constants from Dang[19], the field geothermal gradient, and a formation water resisitivity (Rw) from Dang[19].

a	=	1.0
m	=	1.64
n	=	1.36
T_{surf}	=	75°F
gradient	=	1.4°F / 100 ft
Rw @ 75°F	=	0.41 ohm-m

Permeabilities in air (K_{air}) and liquid (K_{liq}) were calculated from effective porosities using Equations 16 through 19. Equation 16 was based on correlation of core data to log data discussed in Dang[19], and Equation 17 was derived by John Melvin of ARCO on the basis of permeability relationships observed in the 38X-34 well.

For $Ø_{eff} \leq 0.127$: (16)

$$K_{air} = 10 \wedge (0.19 * Ø_{eff} * 100 - 1.62)$$

For $Ø_{eff} > 0.127$: (17)

$$K_{air} = 123.91 - 28.149 * (Ø_{eff} * 100) + 1.7066 * (Ø_{eff} * 100) \wedge 2 - 1.72666 * 10 \wedge (-2) * (Ø_{eff} * 100) \wedge 3$$

For $K_{air} \leq 50$: (18)

$$K_{liq} = 0.0277 * K_{air} + 0.0135 * K_{air} \wedge 2 - 1.208 * 10 \wedge (-4) * K_{air} \wedge 3$$

For $K_{air} > 50$: (19)

$$K_{liq} = 0.4 * K_{air}$$

Net sand for specific stratigraphic intervals was determined using the criteria $Vsh < 0.3$ and $Ø_{eff} > 0.08$. Average net/gross, $Ø_{eff}$, K_{liq}, and Sw were determined for net sand only.

Flow Unit Refinement

Seismic, well log, and pressure data, together with analysis of the oil-water contacts indicated that the Yowlumne sandstone contains seven interlayered, lobe-shaped sand bodies[20,21] . Five of these lobes, designated the A, B, C, D and E sands, are present in the project study area (Figs. 19 and 28). A sixth compartment, the W sand, sits beneath the E lobe but is wet and does not produce hydrocarbons. Additional correlations, constrained by

RFT and Hydraulic Unit analysis, justified further subdivision of the B, C, D and E sands into eight flow units, which together with the A and W sands gave a total of 10 flow units for the study area (Fig. 29).

Five parameters (gross-sand thickness, net-to-gross ratio, $Ø_{eff}$, K_{liq}, and Sw) were derived from the log data and mapped for each flow unit. The parameters of $Ø_{eff}$, K_{liq}, and Sw represent average net sand values. Finally, a digital database, based on state planar coordinates, was generated for each map for input into a fluid flow simulation model for the Yowlumne reservoir.

Summary of Results

Cumulative capacity plots of the core data indicated that the Yowlumne reservoir at surface pressure has an average $Ø_{eff}$ of 16.6%, K_a of 44 md, and pore throat diameters of 4 to 10 µ. With application of a 5000 psi confining pressure, analogous to reservoir depths of 11,000 to 13,000 ft, porosity and permeability reduce to 15.2% and 25 md. Reservoir characteristics are summarized in Table 8.

Although porosity and permeability vary considerable within the data set (Fig. 30), the pore geometries are similar. About 43% of the samples have geometries of type 12 hydraulic units, and 83% are within the type 11 to 13 range (Fig. 31).

Comparisons of core-derived and log-derived data indicated that the log data would effectively model the reservoir. Although measured core permeabilities compared favorably to permeabilities calculated using Equation 16 (Fig. 30), a better match was obtained using Equation 16 for $Ø_{eff} \leq 12.7\%$ and Equation 17 for $Ø_{eff} \geq 12.7\%$ (Fig. 32). Because the log-based porosities were about 1% less than corrected core porosities (Fig. 33), reserve estimates based on the log data alone may be conservative.

In general, reservoir quality decreases from west to east in the project study area, towards the distal margin of the Yowlumne submarine fan (Figs. 34 to 37). Consequently, the reservoir at the location of the proposed slant well is tighter ($Ø_{eff} \leq 12\%$), less permeable ($K_{liq} < 2$ md), and contains less net sand (net/gross = 65%) than wells located closer to the center of the fan ($Ø_{eff} > 16\%$, K_{liq} = 10-20 md, net/gross = 80%). Presumably, this decrease in reservoir quality indicates higher clay content and/or a greater proportion of shale interbeds.

Reservoir Modeling

A full-field 3D reservoir model constructed in 1992 was used to identify and roughly quantify bypassed oil in the northeast fan margin of Unit B. Unfortunately, the full-field model was too coarse for detailed representation of this region and was only useful as a screening tool in evaluating development options.

A fine-grid, partial-field model was therefore constructed which could accommodate the detailed geologic description discussed in the previous section. The partial-field model also utilized local grid refinement[22] (LGR) to provide more explicit definition of the proposed deviated wellbore and hydraulic fractures.

Model Grid

Areal Grid Definition

Of primary concern in establishing model boundaries was influx and/or efflux of reservoir fluids from the northeast fan-margin region during waterflood operations. A streamtube model was used to examine historical fluid movement in and around the area of interest. This work indicated that water injection had not resulted in consistent "no-flow" boundaries near the proposed slant well location (Fig. 38). Instead, significant fluid influx from southern and western areas of the field had occurred due to uneven and irregular waterflood patterns. As a result, the model was extended over the maximum area possible, blanketing the entire region examined during the reservoir characterization effort[22]. This region covered an area of approximately 720 acres.

A 34 X 34 orthogonal grid matrix was established as the areal grid (Fig. 39). Each cell represented an area of approximately 0.6 acres, one-third the size of the full-field model cells. Due to hardware limitations, only six cell interfaces existed between adjacent injectors and producers. While numerical dispersion effects were expected, they were not a major concern. Model forecasts would be continuations of an existing displacement process. Saturation functions would simply be adjusted during the history match to compensate for dispersion and non-represented heterogeneities[23].

Layering

Ten layers were used to explicitly represent each hydraulic unit defined in the fan margin characterization (Fig. 29). All intervals are considered pay except for Sand W, a wet non-pay interval. It was included in the model to examine rate impacts from downward hydraulic-fracture growth.

Local Grid Refinement

A nested grid was designed for the area immediately surrounding the proposed well location (Fig. 40). Local grid refinement of this area allowed better definition of the deviated well path and fracture planes[22]. However, the nested grid also added approximately 3500 cells to the model and required a fully implicit solution technique. As a result, most of the history match was conducted with the 11,560-cell parent grid. Local grid refinement was added only at the end of history matching.

Gridblock Properties

Incorporation of Geologic Model

Cell values for gross thickness, net-to-gross ratio, porosity and horizontal permeability were explicitly defined based on maps from the new geologic model. Vertical transmissibility between layers was set at zero. A horizontal to vertical permeability ratio (kv/kh) of 0.05 was used to represent the random, discontinuous shales in the fan-margin region[24].

Model water saturations were not based on mapped values, but were determined from structural position (height above the water-oil contact) and capillary pressure. Gas saturation values were set to zero, since the reservoir was undersaturated at discovery.

Capillary Pressure

Air-brine drainage capillary pressure data, including porous plate and centrifuge measurements, were used to establish initial water saturation values for each cell. A Leverett J-function was constructed to account for changes in reservoir quality[25]. A J-function was also calculated using TVD-corrected log estimates of water saturation, porosity and permeability. Although the log data were scattered, there was generally good agreement between log and core measurements (Fig. 41).

The J-function was also used to represent capillarity during the waterflood, since imbibition measurements were not available.

Relative Permeability

Water-oil relative permeability curves were developed from unsteady-state corefloods. Water-oil experimental data were normalized over the flowable saturation range and fit to Corey curves[26] (Fig. 42). Similar work was conducted to construct gas-oil relative permeability curves (Fig. 43).

Three-phase relative permeability was represented in the model using the Stone II empirical treatment[27].

PVT Properties

PVT properties were drawn directly from the full-field model (Table 9). Oil and gas properties taken from the earlier model were based largely on a recombined fluid sample. Bubble point pressure, which was varies with depth, was estimated to be 2115 psi for the model area.

History Matching

Following initialization, the partial-field model was tuned to match actual field performance over a 19-year period, which included six years of primary depletion and 13 years of waterflood operations. This process progressed from matching regional pressure and production data to matching individual well performance to eventually reproducing flow unit pressures and saturations.

The history match was complicated by fluid movement across model boundaries. Pseudo-wells were used along the north, west, and south boundaries to account for fluid flux. This increased uncertainty associated with the history match, especially near model boundaries. Fortunately the size of the model and quality of the history match effectively addressed boundary flux concerns.

Regional Match

Oil production and water injection rates were directly specified in the model, limiting history match parameters at the regional level to water and gas production rates and average reservoir pressure. Water-oil and gas-oil relative permeability curves were adjusted to achieve a rough match of gas and water rates.

Pseudo-well flux rates were next adjusted to match average reservoir pressures. During primary depletion, flux rates were minor and primarily limited to updip wells located along the southern boundary. These pseudo-wells were used to drain off free gas which was liberated from solution as reservoir pressure fell below the bubble point. Following startup of the waterflood, flux rates were reversed to represent fluid movement into the model area along the northern, western and southern boundaries. Irregular injection patterns funneled fluid to the central and eastern portions of the model.

Rate and pressure matches for the entire model area are shown in Figs. 44 and 45.

Well Match

Before attempting local adjustments to match individual well performance, the water-oil pseudo-relative permeability curve was reviewed and compared to experimental data (Fig. 46). Gross adjustments applied to the curves seemed excessive, given the amount of numerical dispersion expected for the model. The model curves resulted in too favorable fractional flow.

Review of individual wells indicated that the favorable fraction flow was probably related to scale deposition in producing wells. Several wells had exhibited scaling tendencies, and typically experienced drastic productivity reductions following water breakthrough. Reperforating and acidizing almost always increased total fluid production, but oil rates usually decreased. Apparently scale had acted as a natural "water shut-off treatment" in zones that had experienced breakthrough. In wells that were pump-limited, this effect resulted in larger drawdowns on lower pressure, higher oil cut zones.

Adjustments of the water-oil relative permeability curve to match post-acidizing and perforating water cuts resulted in a much more reasonable pseudo-function. Water production rates were then too high for most wells. In order to match water cuts, layer skin factors were specified for zones which experienced water breakthrough. The skins were then removed following acidizing or reperforating.

Layer skin factors were also applied to injectors to match biannual injection surveys. Initial surveys typically mimicked permeability profiles and therefore matched model injection splits. However as injection continued, the two sets of data tended to diverge due to preferential pore throat plugging and the accumulation of fill. Sands E1 and E2 (layers 8 and 9) were most vulnerable because of smaller pore throats and their position at the base of most wellbores. This resulted in generally poor injection support in the affected flow units. Layer skin factors were used to match this degradation of injection profiles.

Local adjustments of fluid flux from pseudo-wells were also attempted to match well rates along model boundaries. Flux rates were changed to bottomhole pressures. Phase splits were also adjusted to match individual well water and gas rates. By the end of the history match period, most of the fluid influx was water, which reduced the importance of accurately predicting future influx phase splits.

Flow Unit Match

Limited data were available to evaluate the model's accuracy at the flow unit level. RFT pressures were available from three wells in the model area: 47X-34, 56X-34 and 57X-34. Saturation estimates from openhole resistivity logs were available from a number of infill wells, but most were drilled early in the waterflood and did not encounter swept intervals. Only the most recent well, 38X-34RD, penetrated watered-out intervals.

Model layer pressures closely matched RFT pressures, generally within 200 psi (Fig. 47). Model saturations compared favorably to log-derived saturations from 38X-34RD, which was drilled in January, 1996. The model accurately predicted high oil saturations within Sands A, E1 and E2 (layers 1, 8, and 9), as shown in Fig. 48.

Near the end of history matching, the nested grid described earlier was added to the model. With the change in grids, it was also necessary to switch from an IMPES to a fully implicit formulation of the flow equations. Neither change greatly altered the history match. Only minor adjustments were needed to finalize the match.

Performance Forecasts

The fine-grid, partial-field model was used to test a variety of development alternatives aimed at optimizing project economics. Model forecasts compared slant well performance to more conventional development options and quantified rate impacts of changes in well location, orientation, and completion technique. Model results are reported in terms of incremental rates and reserves in order to eliminate interference effects.

Continued Operations

All model forecasts were compared against a base prediction to determine incremental performance. The base prediction assumed water injection would replace reservoir voidage through year end 1999, and then be limited to re-injection of produced water for the remainder of the expected field life (year end 2005).

North-South Fractured Slant Well

The model was initially used to predict the performance of a slant well drilled along the south-to-north well path as described in the project proposal (Fig. 38). The well was expected to penetrate the reservoir interval at a 55° angle from vertical entering from an updip position (25° dip). This provided 1100 ft of pay exposure within approximately 180 ft of stratigraphic thickness. The well was also assumed to be fractured at three locations spaced 250 ft apart along the well path.

Based on results from the stimulation treatment in well 84-32, fractures were assumed to propagate along a northwest-southeast trend. Results from microseismic monitoring of the 84-32 treatment also indicated that fractures would probably not be confined by internal shales and would tend to be asymmetric with the longer fracture wing extending to the interior of the field. Fracture height was defined as equal to fracture length and was set at approximately 175 ft. Roughly 70% of total fracture length was allocated to the interior fracture wing, leaving 30% to extend toward the sand margin.

Each fracture was represented in the model as a separate deviated wellbore which was defined to traverse the entire fracture plane numerous times. This treatment created an infinite conductivity pathway. Rates from each fracture were constrained based upon analogy to a successful frac in offset well 57X-34 and to predictions from commercial fracture-stimulation software.

Model results indicated the well would initially produce 1252 BOPD if drawn down to a producing bottomhole pressure of 1200 psi. Despite the high initial rate, incremental reserves attributed to the slant well were only 465 MBO.

East-West Fractured Slant Well

Saturation and pressure distributions in the partial-field model differed from results generated by the full-field model. Better representation of reservoir heterogeneity and a change in flow unit correlations resulted in a significant portion of the original bypassed oil target being swept. Fine-grid modeling suggested that an alternate east-to-west well path would be superior to the south-to-north orientation. An area of higher oil saturations appeared to be trapped between two east-west rows of producers immediately adjacent to the original slant well location.

A second slant well location was therefore tested with approximately 1000 ft of east-to-west formation exposure (Fig. 34). The well was expected to penetrate the formation along strike at a 75° angle from vertical and was assumed to be fractured at three points 250 ft apart (Fig. 20). The approach used to represent each fracture plane was identical to the methodology described for the north-south well. This required that the nested grid be re-oriented to accommodate the east-west well path.

Model results indicated the well could initially produce 2180 BOPD and provide 724 MBO of incremental reserves. Improved well performance for the east-west orientation was attributed to higher oil saturations and better reservoir quality. The well also produced an incremental 8% of OOIP from the distal fan-margin region.

Vertical Wells

In order to evaluate other development options, the model was next used to predict performance of three vertical wells placed equidistant along the east-to-west slant well path. The wells were assumed to be unstimulated with 0.25 ft wellbore radii and skin factors of 3.

Model projections indicated that rates and reserves were much lower for vertical wells than the east-to-west slant well. The combined initial rate of all three wells was 679 BOPD, while incremental reserves were projected to be only 223 MBO.

Increased pay exposure along the deviated well path and fracture planes accounted for most of the rate variation between the slant well and vertical wells. However, operational differences in the two sets of forecasts also contributed to the rate difference. The slant well was assumed to be equipped with an electrical submersible pump (ESP) to minimize producing bottomhole pressure. The vertical wells were assumed to be lifted using hydraulic jet pumps operating at 500 psi higher bottomhole pressure. The incremental rates from the vertical wells resulting from greater pressure drawdowns did not justify the higher operating costs associated with ESPs.

Horizontal Well

The east-to-west slant well was also compared to a horizontal well. The horizontal well was assumed to be drilled and completed entirely within Sands E1 and E2 (layers 8 and 9), which appeared to be relatively unswept. The well would follow the same lateral east-west path as the slant well.

The model forecast suggested the horizontal well would initially produce 404 BOPD and provide only 74 MBO of incremental reserves. These results confirmed the obvious need to establish communication between the wellbore and each productive flow unit.

Number of Fractures

A sensitivity study was conducted to examine the impact of reducing the number of fracture treatments pumped in the slant well. Model results are summarized below:

Number of Fracs	*0*	*1*	*2*	*3*
Incremental Rate, BOPD	684	1267	1638	1980
Incremental Recovery, MBO	296	527	622	734
Total Well Recovery, MBO	691	1215	1388	1547

Model results clearly demonstrated the importance of establishing vertical communication at multiple points along the well path.

Analytical Estimates of Reserves and Initial Rates

Analytical methods were used to confirm model predictions of reserves and initial rates. Although there were many uncertainties, particularly with reserve estimates, model results appeared to be reasonable. Because of the detailed geology and reservoir characterization in the fine-grid model, and the difficulty of analytical methods to account for fluid flux in a small volumetric region, the results from the reservoir simulation model were felt to be much more reliable.

Development Strategy

The fine-grid reservoir-simulation model confirmed the use of an east-to-west slant well and multiple hydraulic fractures to develop the fan-margin region. The well clearly outperformed other development options in thin, highly-stratified intervals (Figs. 49 and 50).

Project Economics

The original economics of drilling a north-to-south slant well were revised to reflect the currently planned east-to-west well path and the results of the fine-grid reservoir simulation of the fan-margin region.

Economic Input

Decision Tree Analysis

Decision tree analysis was applied to production and costs in the economic evaluation to account for the numerous outcomes that are possible (Fig. 51). For example, there is mechanical risk in successfully drilling the well and pumping multiple fracs. There is also geologic and reservoir risk with rock quality and saturations. Finally, successfully pumping each frac does not guarantee desired frac height, length, width, conductivity, azimuth, etc.

Costs to Drill, Complete, and Operate

The investment-outlay estimates to drill, complete, and equip the slant well are shown in Table 10. Some of the activities that add to the costs to drill, complete, and equip a "typical" vertical well in the Yowlumne field are listed below:

(1) Directional work.
(2) Cut and analyze whole core.
(3) Drillpipe-conveyed logging.
(4) Running an FMI log and processing data.
(5) Perforate long intervals.
(6) Three large hydraulic-fracture treatments.
(7) Microseismic logging in an offset well for each of the three fracs.
(8) Selective production tests, pressure transient tests, and production logs.
(9) Electric submersible pump (ESP) lift.

Table 11 lists the annual operating expenses used in the economic evaluations for the eight and one-half year life of the well. These expenses are also higher than "normal".

Operations surveillance costs represent lifting costs for a well equipped with an ESP sized for 3000 - 3500 BPD, including provisions for one ESP replacement each year. The production tubing will be equipped with a "Y" offset tool to permit production logging and pressure testing while the well is producing. In addition, costs are included for remedial water shut-off workovers.

The economics also include contract and company labor costs (including overhead and burden) and five years of technology-transfer costs.

All expenses shown in Table 11 are inflated 5% annually.

Production

The production streams for each scenario consisting of a slant well with no fracs up to a slant well with three fracs were input into the economic evaluation (Fig. 52). Each stream was factored based upon decision tree analysis. The expected-value incremental production stream (Fig. 53) represents a starting rate of 967 BOPD and reserves of 407 MBO. Expected-value reserves are 55% of the three-frac success case reserves.

Gas and NGL sales were based upon a GOR of 489 SCF/STB, gas shrinkage of 22%, and 5.1 GPM yield.

Product Prices

Pricing was based upon 1996 postings for the Yowlumne Field (31° API). The starting prices were $18.00 per BO, $18.15 per BNGL, and $1.45 per MCF. Prices were escalated at 5% per year, consistent with escalation of operating expenses.

Tax Rates

Income tax rates used in the economics were 35% for federal and 5.4% for California state. Severance tax rates were 2.2% for oil and 0.22% for gas. The ad valorem tax rate was 1.61%.

Results

Using commercial economic analysis software, expected-value, incremental economics were calculated for the project based upon working and revenue interests of 100%. The following table lists the present worth figures, BFIT and AFIT, for a range of discount rates:

Discount Rate, %	*BFIT Present Worth, M$*	*AFIT Present Worth, M$*
0	629	387
5	865	471
10	969	487
15	992	463
20	967	416

The economics were less favorable at lower discount rates due to rate acceleration effects. Although the well had full incremental operating expenses for 8.5 years, there was virtually no incremental production after five years. Higher discount rates increased the present values of the negative cash flows after year 5, thereby improving project economics.

Technology Transfer

Project Evaluation Report

A project evaluation report for budget period one was prepared and shipped to the DOE on September 27, 1996.

Open File

An "open file" for this project is being established with the California Division of Oil, Gas, and Geothermal Resources (DOGGR). The open file will be available to the public, and is expected to be useful to operators of slope-basin clastic reservoirs, particularly in California.

Technical Papers, Presentations, Workshops

Project objectives and preliminary results were presented at a well stimulation forum held in Girdwood, Alaska during the week of March 11, 1996. The forum was hosted by ARCO Alaska Inc. and was attended by representatives from over 20 companies and universities.

Dr. Mike Clark gave an oral presentation on May 22, 1996 concerning the project to an advanced sedimentary geology class at the University of California, Santa Barbara. The title of his talk was Growth Patterns of a Miocene Turbidite Complex in an Active-Margin Basin, Yowlumne Field, San Joaquin Basin, California.

Dr. Mike Clark presented Growth Patterns of a Miocene Turbidite Complex in an Active-Margin Basin, Yowlumne Field, San Joaquin Basin, California at the 1996 annual convention of the American Association of Petroleum Geologists (AAPG) on May 29, 1996.

Mr. Jim Davis, President, AWE discussed the project in a presentation to the Bakersfield chapter of The American Association of Drilling Engineers on September 19, 1996.

An abstract entitled Characterization of the Distal Margin of a Basin-Slope (Class III) Reservoir, ARCO-DOE Slant Well, Yowlumne Field, California has been submitted for presentation at the Fourth International Reservoir Characterization Conference workshop on March 2, 1997. A poster and technical paper will also be prepared for the workshop.

Dr. Mike Clark presented the project to a petroleum geology class at the University of California, Santa Barbara in October, 1996.

Dr. Mike Clark is preparing a paper concerning the project to present at the annual convention of the Pacific Section of AAPG in May, 1997.

References

1. Gidley, J.L., Holditch, S.A., Nierode, D.E., and Veatch, Jr., R.W., Recent Advances in Hydraulic Fracturing, Monograph Series, SPE, Richardson, Tex. (1989) 12, 42-43.

2. Werner, K.S., Graven, E.P., Berkman, T.A., and Parker, M.J., Direction of Maximum Horizontal Compression in Western Oregon Determined by Borehole Breakouts, Tectonics, 10, 948-957, 1991.

3. Castillo, D.A., and Zoback, M.D., Systematic Variations in Stress State in the Southern San Joaquin Valley: Inferences Based on Well-Bore Data and Contemporary Seismicity, AAPG Bull., 78, 1268-1269, 1994.

4. Nolte, K. G.: "Determination of Fracture Parameters from Fracturing Pressure Decline," paper SPE 8341 presented at the 1979 SPE Annual Technical Conference and Exhibition, Las Vegas, Sept. 23-26.

5. Fix, J. E., "Hydraulic Fracture Diagnostics Survey," Technical Report No. 96-1, 59 p., 1996.

6. Graham, S. A. and Williams, L. A., Tectonic, Depositional, And Diagenetic History of Monterey Formation (Miocene), Central San Joaquin Basin, California: American Association of Petroleum Geologists Bulletin, v. 69, p. 385-411, 1985.

7. Church, H. V., Display Of Cores From The Stevens Sand (Upper Miocene), Southern San Joaquin Valley, California: California Well Sample Repository, Special Publication No. 1, California State University, Bakersfield, 40, 1978.

8. Hewlett, J. S. and Jordan, D. W., Stratigraphic And Combination Traps Within A Seismic Sequence Framework, Miocene Stevens Turbidites, Bakersfield Arch, California in (Weimer, P. and Posamentier, H., eds.) Siliciclastic Sequence Stratigraphy: American Association of Petroleum Geologists, Memoir 58, p. 135-162, 1994.

9. Berg, R. R. and Royo, G. R., Channel-Fill Turbidite Reservoir, Yowlumne Fields, California In (Barwin, J. H., MacPherson, J. G., and Studlick, J. R., eds.) Sandstone Petroleum Reservoirs: Casebooks in Earth Science, Springer-Verlag, New York, p. 467-487, 1990.

10. Jessup, D. D. and Kamerling, M., Depositional Style Of The Yowlumne Sands, Yowlumne Oil Field, Southern San Joaquin Basin, California (abstract): Bulletin of the American Association of Petroleum Geologists, v. 75, p. 368, 1991.

11. Clark, M. S., Melvin, J., and Kamerling, M., Growth Patterns Of A Miocene Turbidite Complex In An Active-Margin Basin, Yowlumne Field, San Joaquin Basin, California (abstract): American Association of Petroleum Geologists, Annual Convention Official Program, San Diego, 1996, v. 5, p. A27, 1996.

12. Fisher, D. A. and Wall, K. S., Yowlumne Field Horizon Slice Interpretation: ARCO Exploration and Production Technology Proprietary Report TSR 89-0065, 21 p., 4 enclosures, 1989.

13. Berg, R. R., Capillary Pressures In Stratigraphic Traps, American Association of Petroleum Geologists Bulletin, v. 59, p. 939-956, 1975.

14. Amaefule, J. O., Kersey, D. G., Marshall, D. M., Powell, J. D., and Valencia, L. E., and Keelan, D. K., Reservoir Description:A Practical Synergistic Engineering And Geological Approach: paper SPE 18167, p. 1-30, 1988.

15. Amaefule, J. O., Altunbay, M., Tiab, D., Kersey, D. G., and Keelan, D. K., Enhanced Reservoir Description: Using Core And Log Data To Identify Hydraulic (Flow) Units And Predict Permeability In Uncored Intervals/Wells: paper SPE 26436, p. 1-16, 1993.

16. Vavra, C. L., Kaldi, J. G., and Sneider, R. M., Capillary Pressure In (Morton-Thompson, D. And Woods, A. M., eds.) Development Geology Reference Manual: AAPG Methods in Exploration Series, No. 10, American Association of Petroleum Geologists, p. 221-225, 1992.

17. Berg, R. R. and Royo, G. R., Channel-Fill Turbidite Reservoir, Yowlumne Fields, California In (Barwin, J. H., MacPherson, J. G. and Studlick, J. R., eds.) Sandstone Petroleum Reservoirs: Casebooks In Earth Science, Springer-Verlag, New York, p. 467-487, 1990.

18. Clark, M. S., Beckley, L. M., Crebs, T. J., and Singleton, M. T., Tectono-Eustatic Controls On Reservoir Compartmentalization: An Example From The Upper Miocene, California: Marine and Petroleum Geology, v. 13, p. 475-491, 1996.

19. Dang, T. T., Petrophysical Evaluation Of The Yowlumne Field: Porosity, Water Saturation And Permeability Models: ARCO Exploration and Production Technology Proprietary Report TSR 92-0017, 40 p., 5 appendices, 1992.

20. Jessup, D. D. and Kamerling, M., Depositional Style Of The Yowlumne Sands, Yowlumne Oil Field, Southern San Joaquin Basin, California (abstract): Bulletin of the American Association of Petroleum Geologists, v. 75, p. 368, 1991.

21. Clark, M. S., Melvin, J. and Kamerling, M., Growth Patterns Of A Miocene Turbidite Complex In An Active-Margin Basin, Yowlumne Field, San Joaquin Basin, California (abstract): American Association of Petroleum Geologists, Annual Convention Official Program, San Diego, 1996, v. 5, p. A27, 1996.

22. Mattax, C. C. and Dalton, R. L., Reservoir Simulation, Monograph Series, SPE, Richardson, TX, (1990) 13, p. 50.

23. Mattax, C. C. and Dalton, R. L., Reservoir Simulation, Monograph Series, SPE, Richardson, TX, (1990) 13, 20-21.

24. Begg, S.H., Chang, D.M., and Haldorsen, H.H, A Simple Statistical Method for Calculating the Effective Vertical Permeability of a Reservoir Containing Discontinuous Shales, paper SPE 14271 presented at the 60th Annual Technical Conference and Exhibition of the Society of Petroleum Engineers, Las Vegas, Nev., September 22-25, 1985.

25. Amyx, J. W., Bass, D. M., and Whiting, R. L.: Petroleum Reservoir Engineering Physical Properties, McGraw-Hill, New York, (1960), 155-156.

26. Corey, A. T., et al.: "Three-Phase Relative Permeability," *JPT* (Nov. 1956) 349-51; *Trans.*, AIME, 207.

27. Stone, H. L.: "Estimation of Three-Phase Relative Permeability and Residual Oil Data," *J. Cdn. Pet. Tech.* (Oct.-Dec. 1973) 53-61.

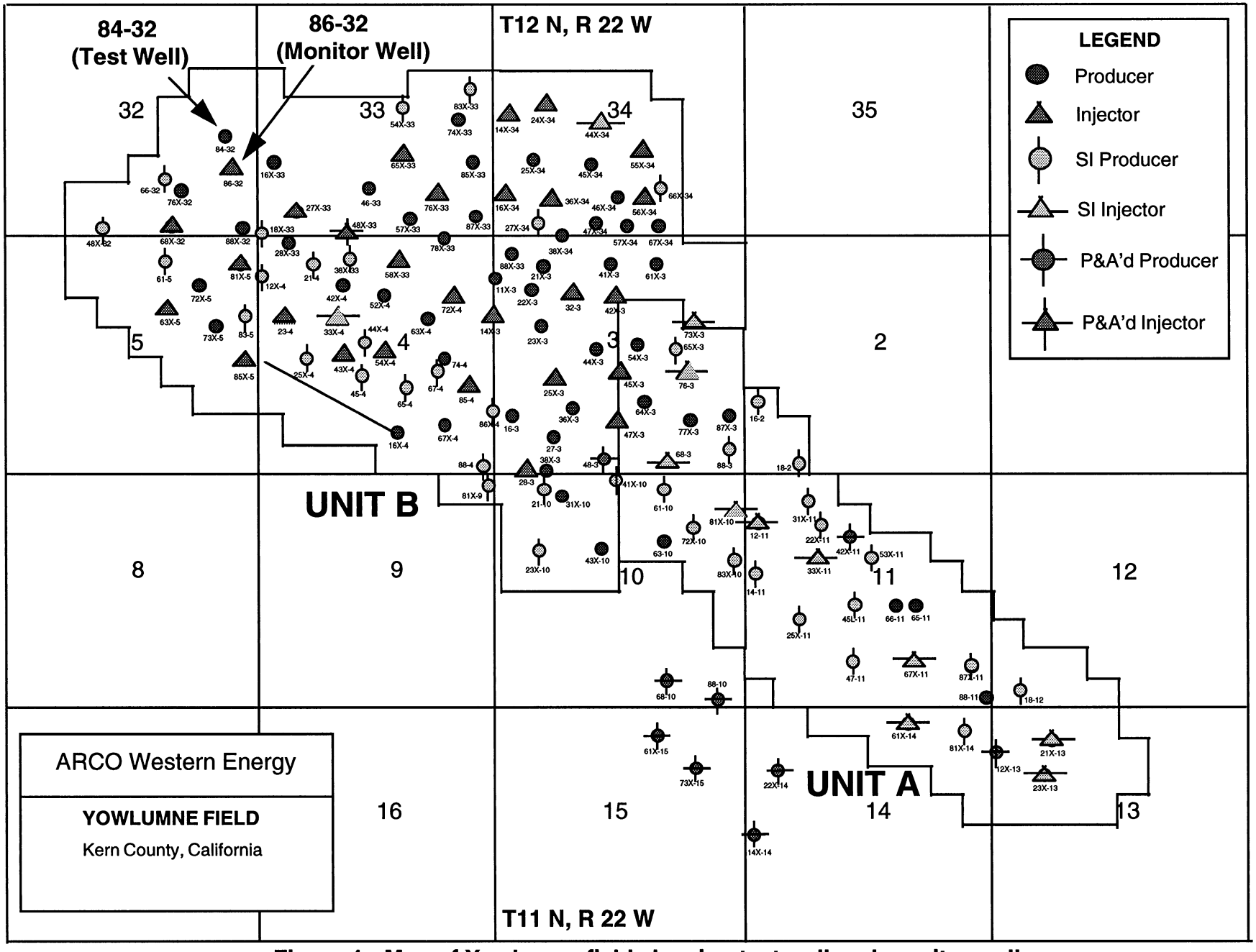

Figure 1: Map of Yowlumne field showing test well and monitor well

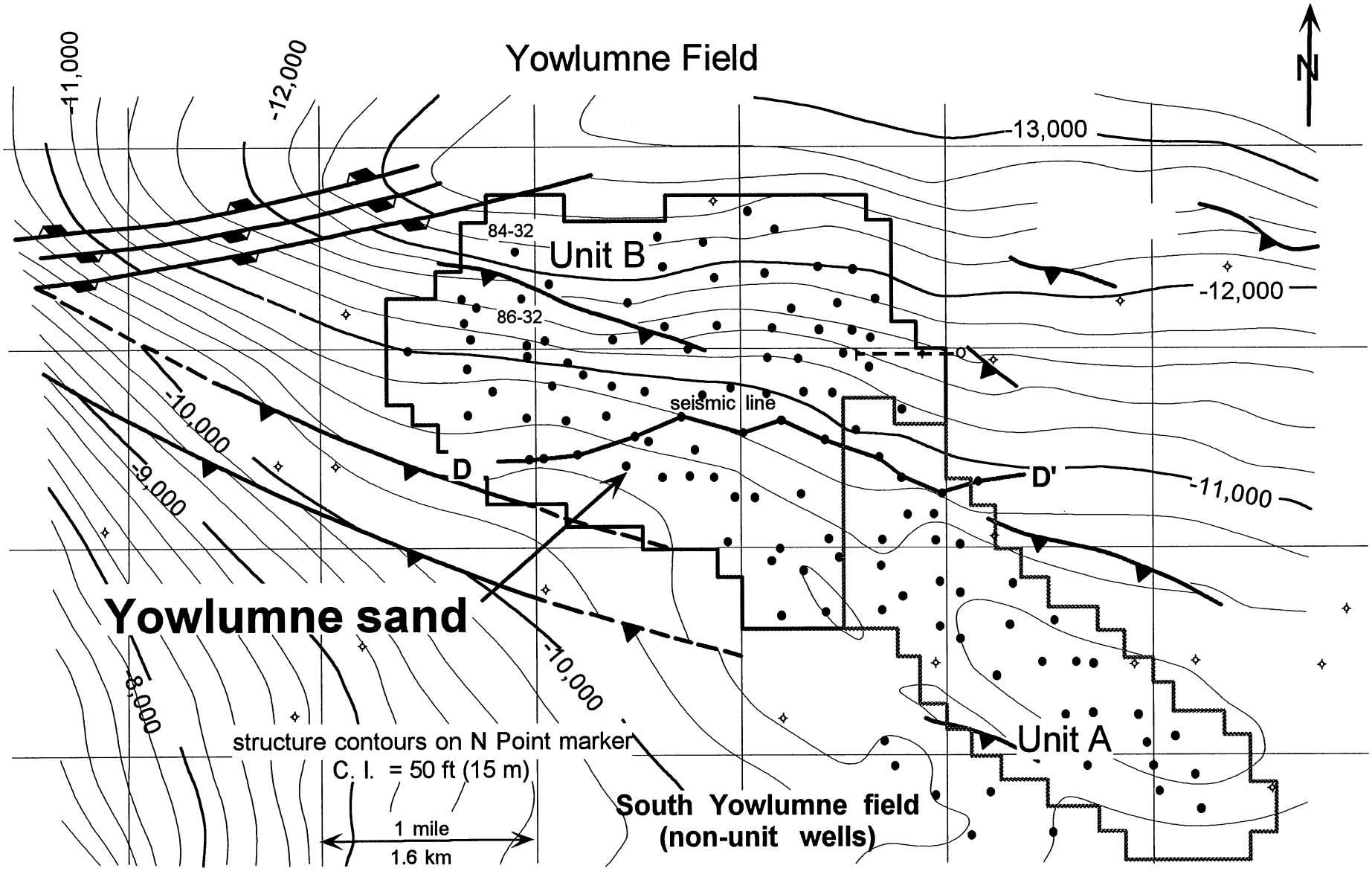

Figure 2: Structure map of the N-Point marker showing test well and monitor well.

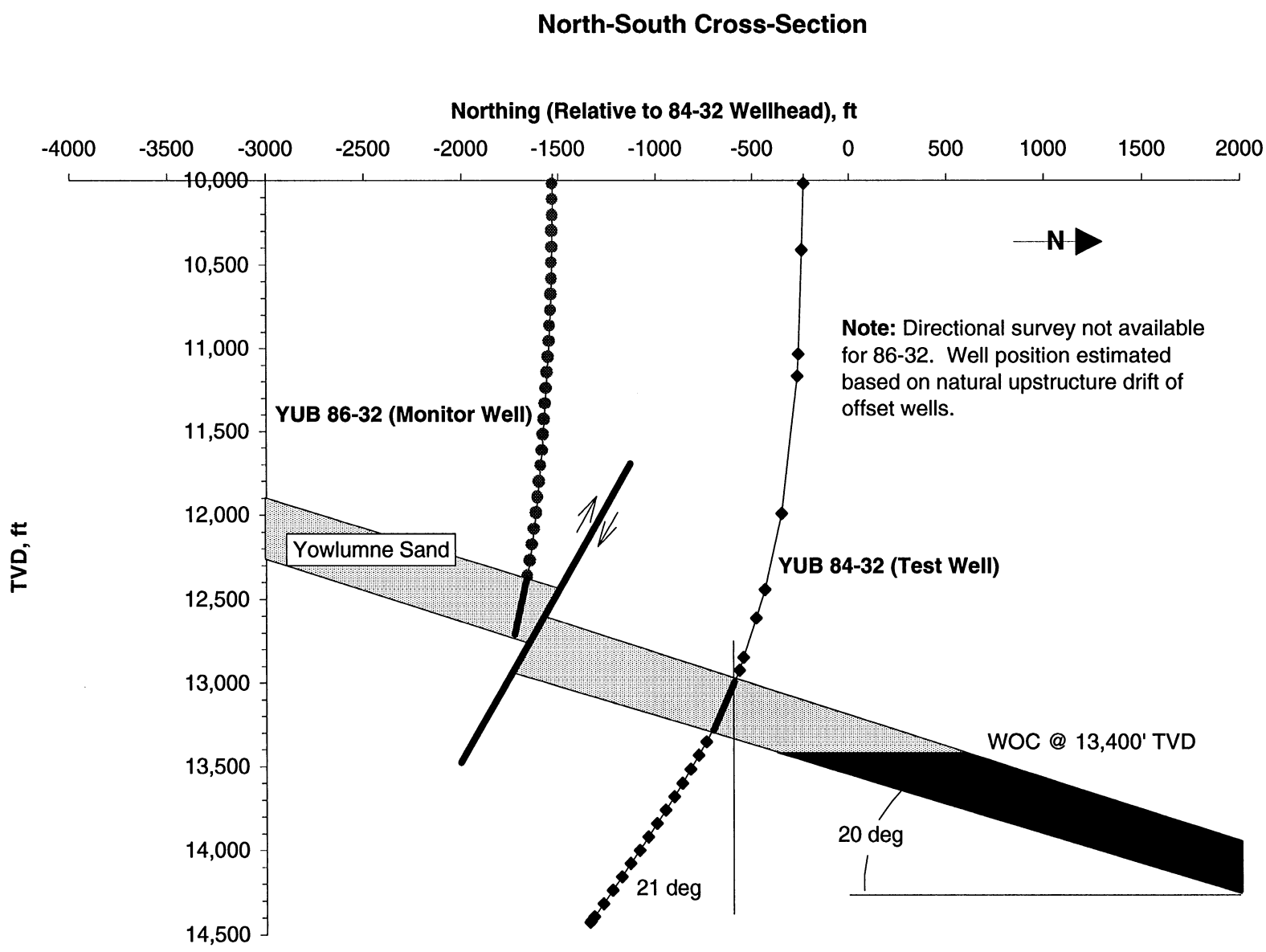

Figure 3: North-South cross-sectional schematic depicting test well and monitor well

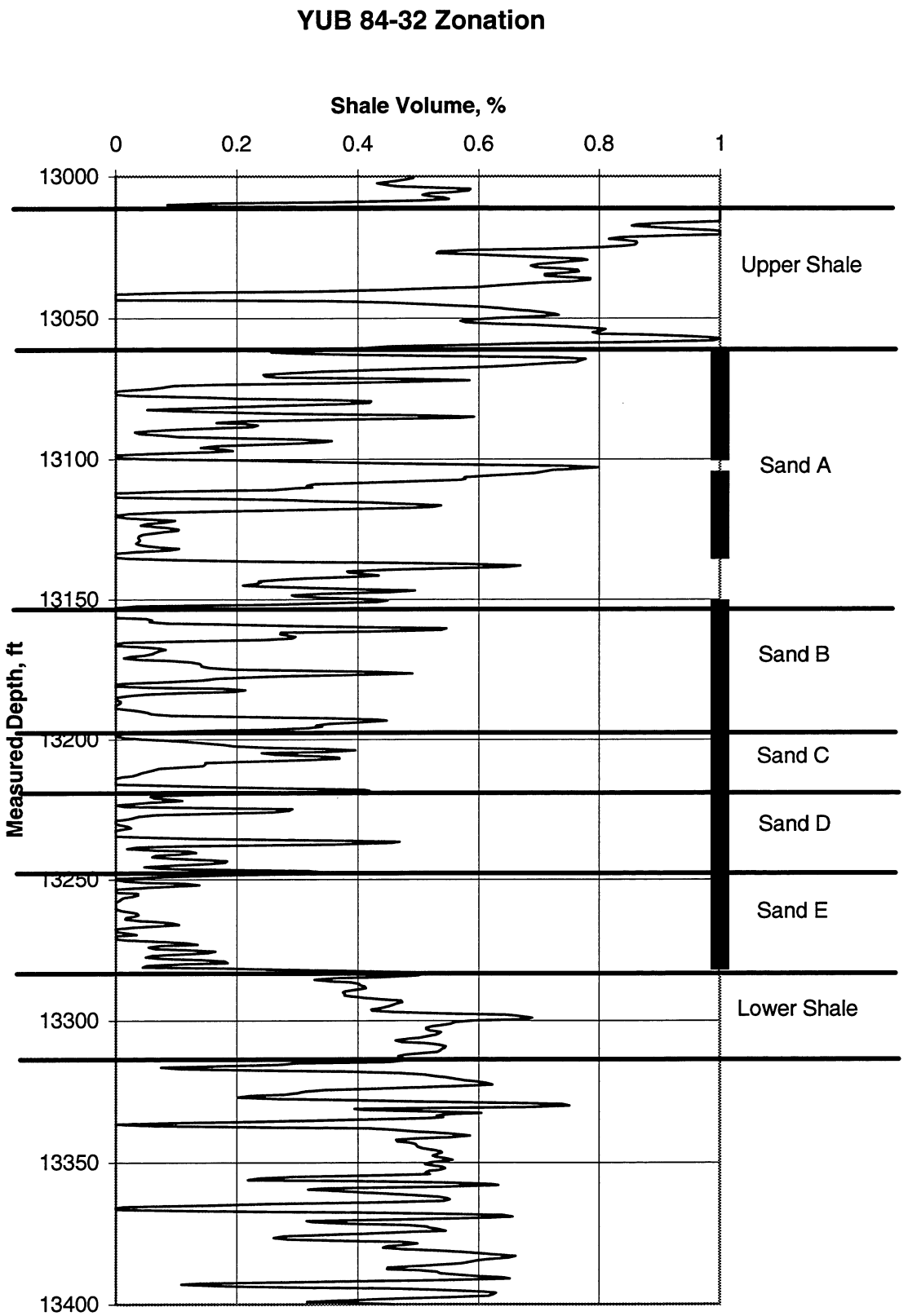

Figure 4: Type log of test well identifying flow units

Shmax from Borehole Breakout Data

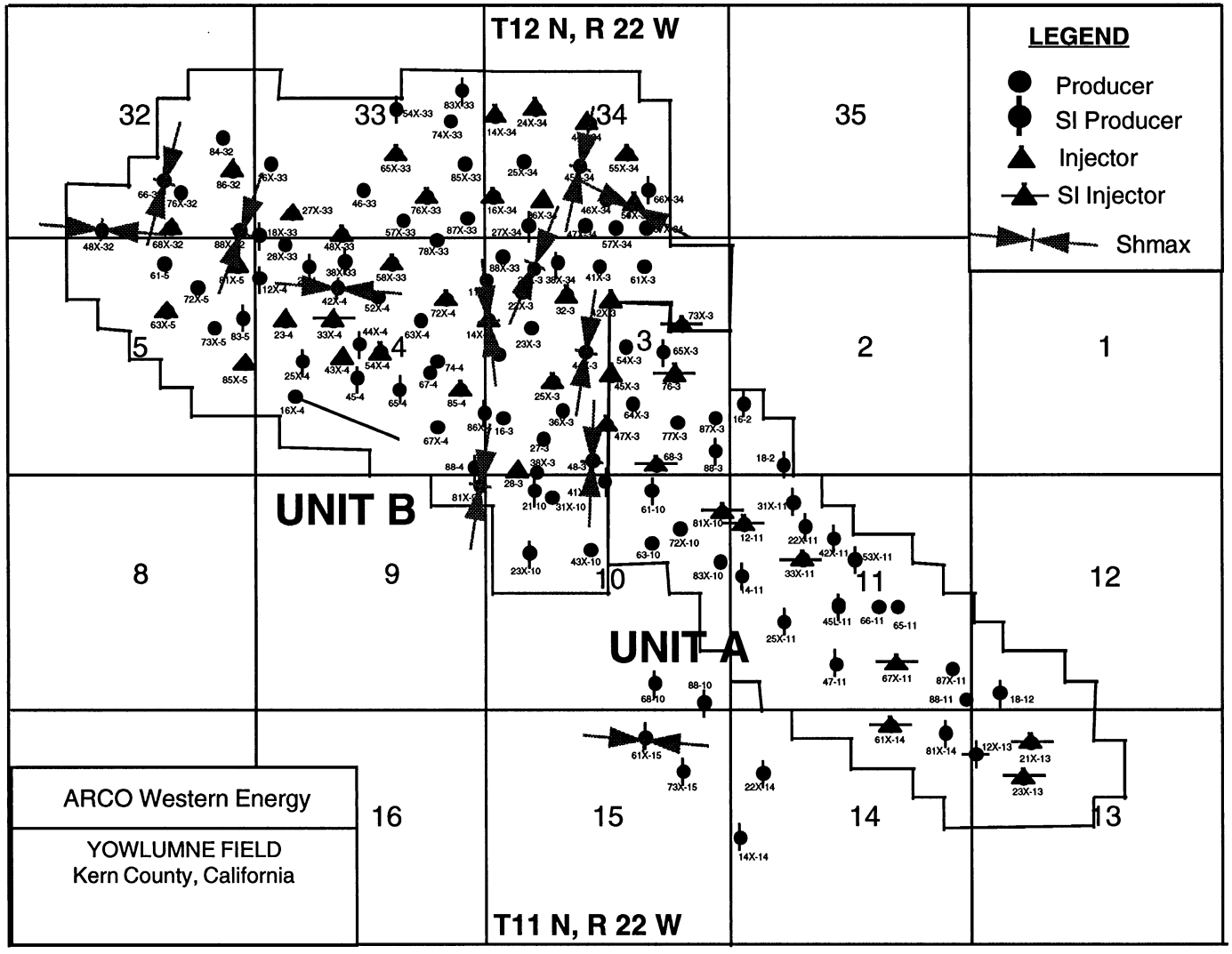

Figure 5: Shmax from borehole breakout data.

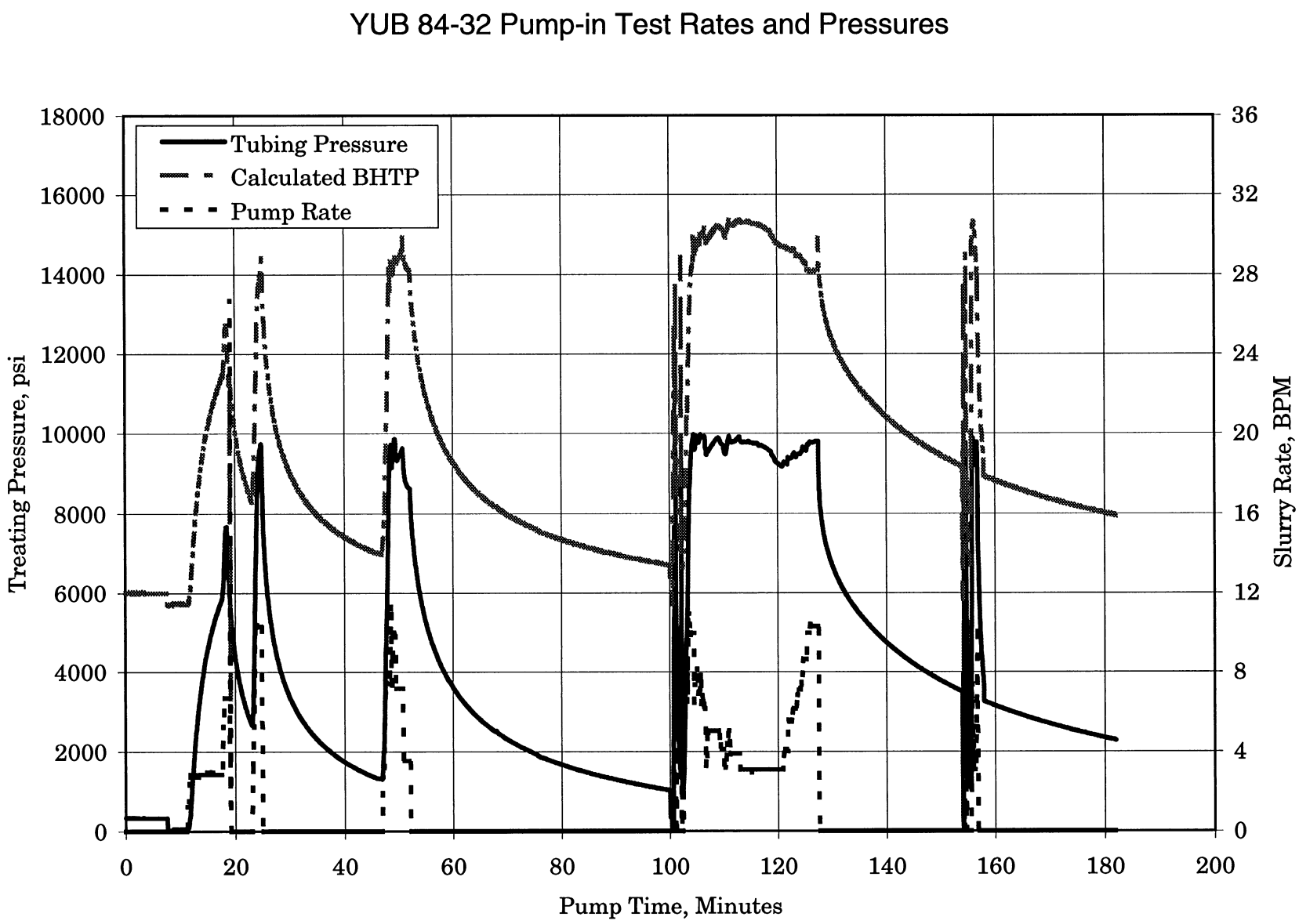

Figure 6: Treating pressures and rates from test well pump-in test.

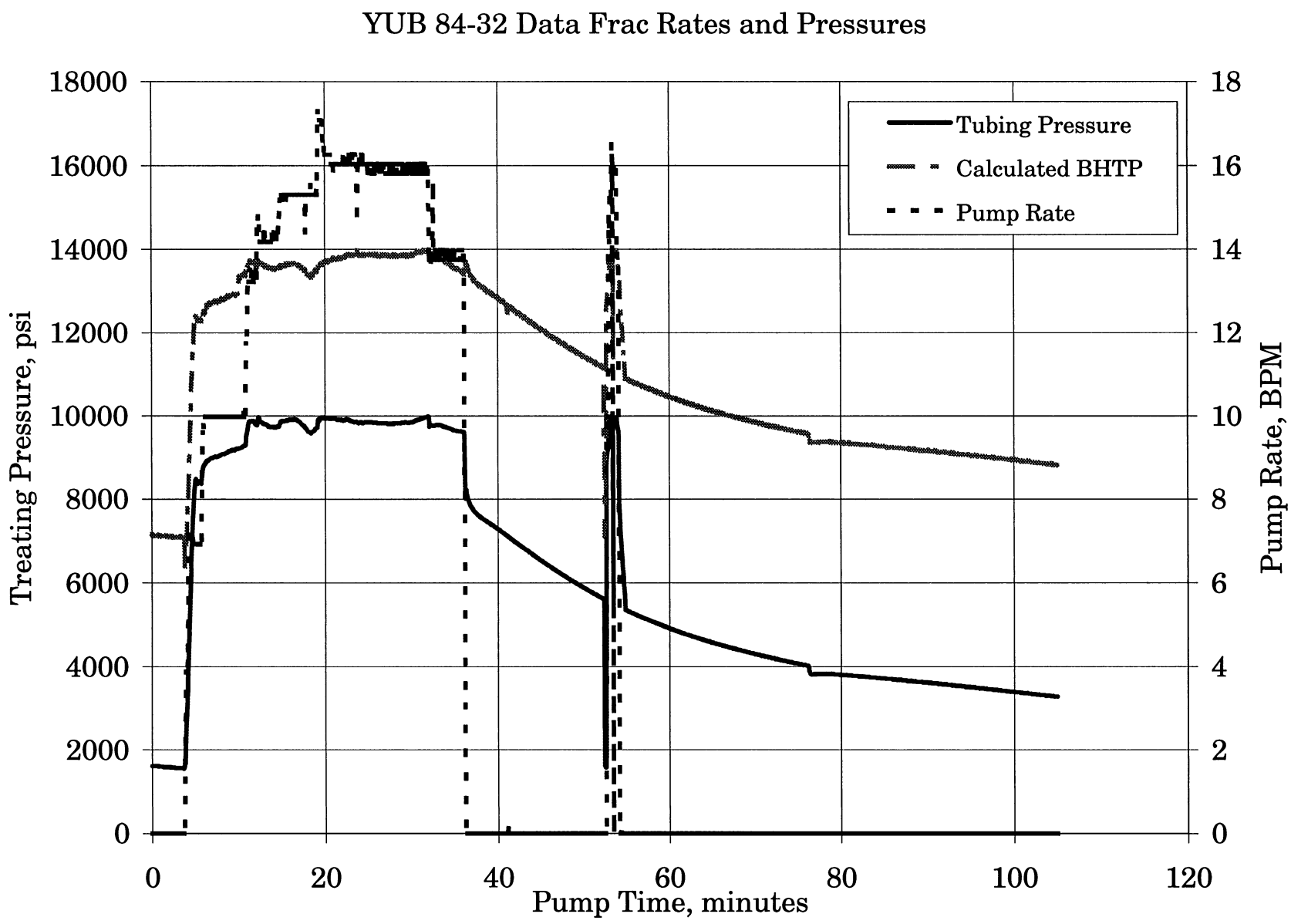

Figure 7: Treating pressures and rates from test well data frac.

YOWLUMNE UNIT B 84-32

POST-FRAC GAMMA RAY / TEMPERATURE LOG

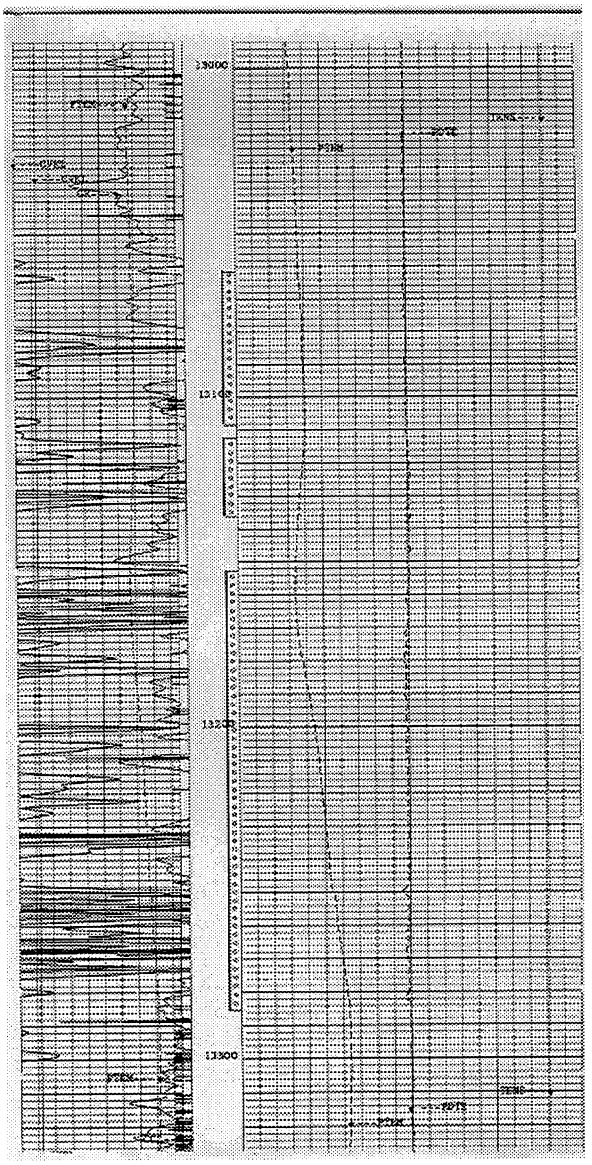

Figure 8: Post data frac gamma ray / temperature log on test well.

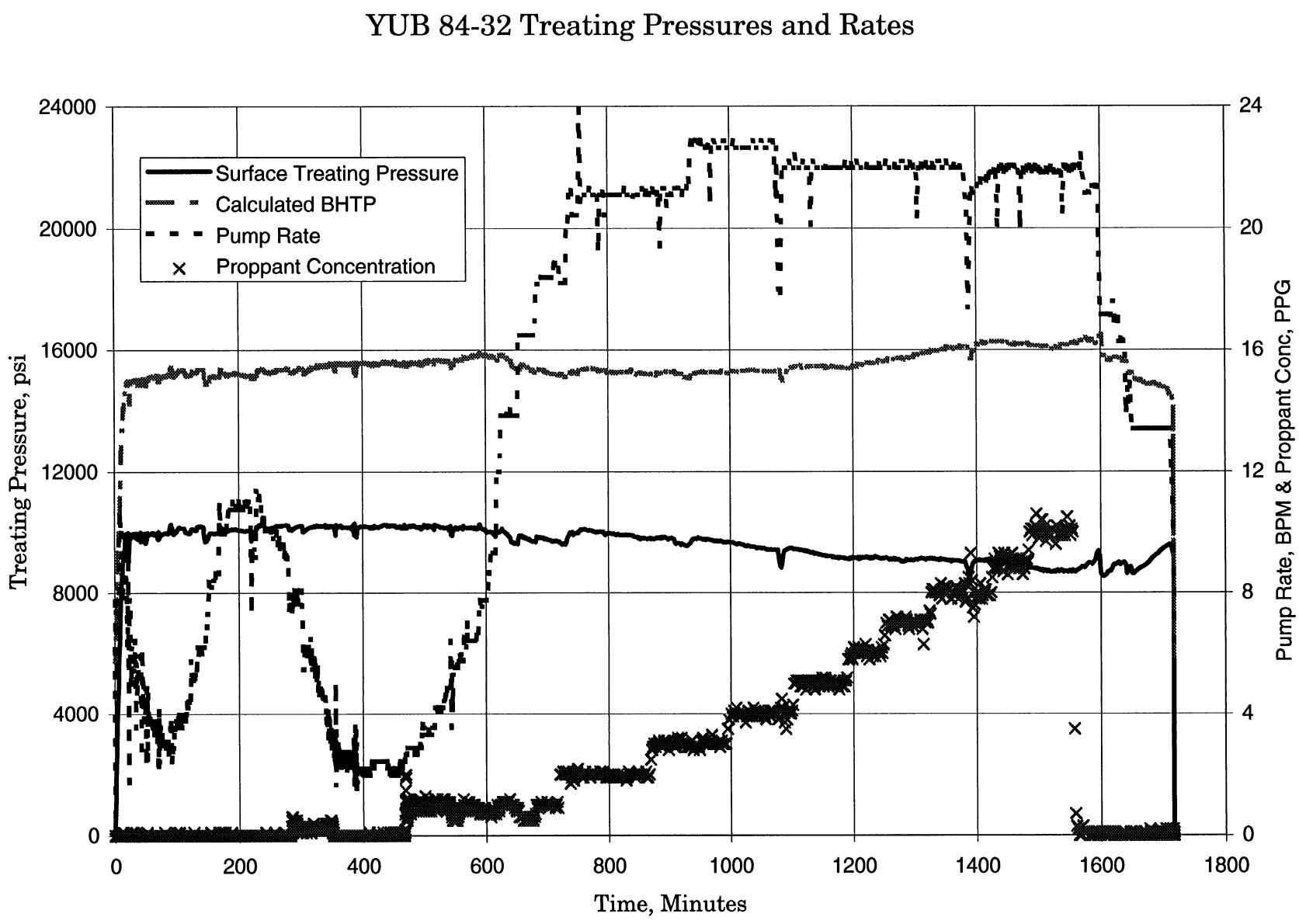

Figure 9: Treating pressures and rates from test well propped frac.

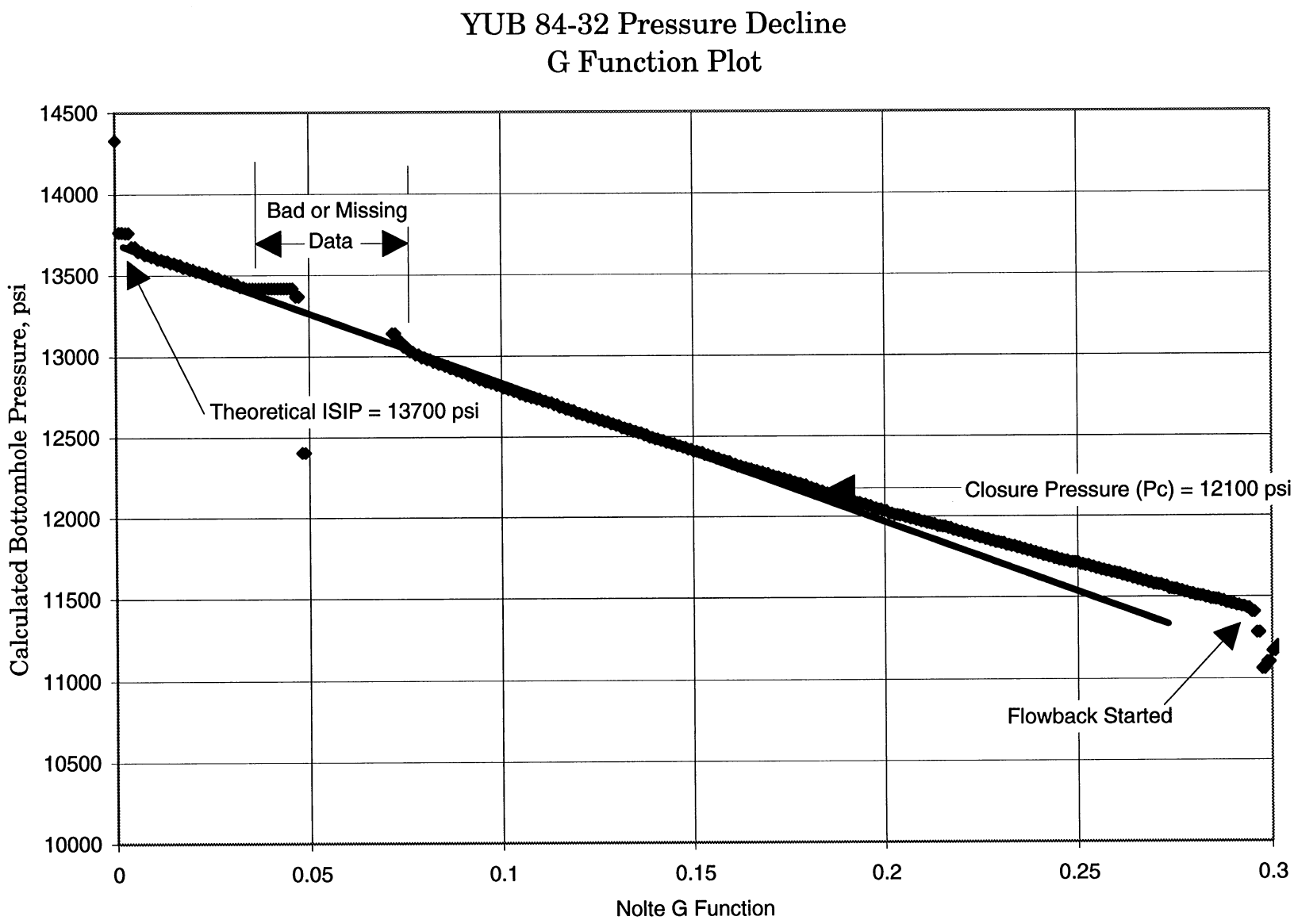

Figure 10: G Function plot of test well propped frac pressure decline

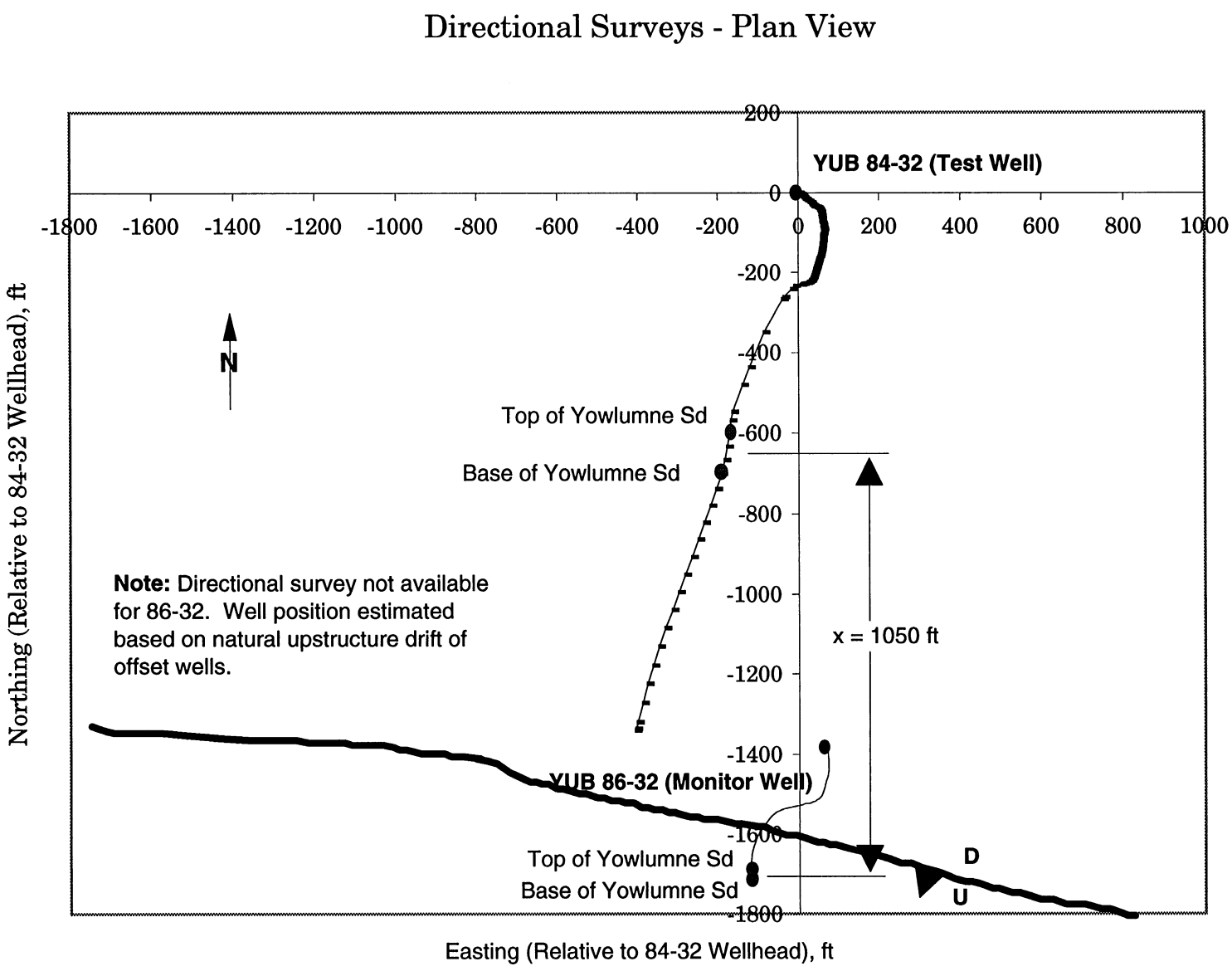

Figure 11: Directional surveys of test well and monitor well (plan view)

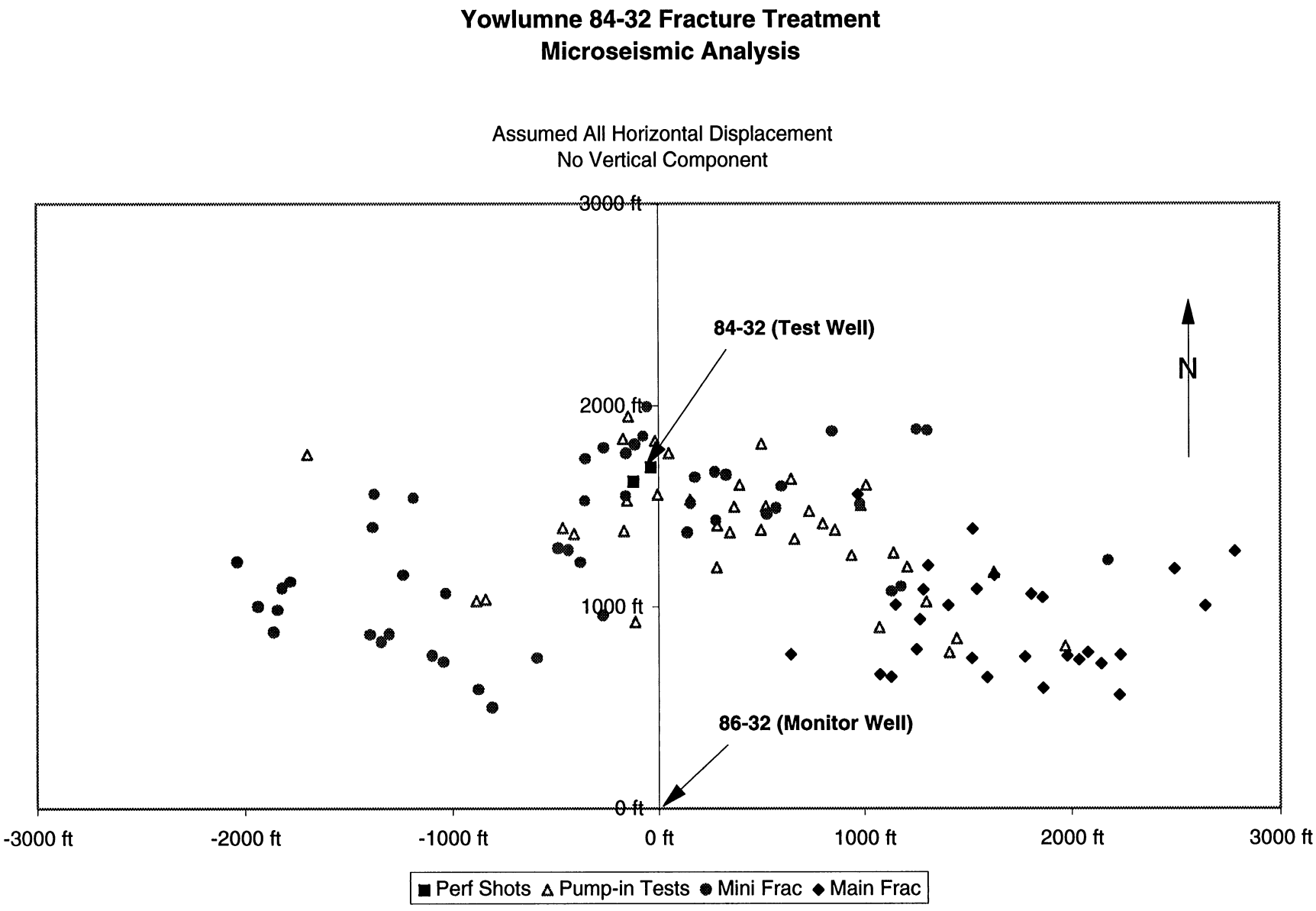

Figure 12: Microseismic events recorded in monitor well (plan view)

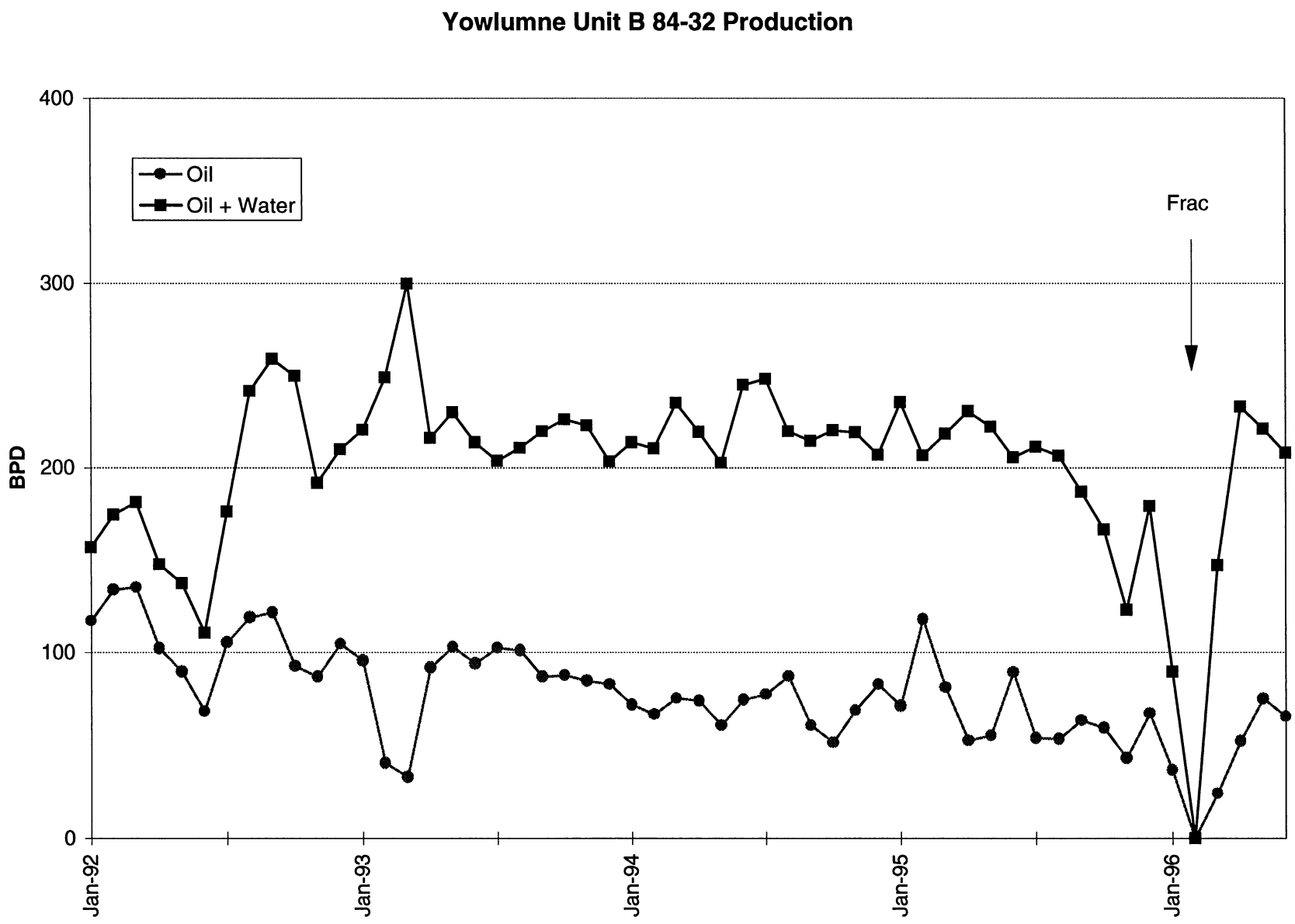

Figure 13: Test well production plot.

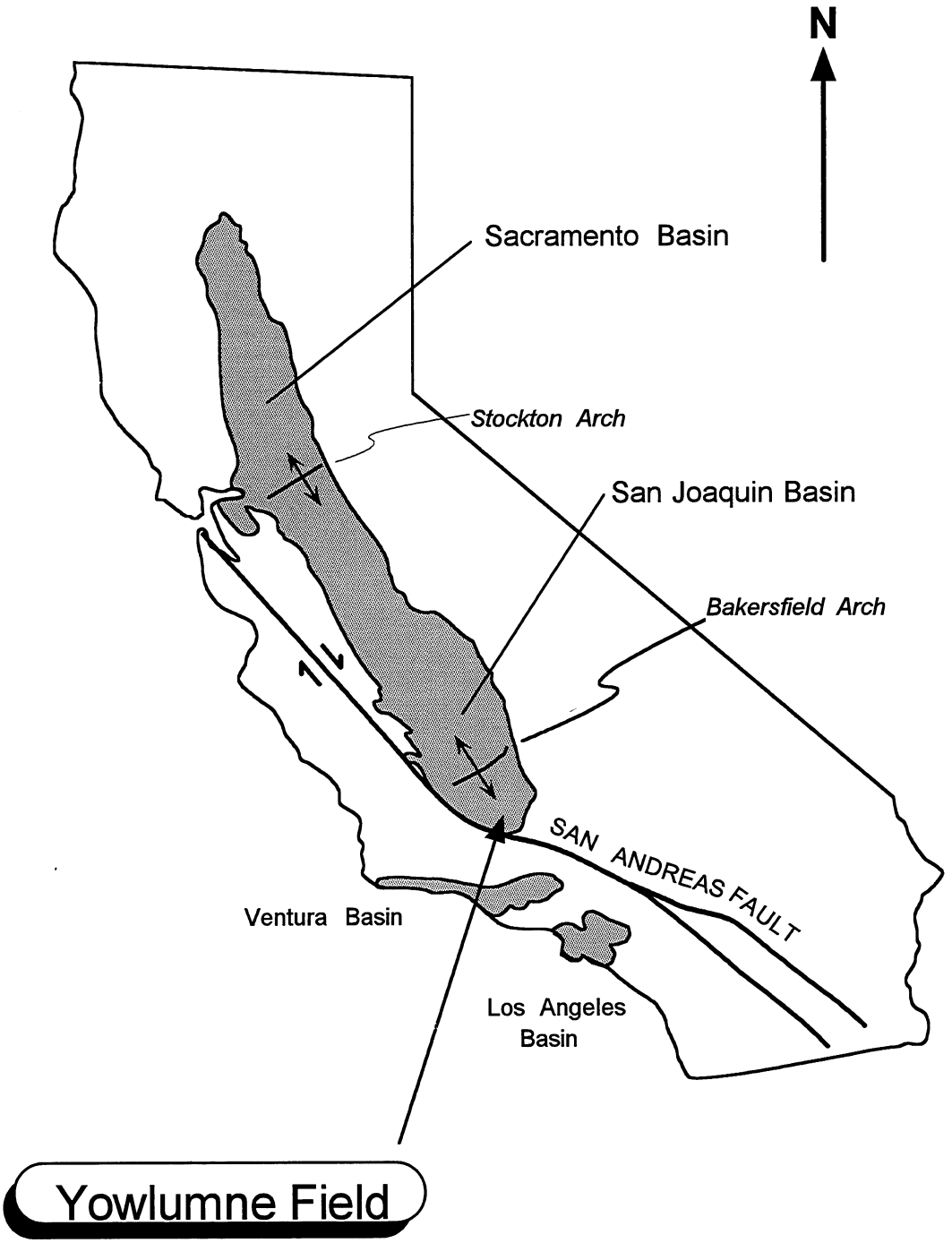

Figure 14: Map of California showing location of the San Joaquin Valley in relation to other oil-producing basins in the state.

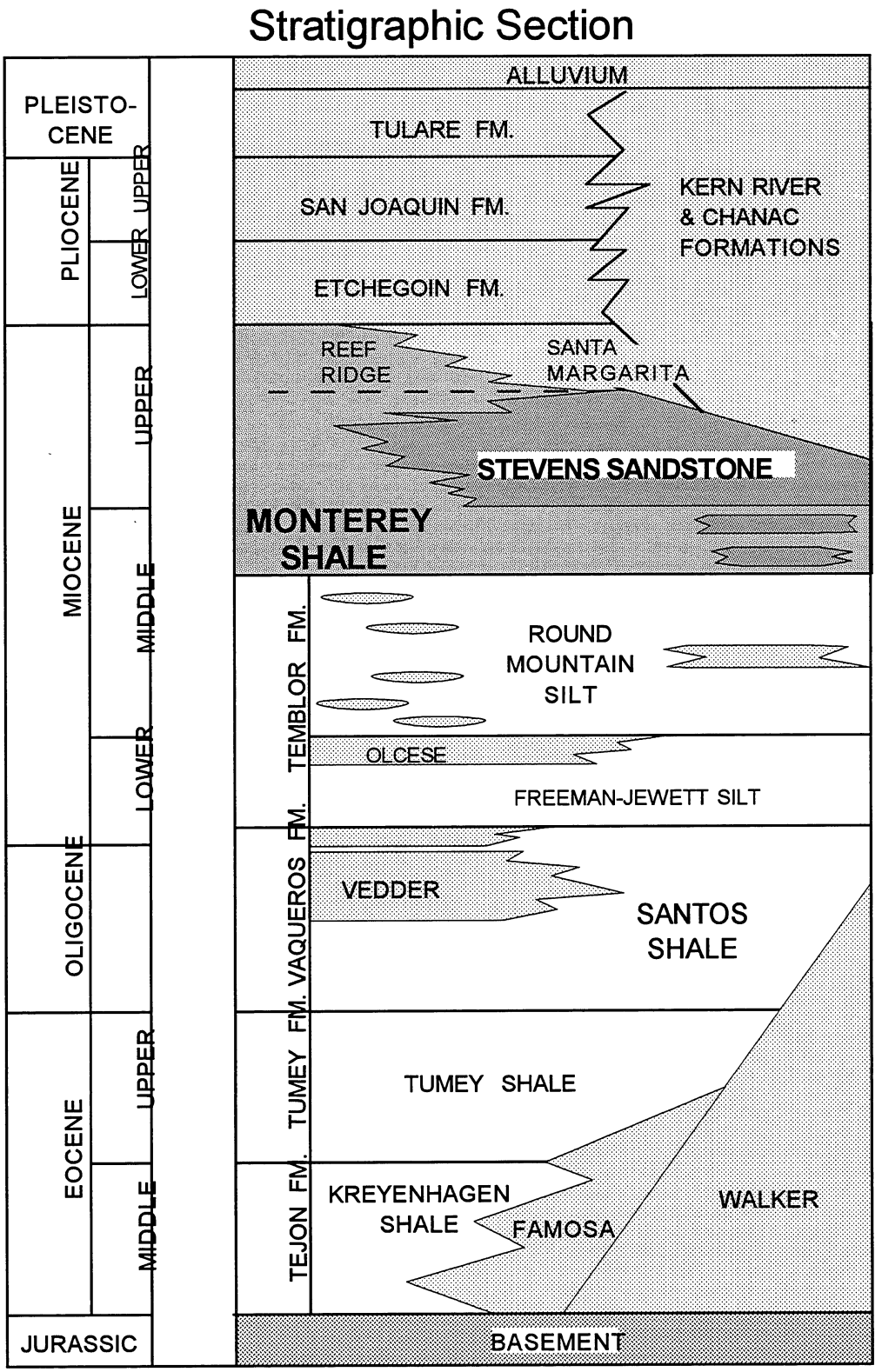

Figure 15: Stratigraphic section for the southern San Joaquin Valley basin showing the Monterey-Stevens petroleum system.

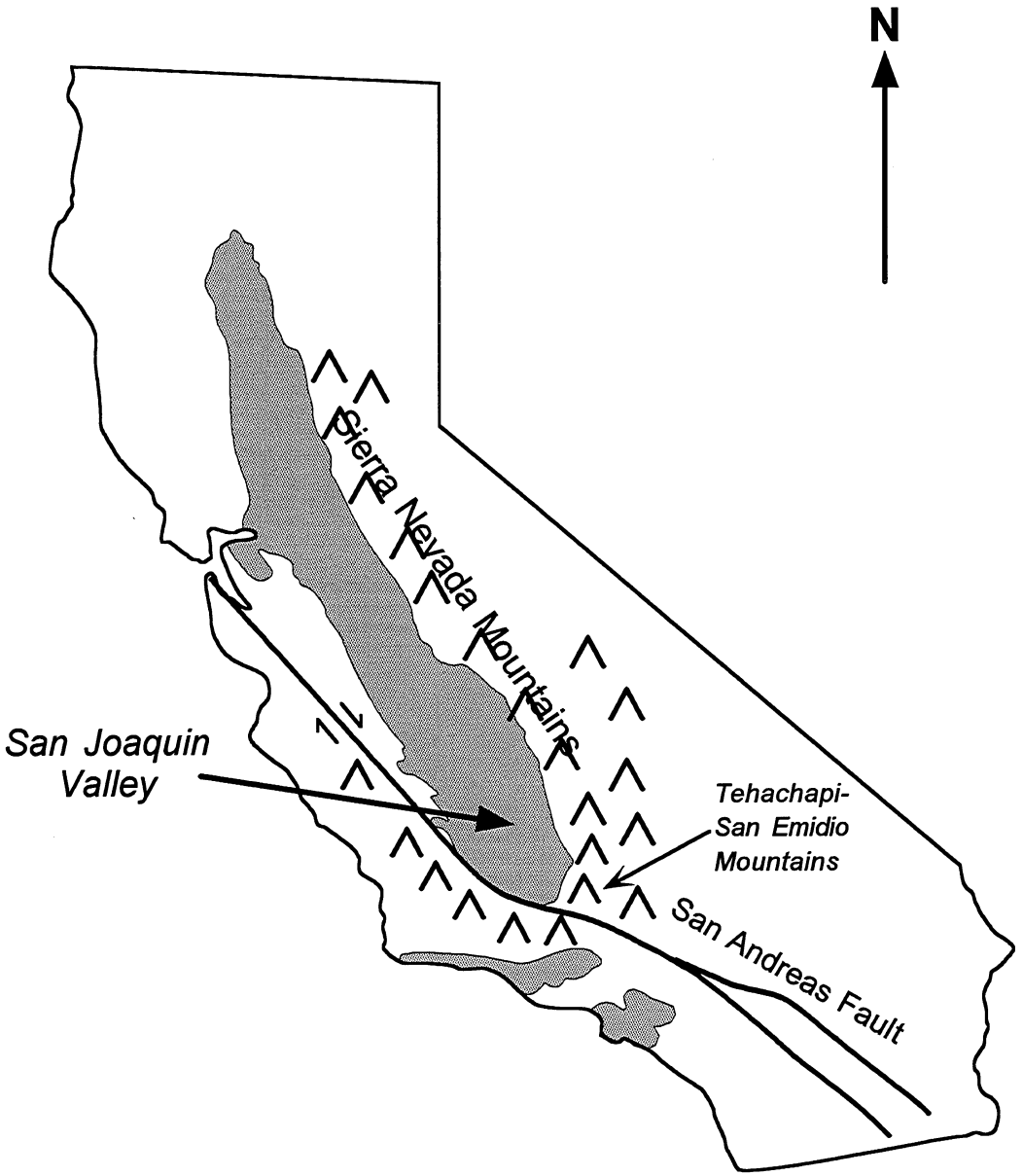

Figure 16: Map of California showing the principle geomorphic provinces surrounding the southern San Joaquin basin.

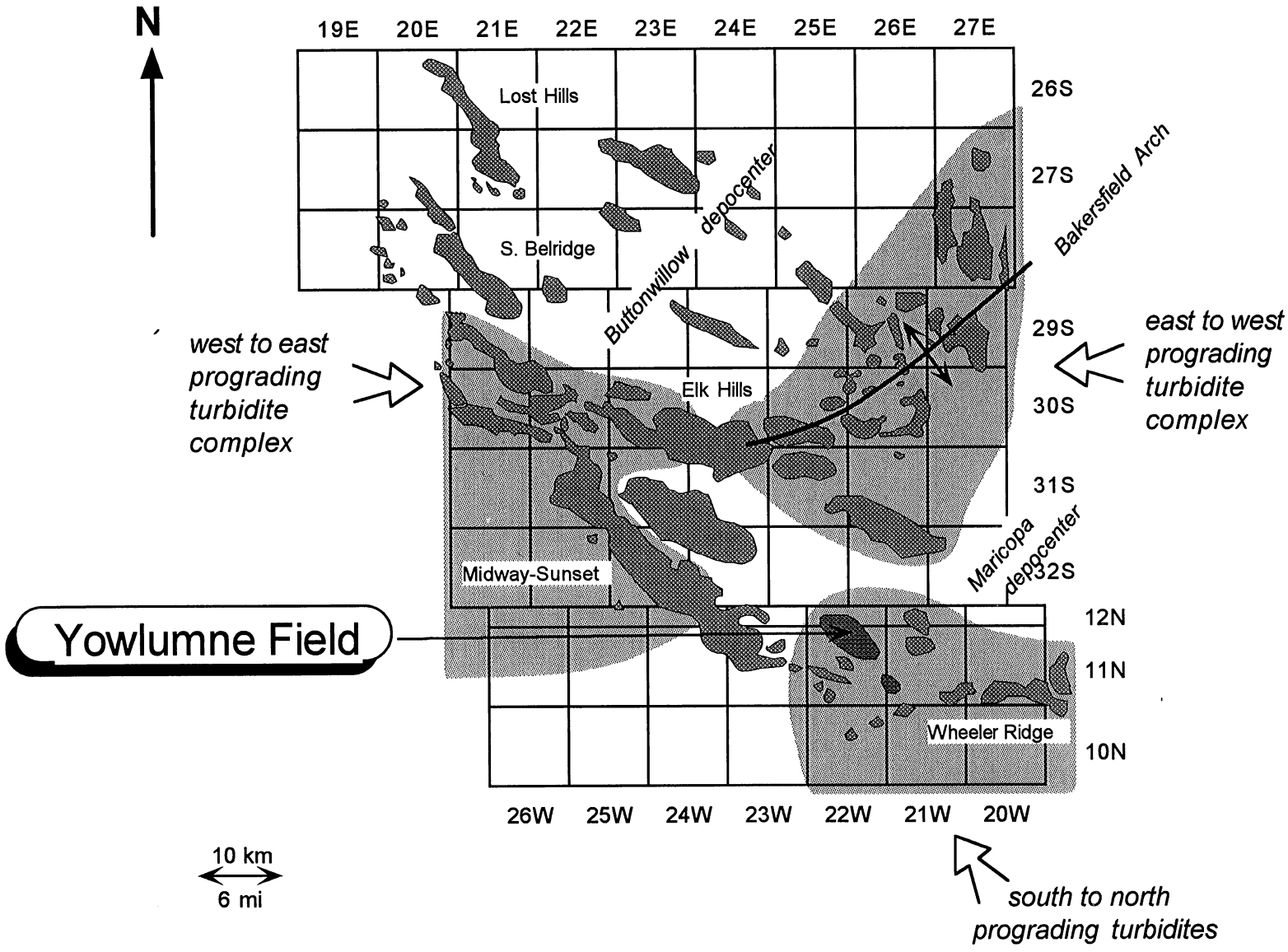

Figure 17: Map of the southern San Joaquin basin showing the distribution of three main depositional systems represented by the Stevens sandstone (modified from Clark et al., 1996a).

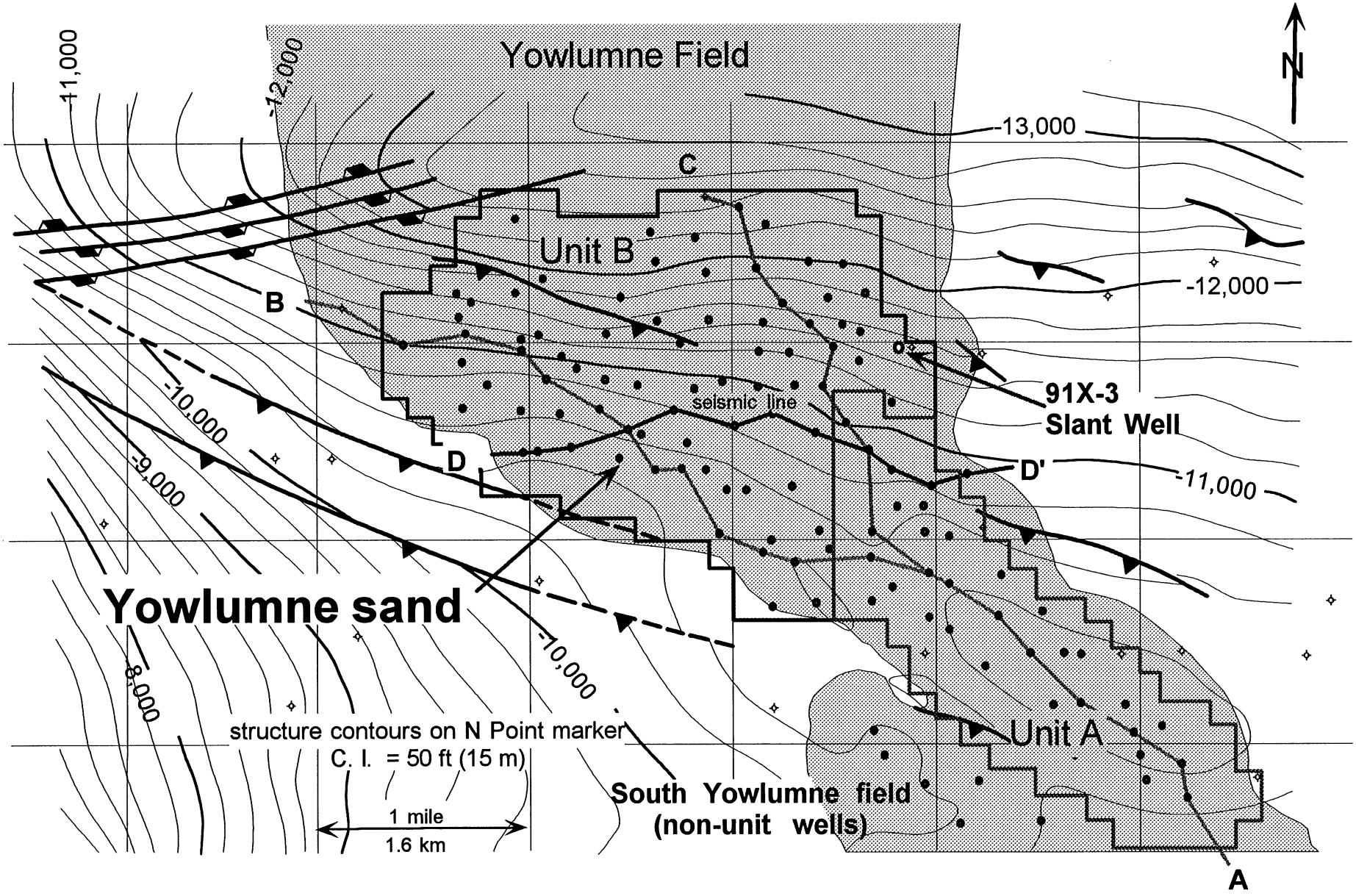

Figure 18: Structure map drawn on the N-point marker showing the relationship of Units A and B to the Yowlumne field anticline.

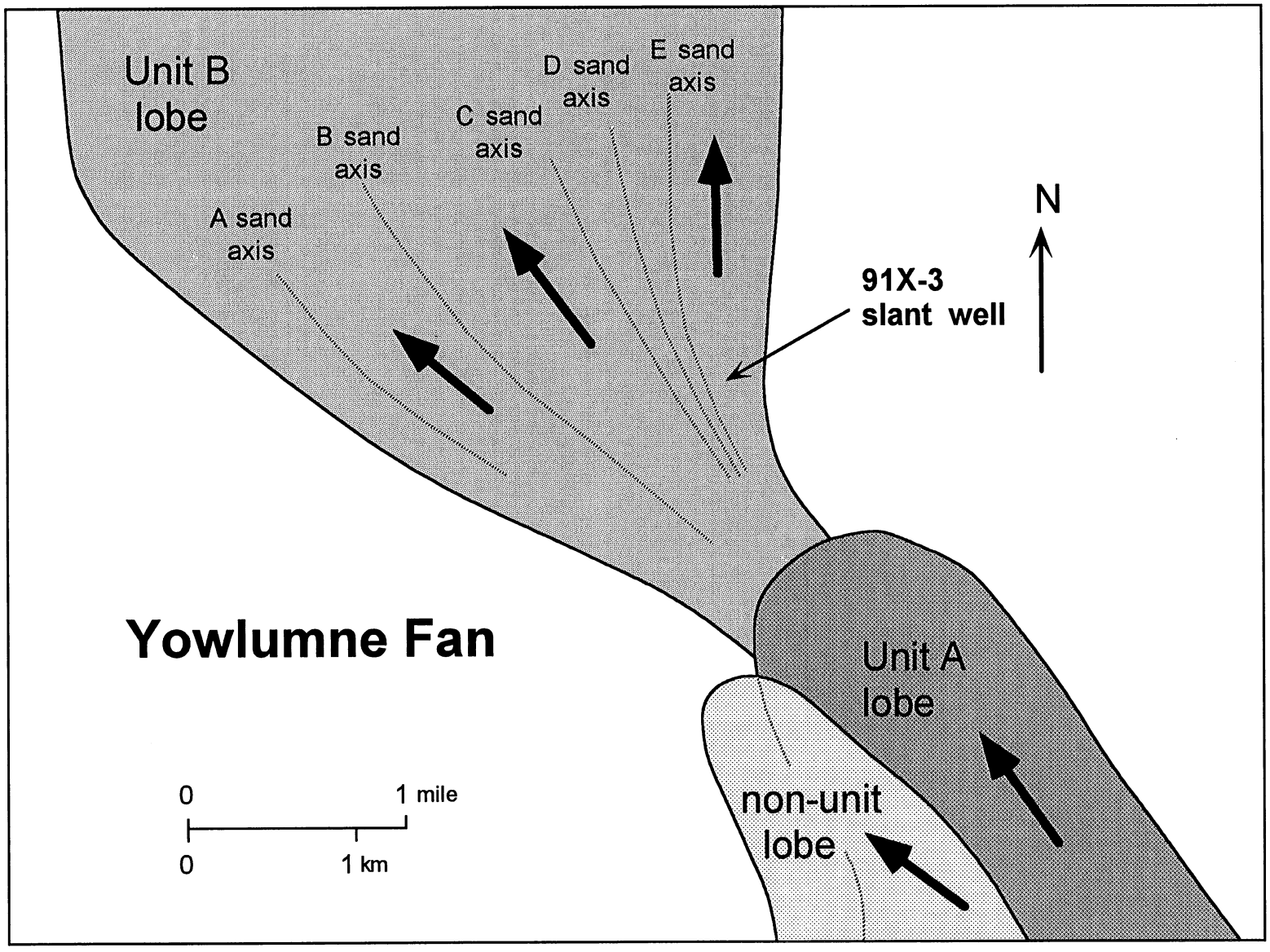

Figure 19: Map showing left-stepping and basinward-stepping geometries exhibited by depositional lobes that compose the Yowlumne fan.

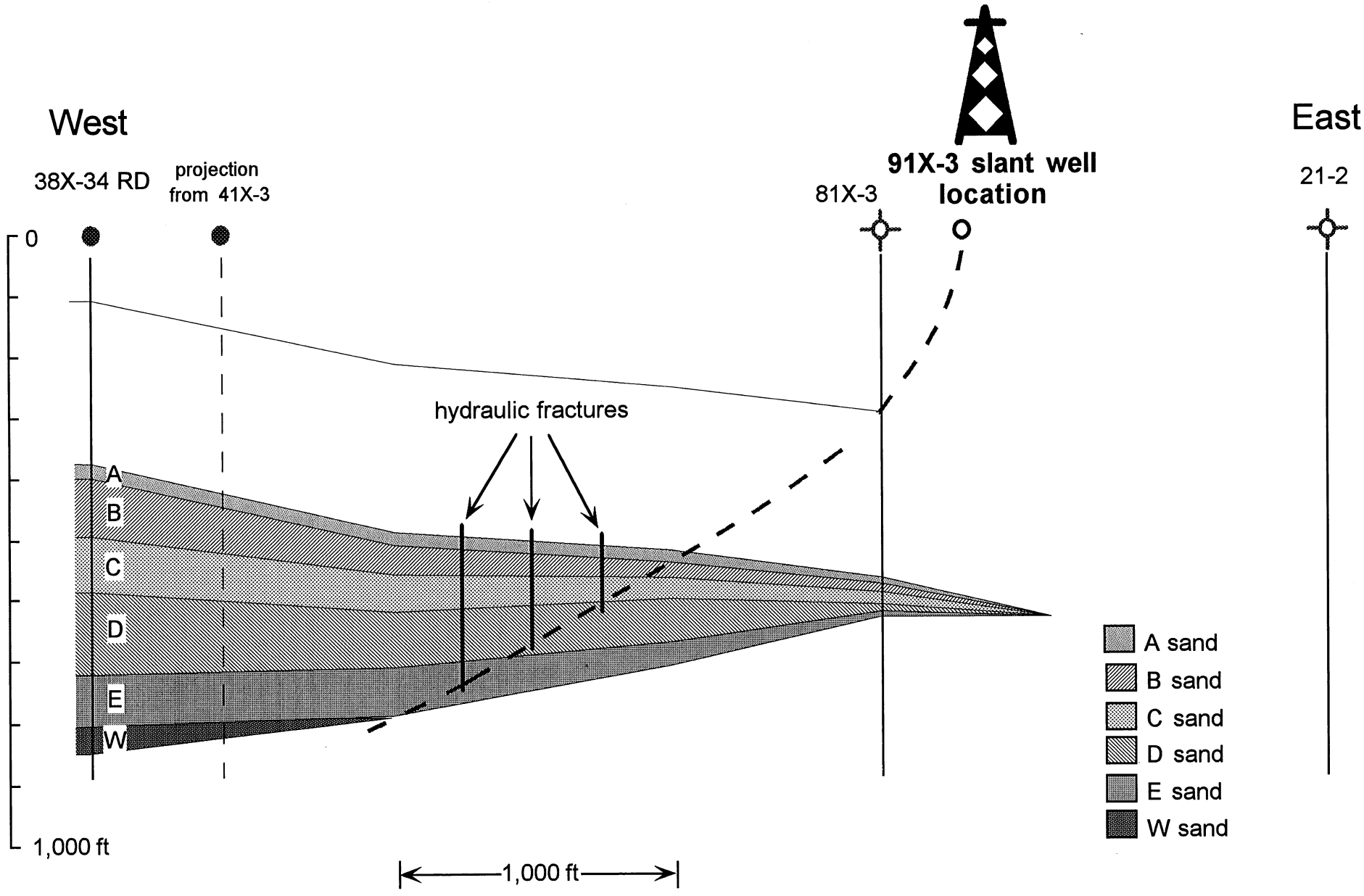

Figure 20: East-West cross-section showiing the five main reservoir layers in Unit B penetrated by the proposed slant well.

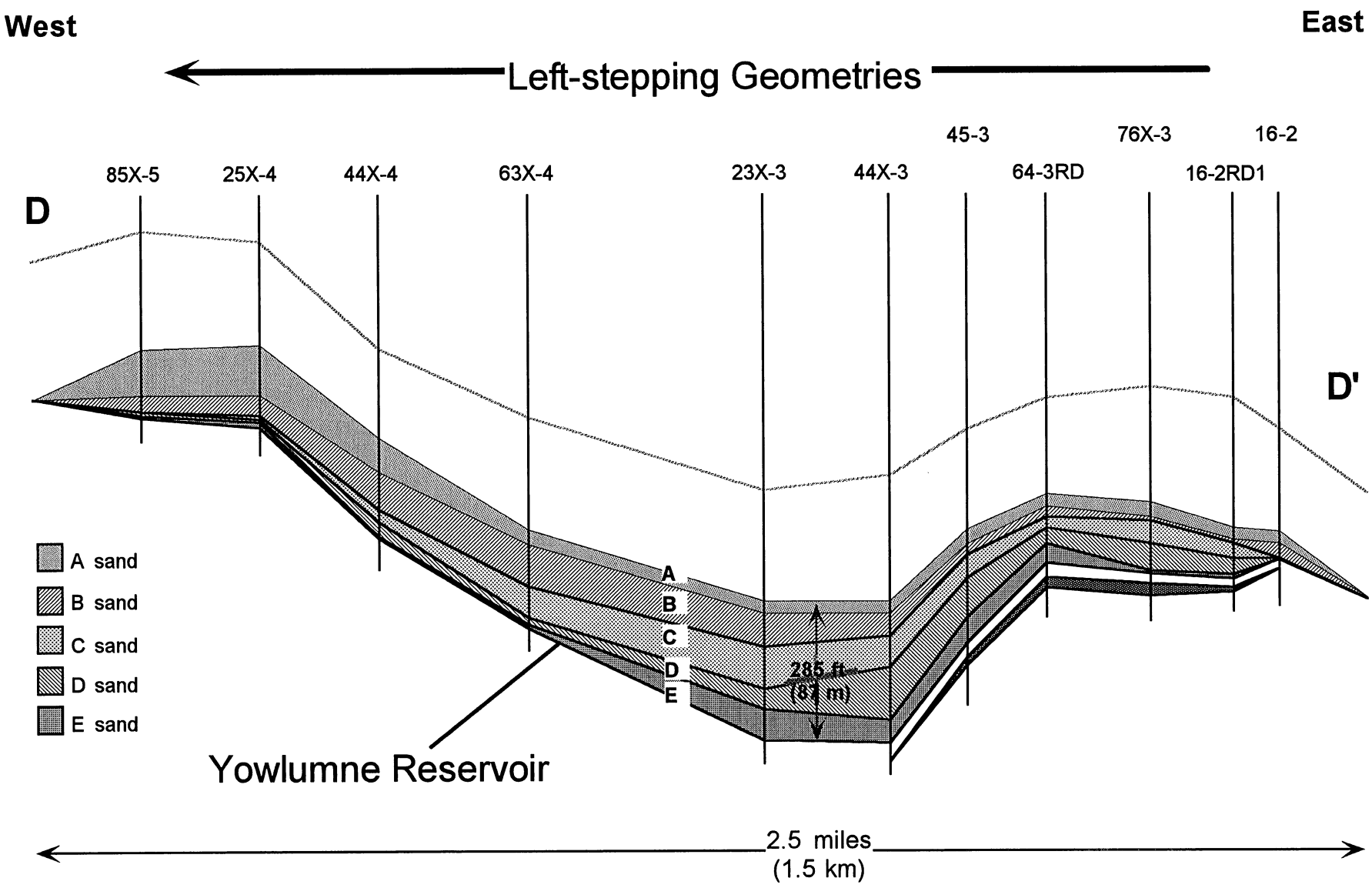

Figure 21: Cross-section showing the left-stepping geometry of the five main reservoir layers in Unit B.

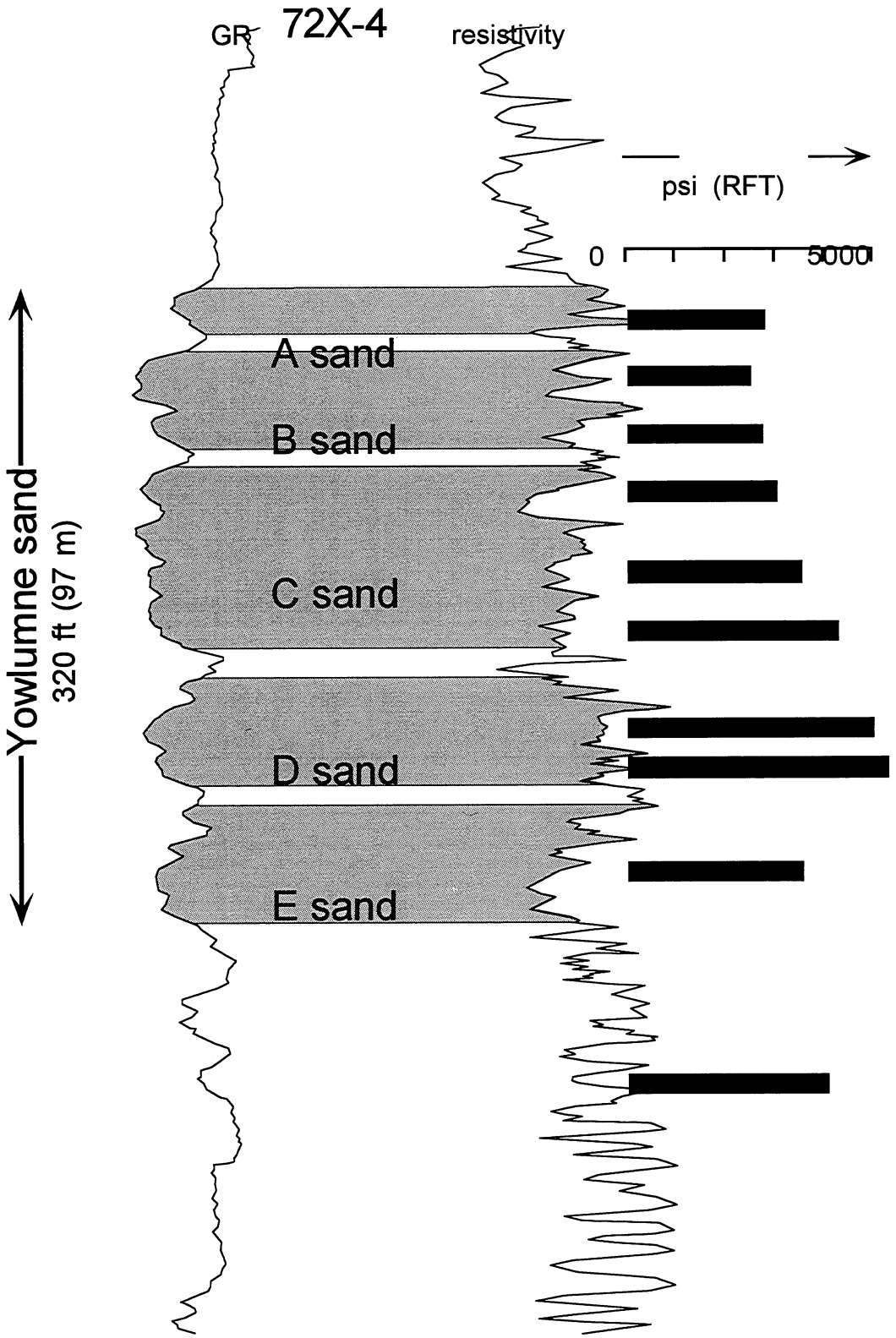

Figure 22: Reservoir compartments in the Yowlumne sand in the 72X-4 well indicated by pressure variations in an RFT survey.

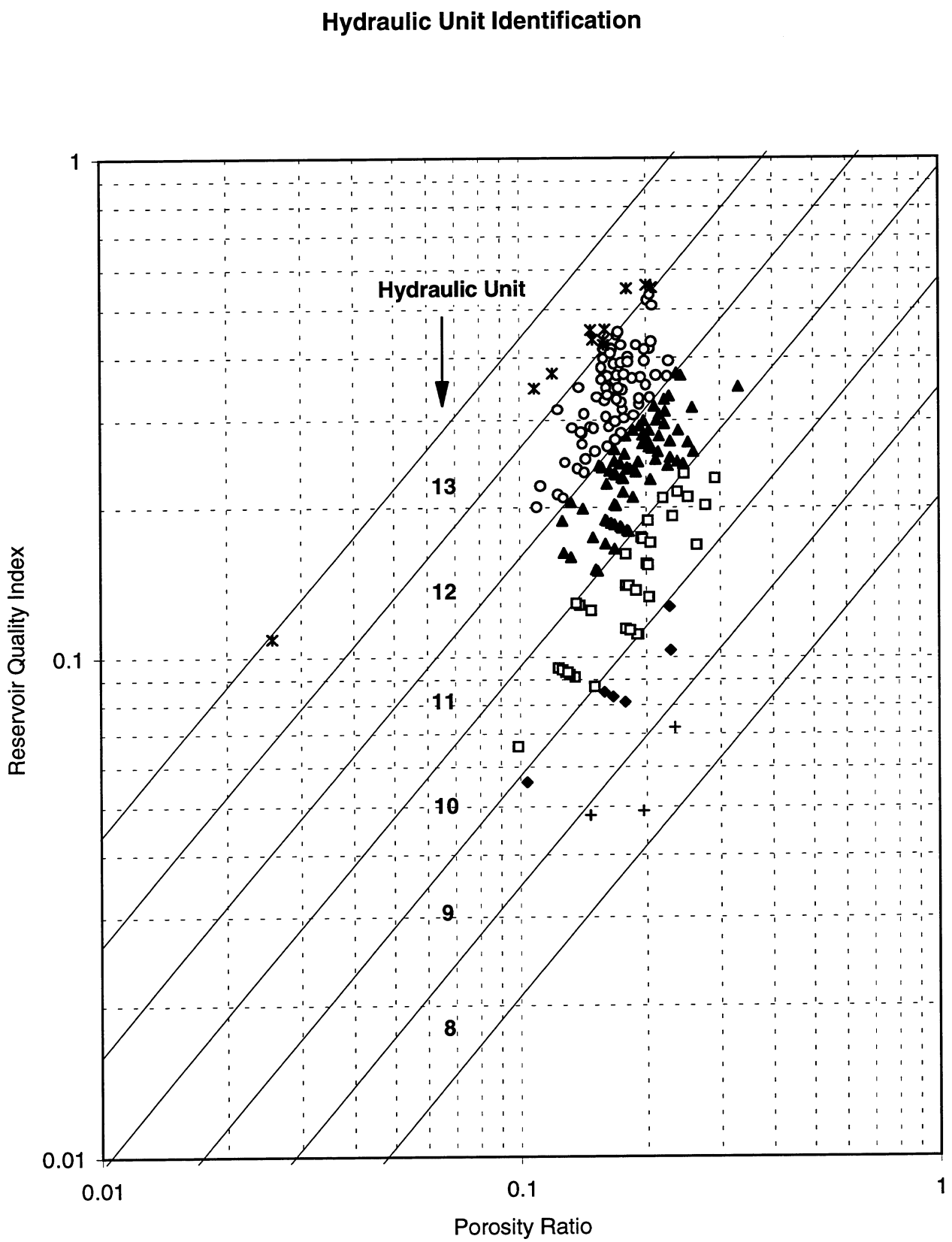

Figure 23: Plot of reservoir quality index vs. pore ratio for well 55X-34 showing hydraulic unit grouping.

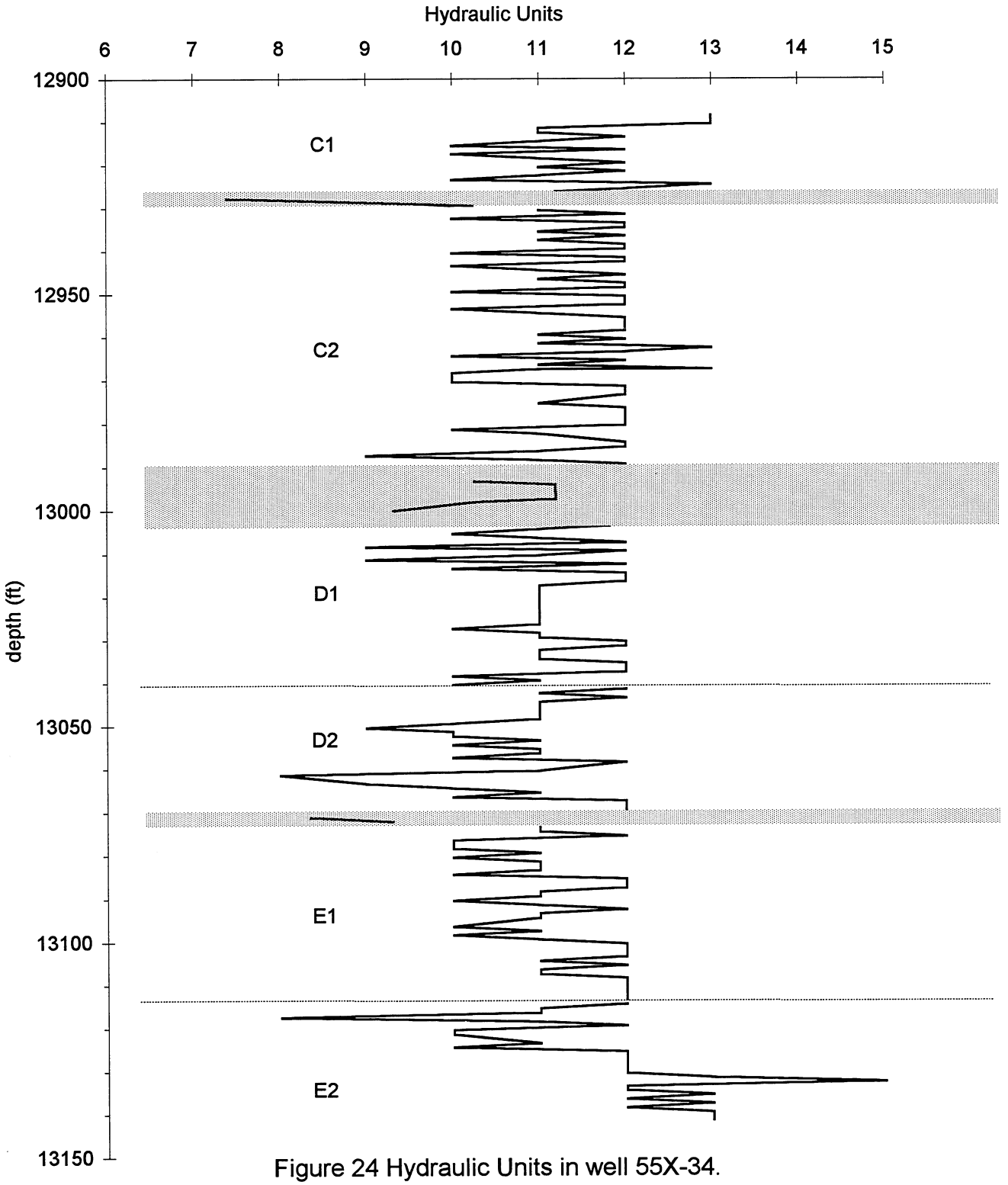

Figure 24 Hydraulic Units in well 55X-34.

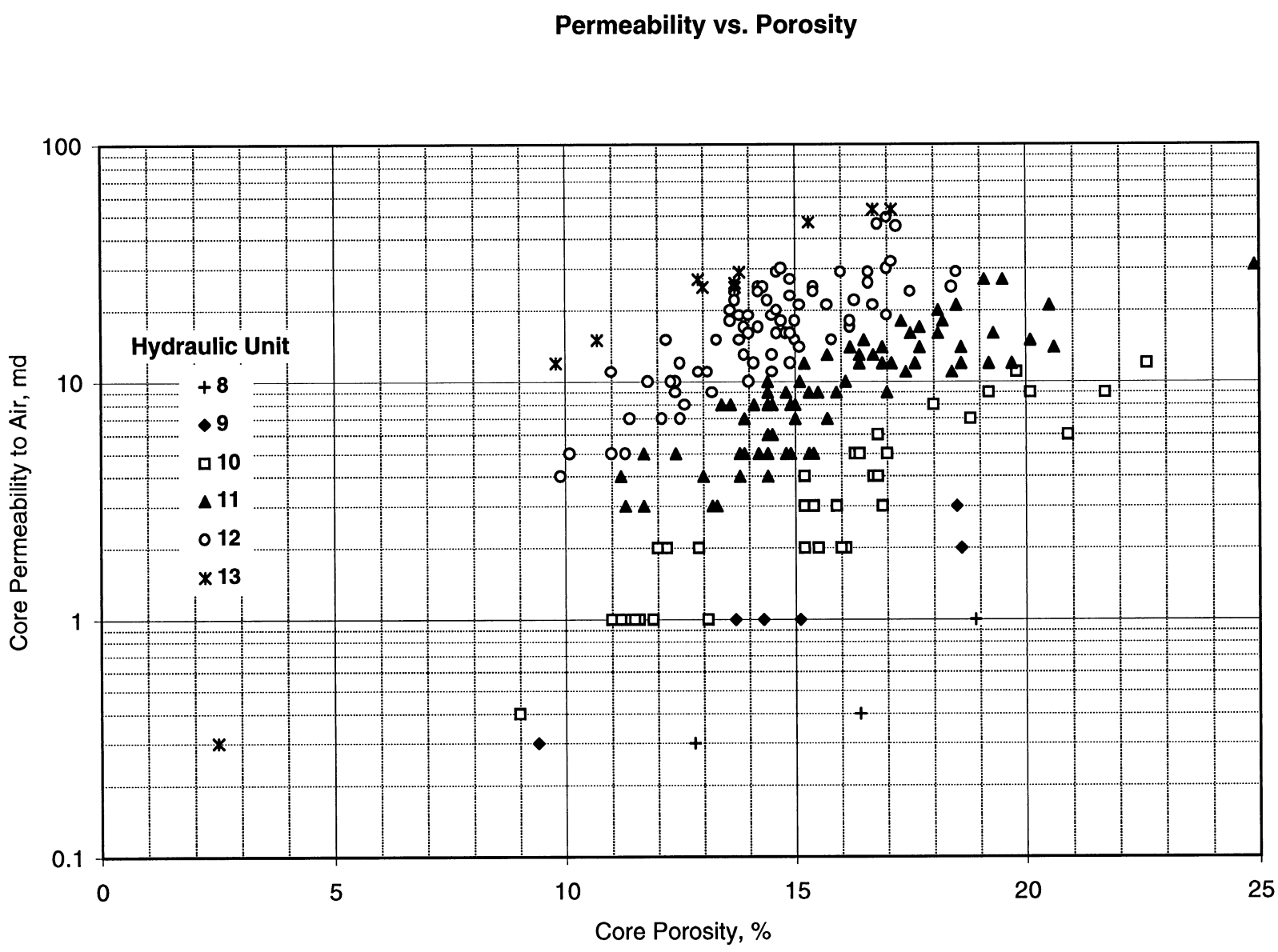

Figure 25: Crossplot of permeability vs. porosity for well 55X-34 grouped by hydraulic unit.

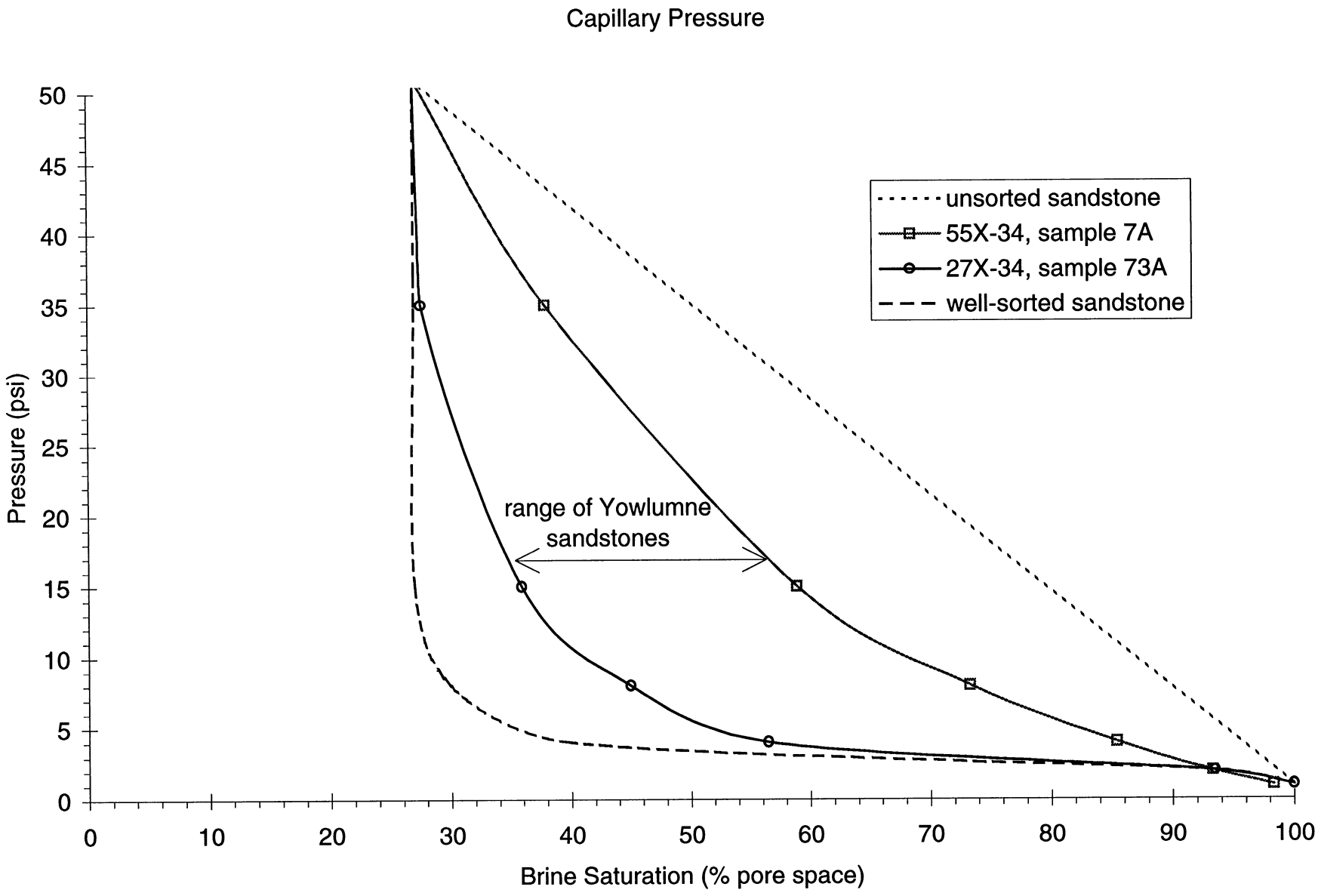

Figure 26: Degree of sorting indicated by shape of mercury injection curves.

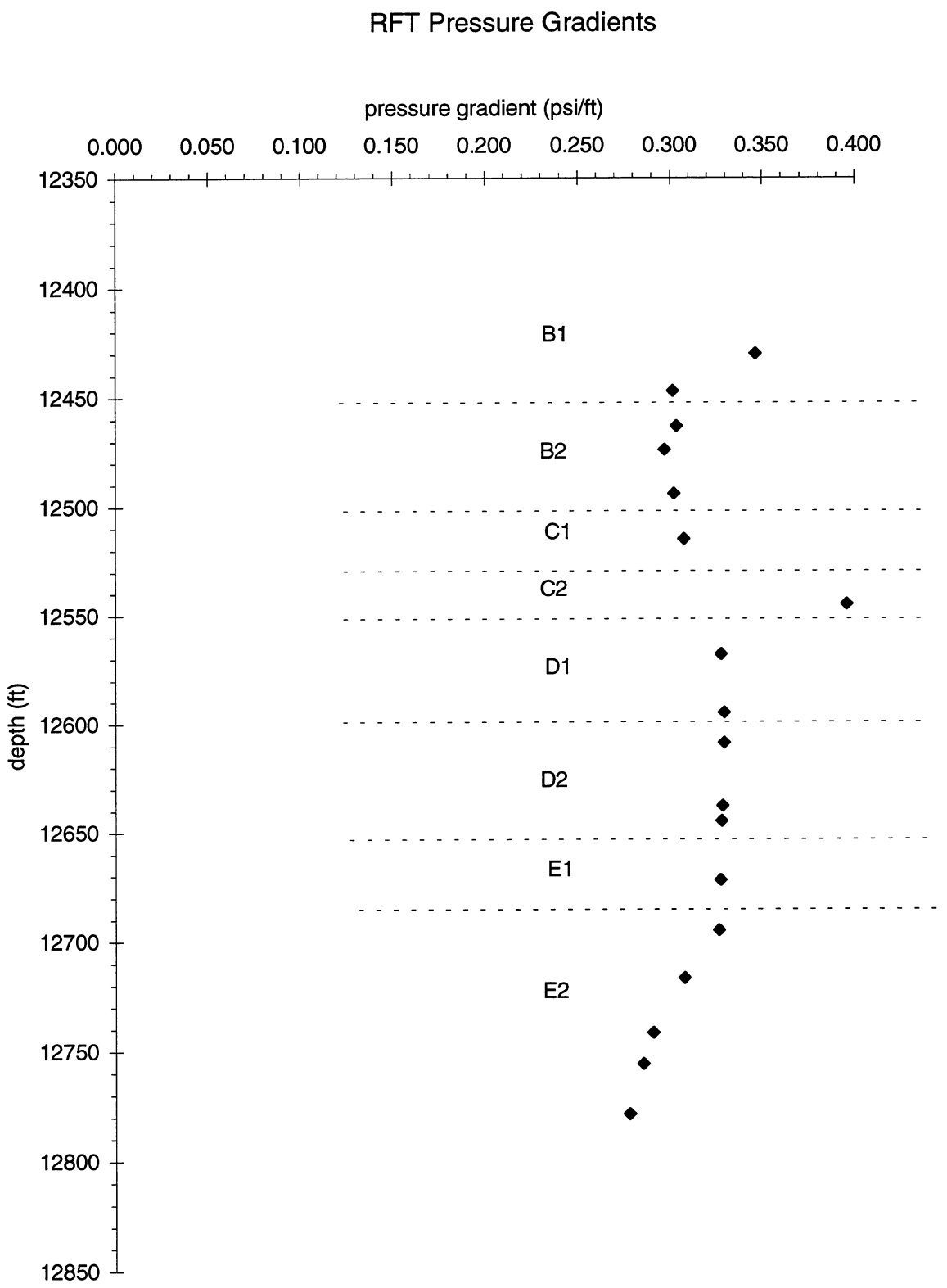

Figure 27: RFT pressure gradients for well 57X-34.

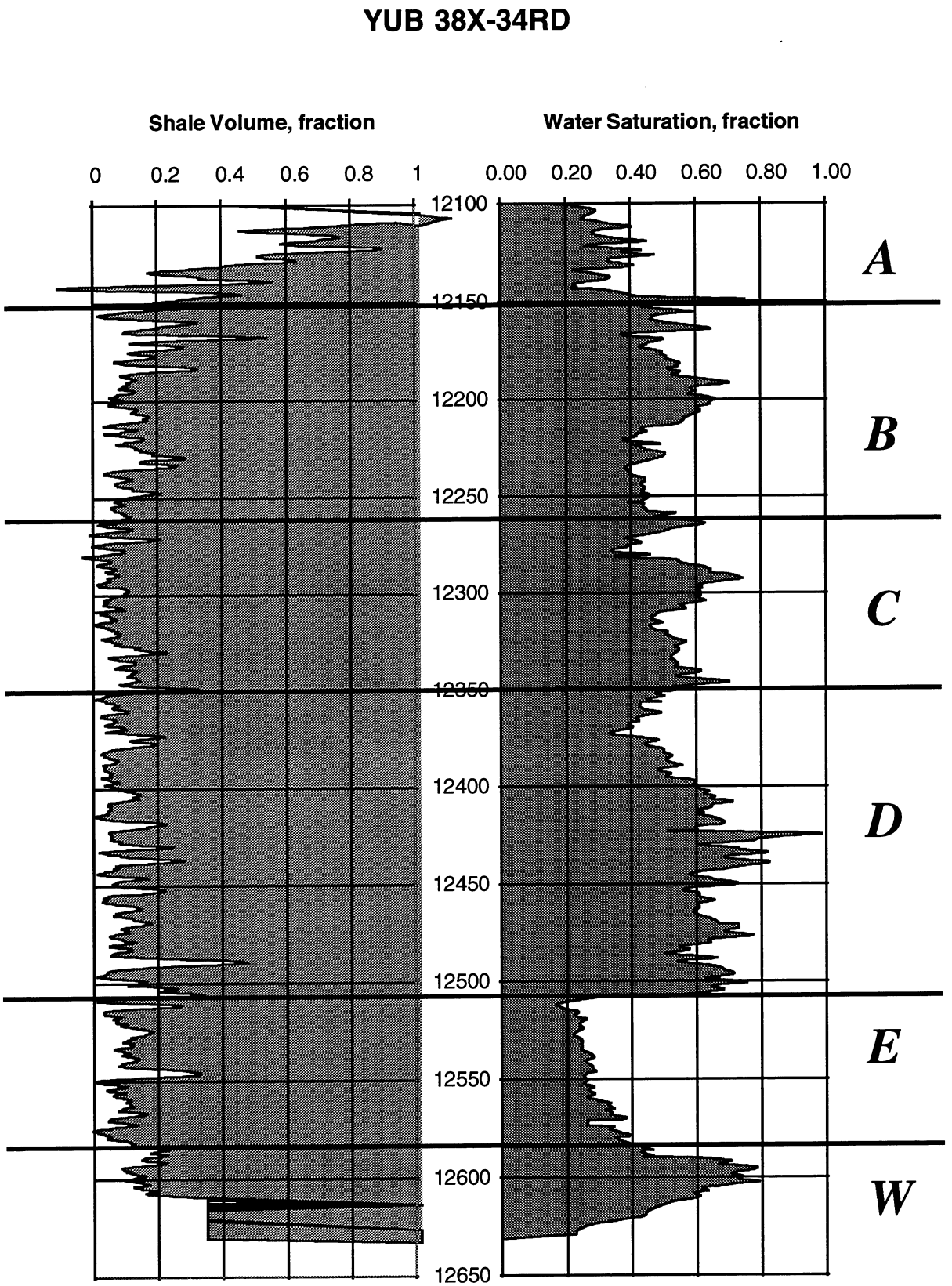

Figure 28: Type log of well 38X-34RD showing five main reservoir layers.

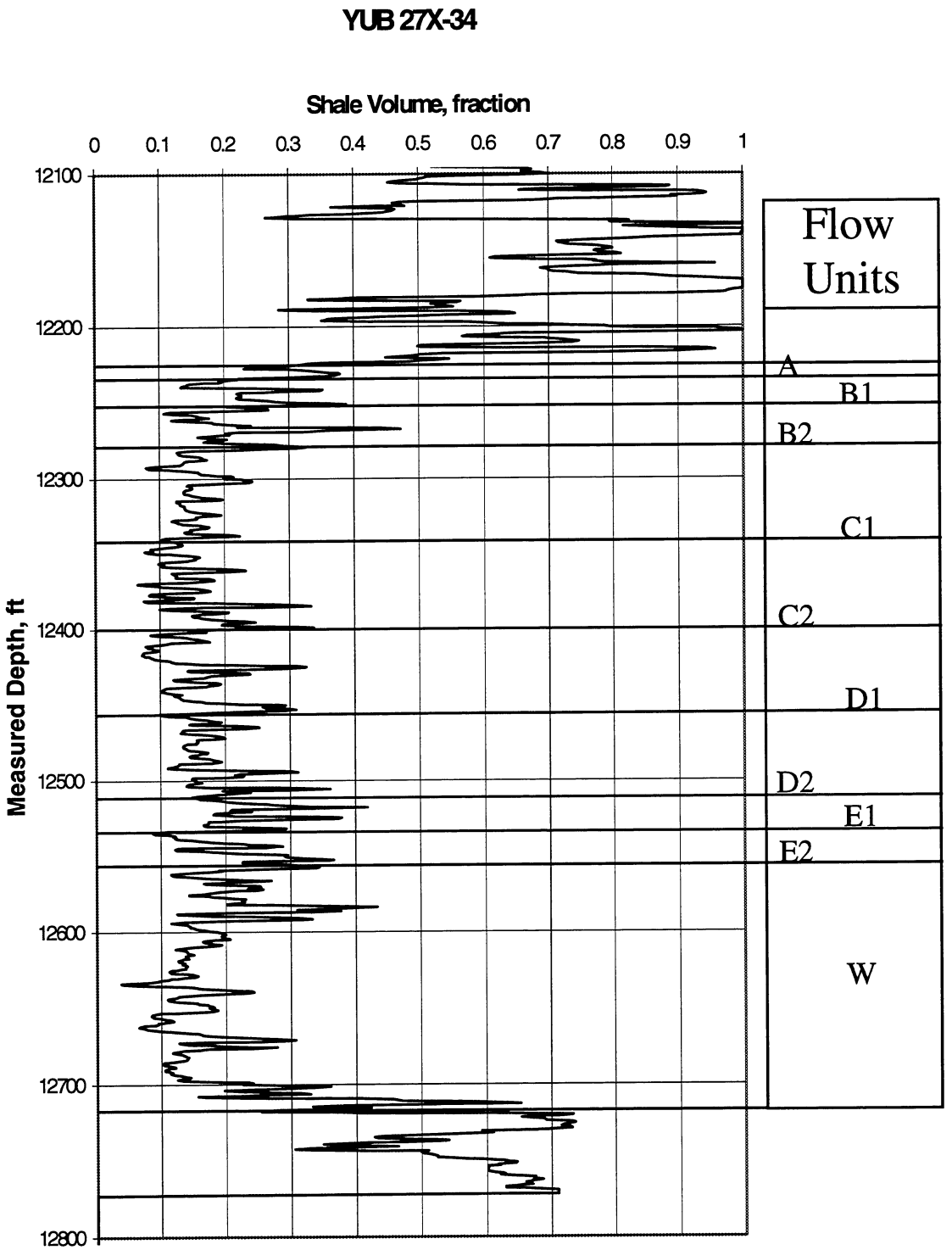

Figure 29: Type log of well 27X-34 showing subdivision of five main reservoir layers into ten layers.

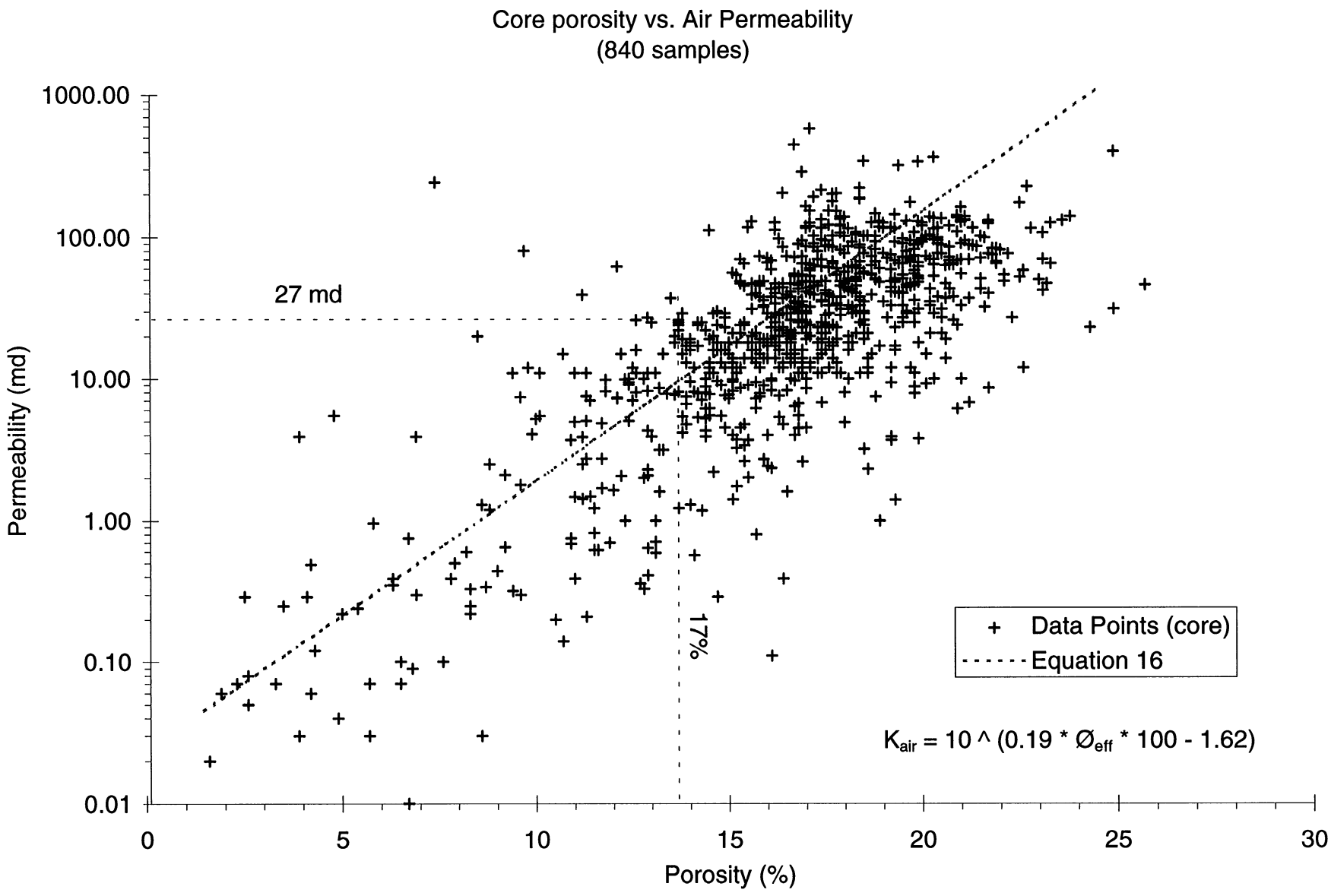

Figure 30: Crossplot of core permeability (air) to porosity.

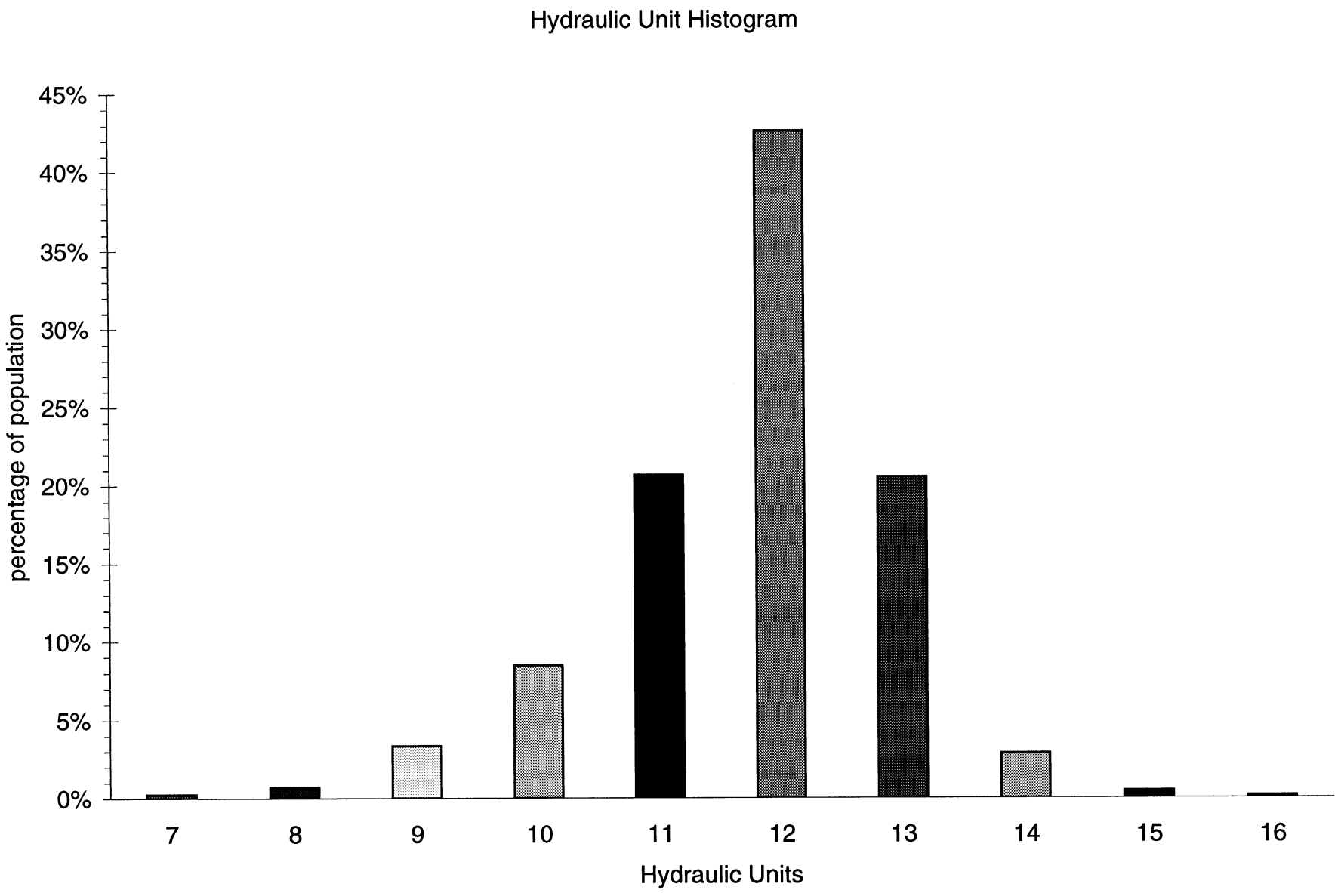

Figure 31: Histrogram showing frequency of hydraulic units in the Yowlumne sandstone.

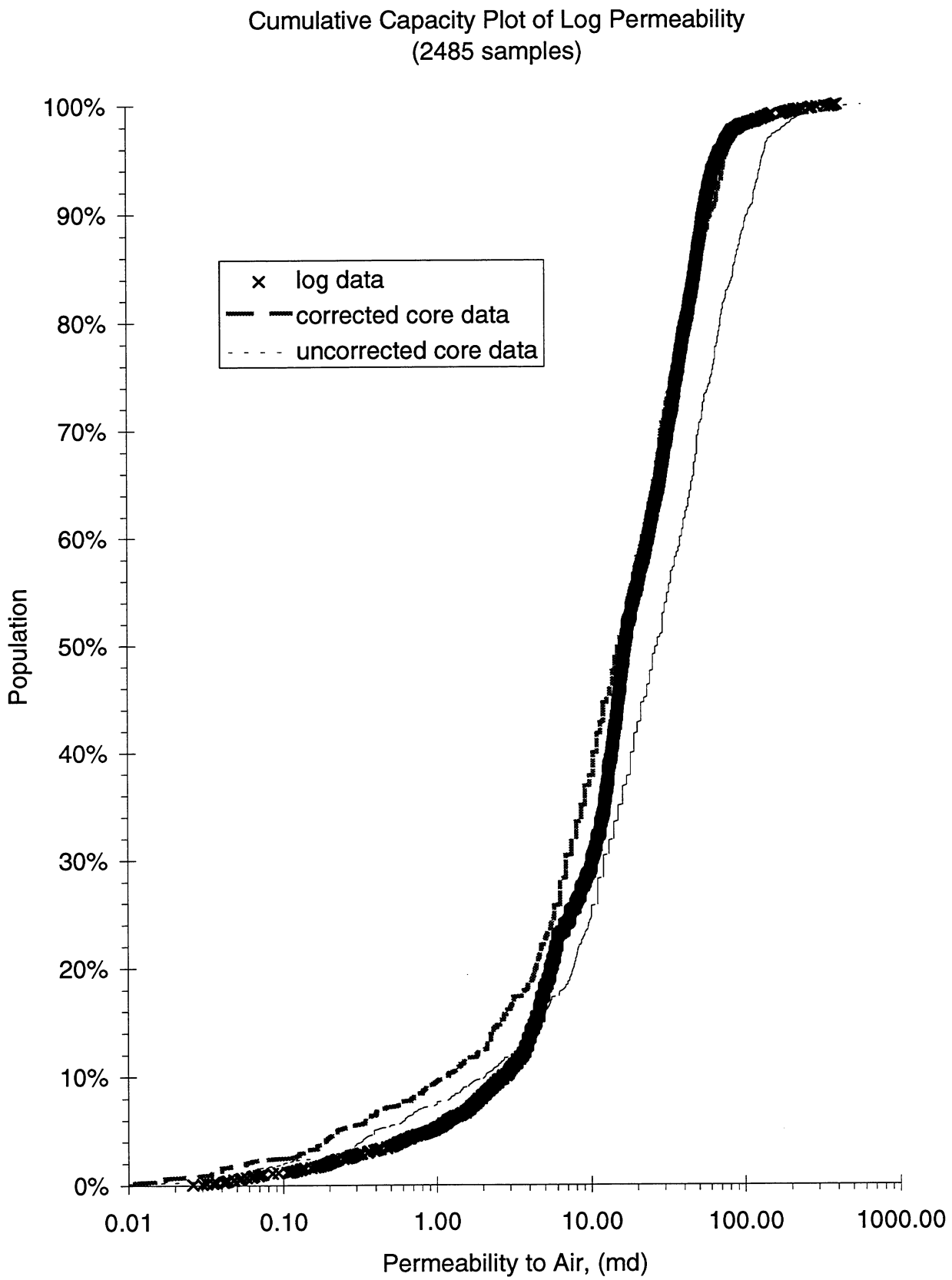

Figure 32: Cumulative capacity plot of air permeability.

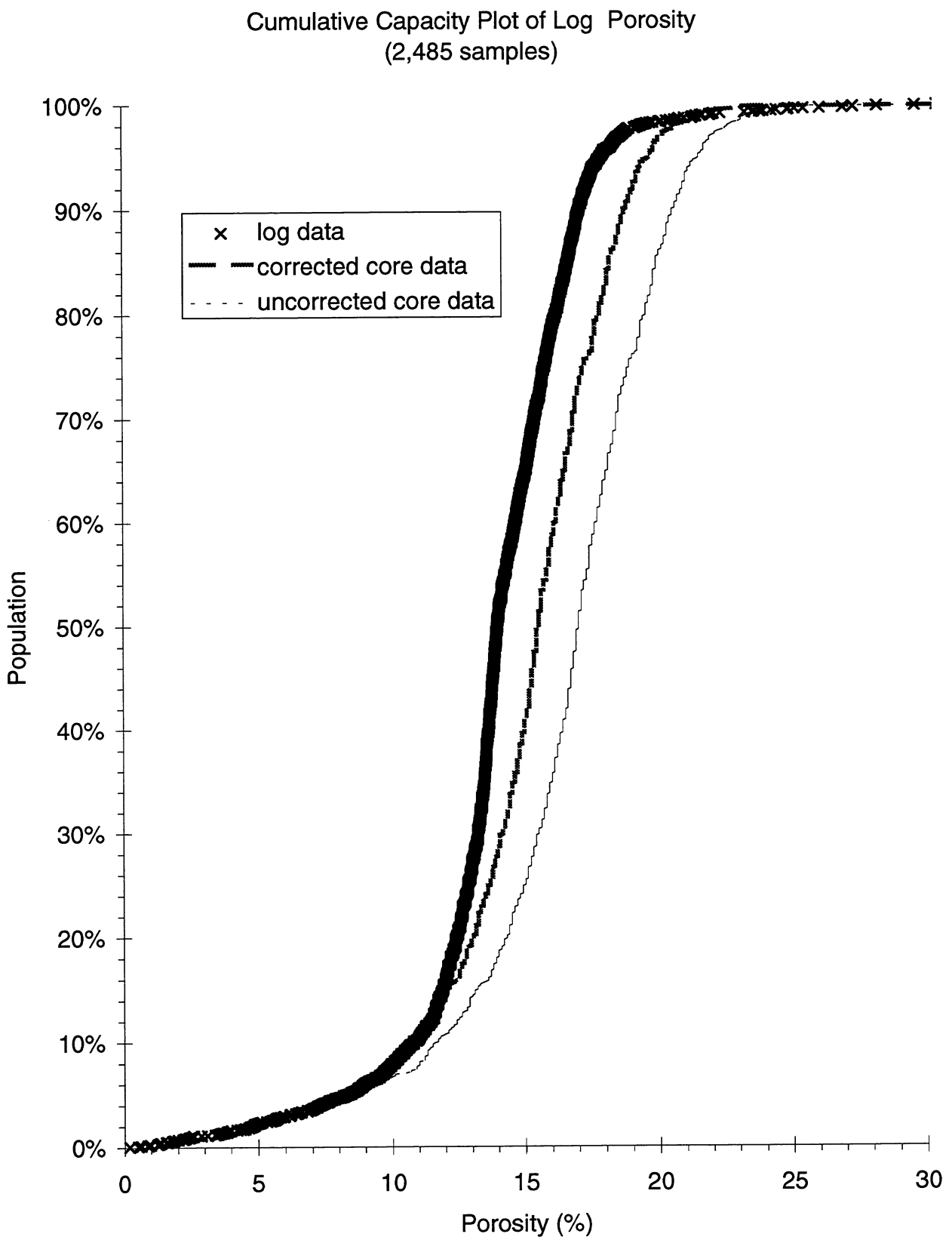

Figure 33: Cumulative Capacity Plot of Effective Porosity.

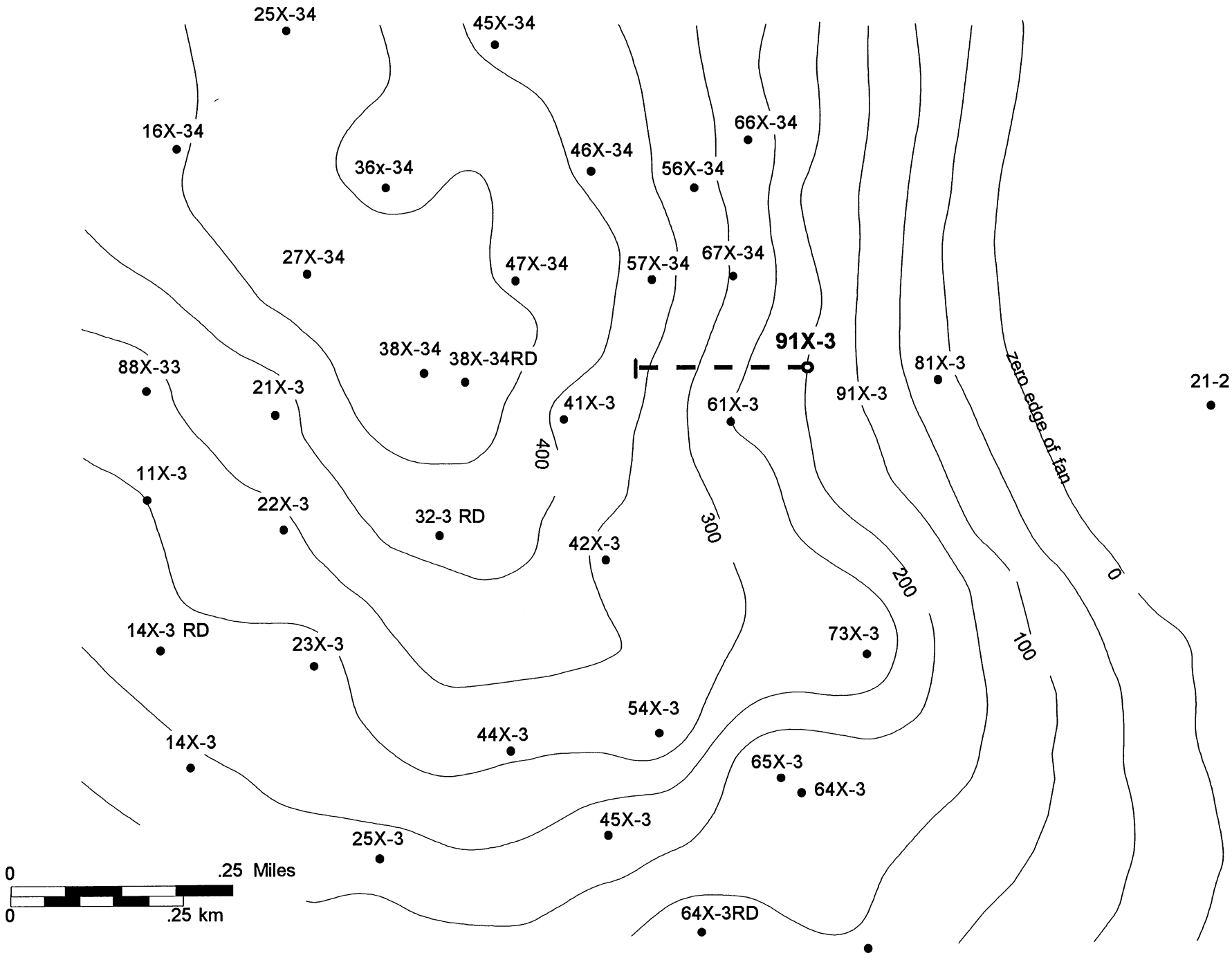

Figure 34: Map of gross sand thickness.

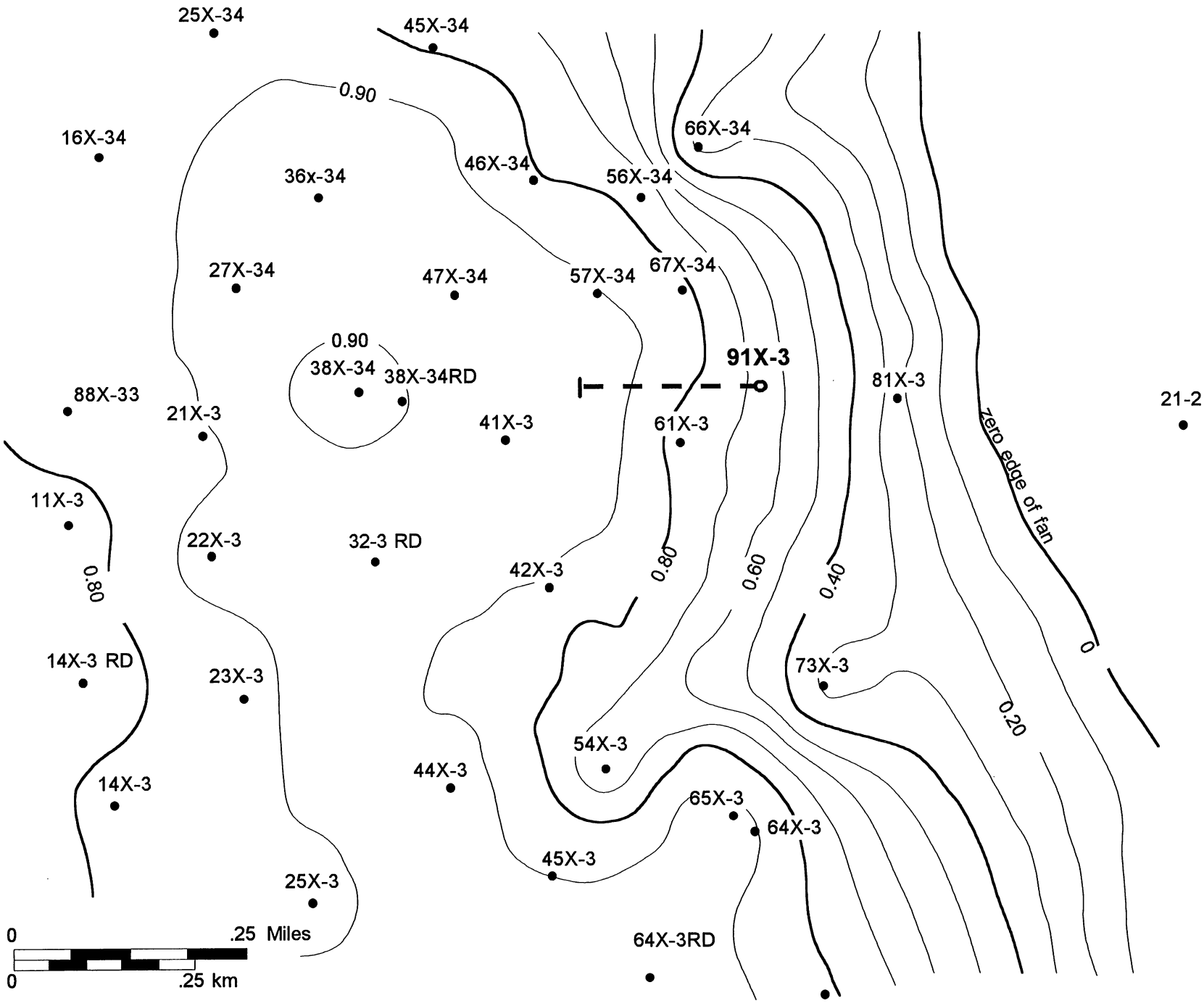

Figure 35: Map of net-to-gross sand ratio.

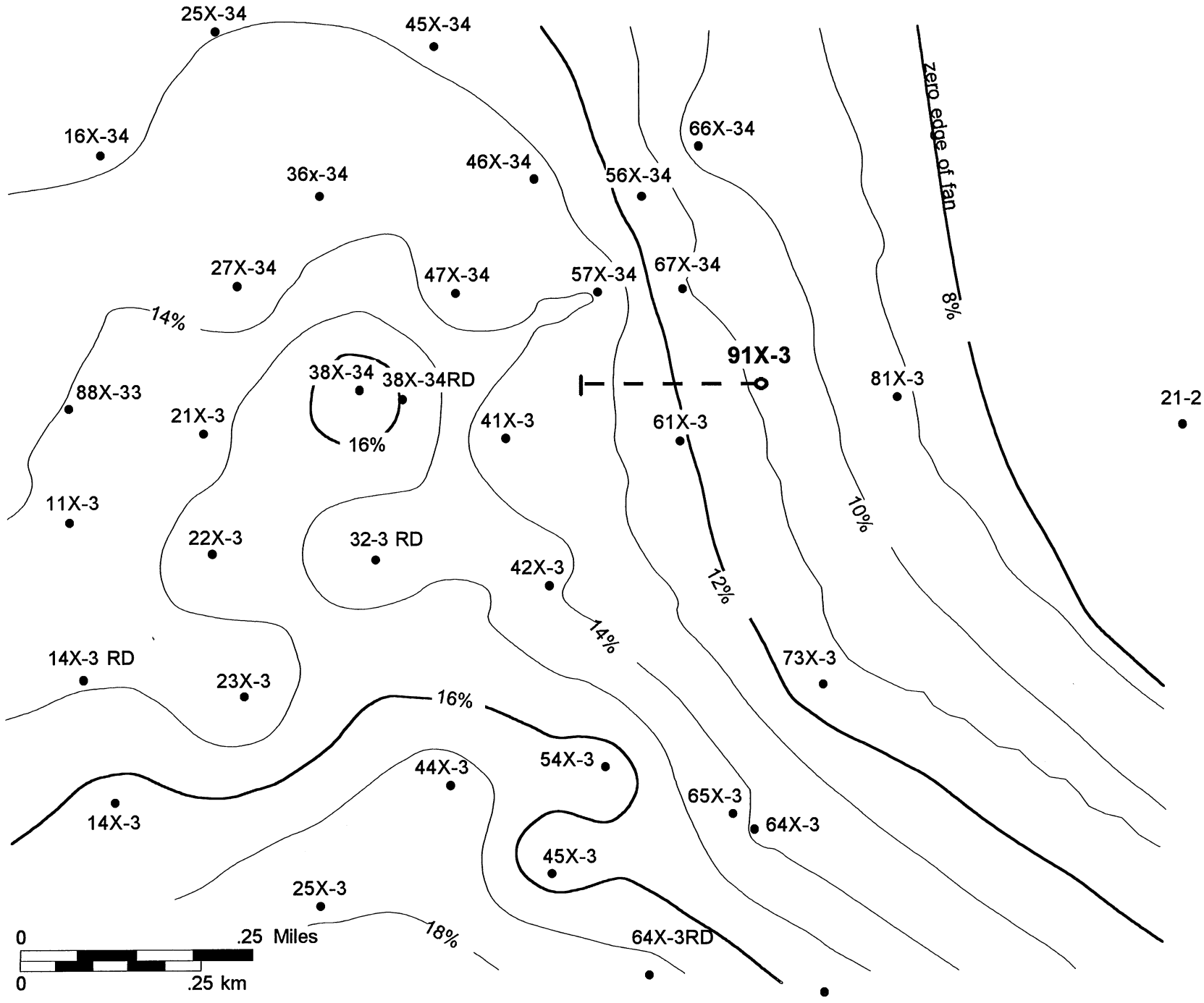

Figure 36: Map of effective porosity of net sand.

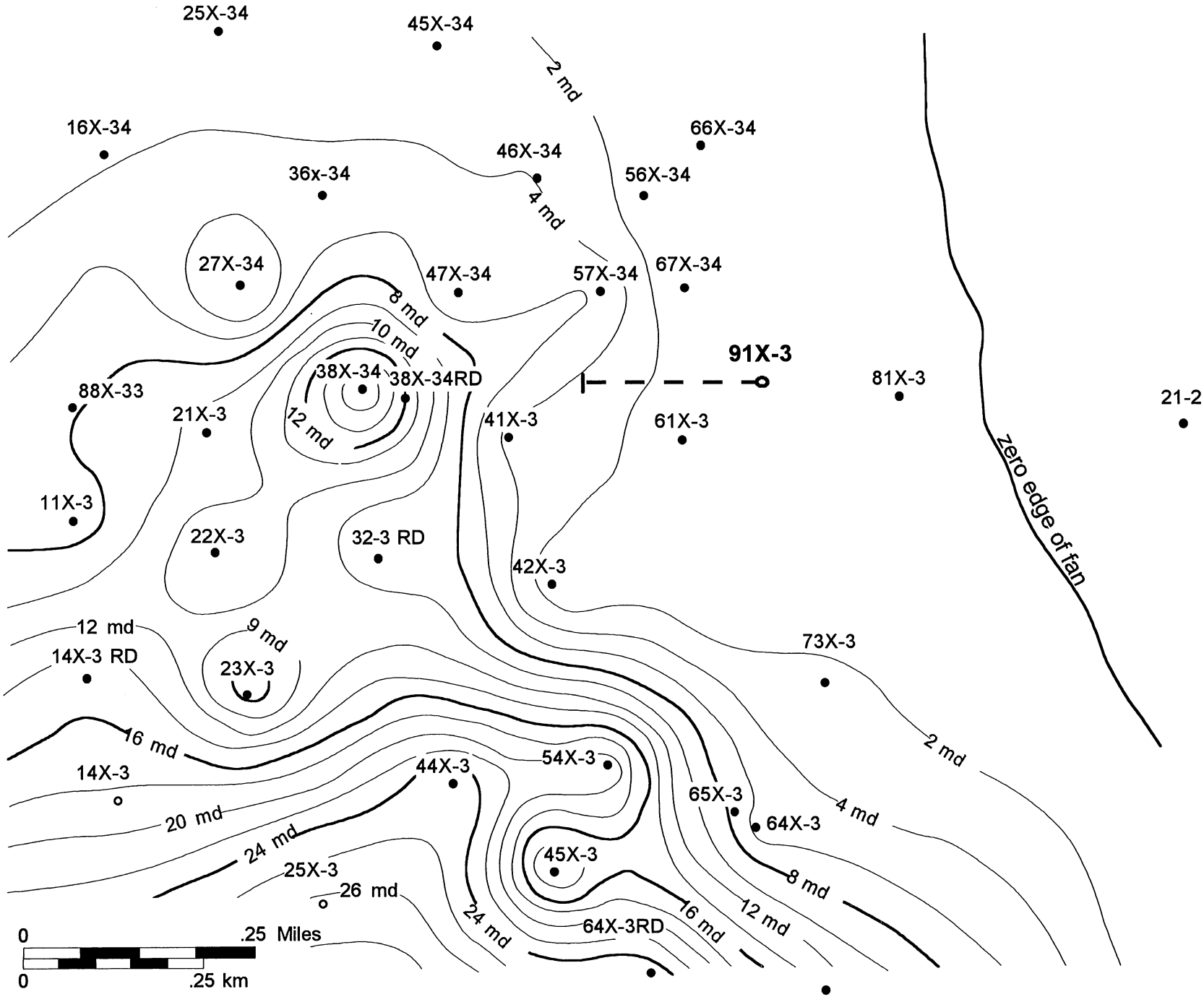

Figure 37: Map of liquid permeability of net sand.

Yowlumne Unit B Streamline Analysis

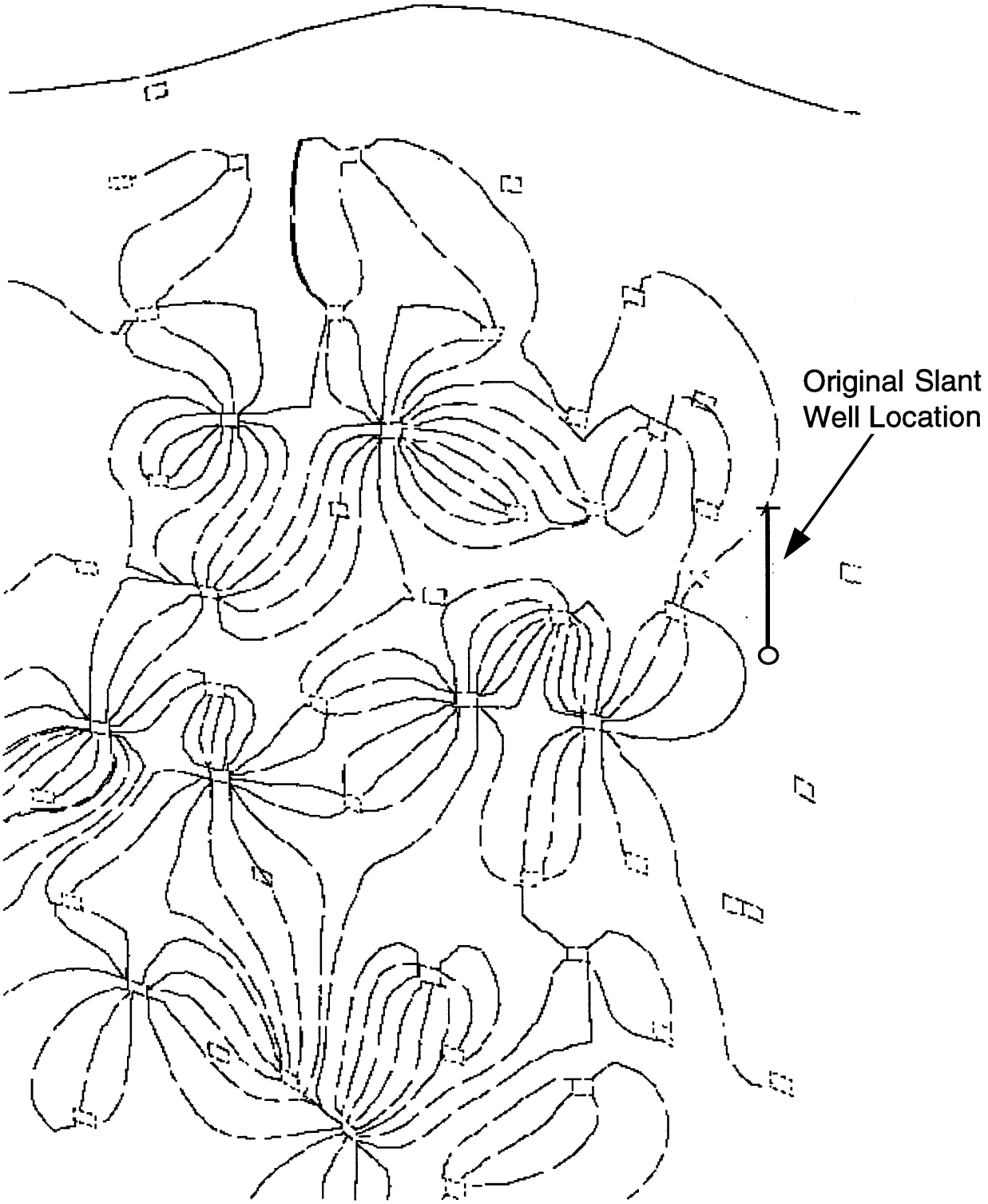

Figure 38: Streamline map showing original North-South slant well

Yowlumne Partial-Field Fine-Grid Model

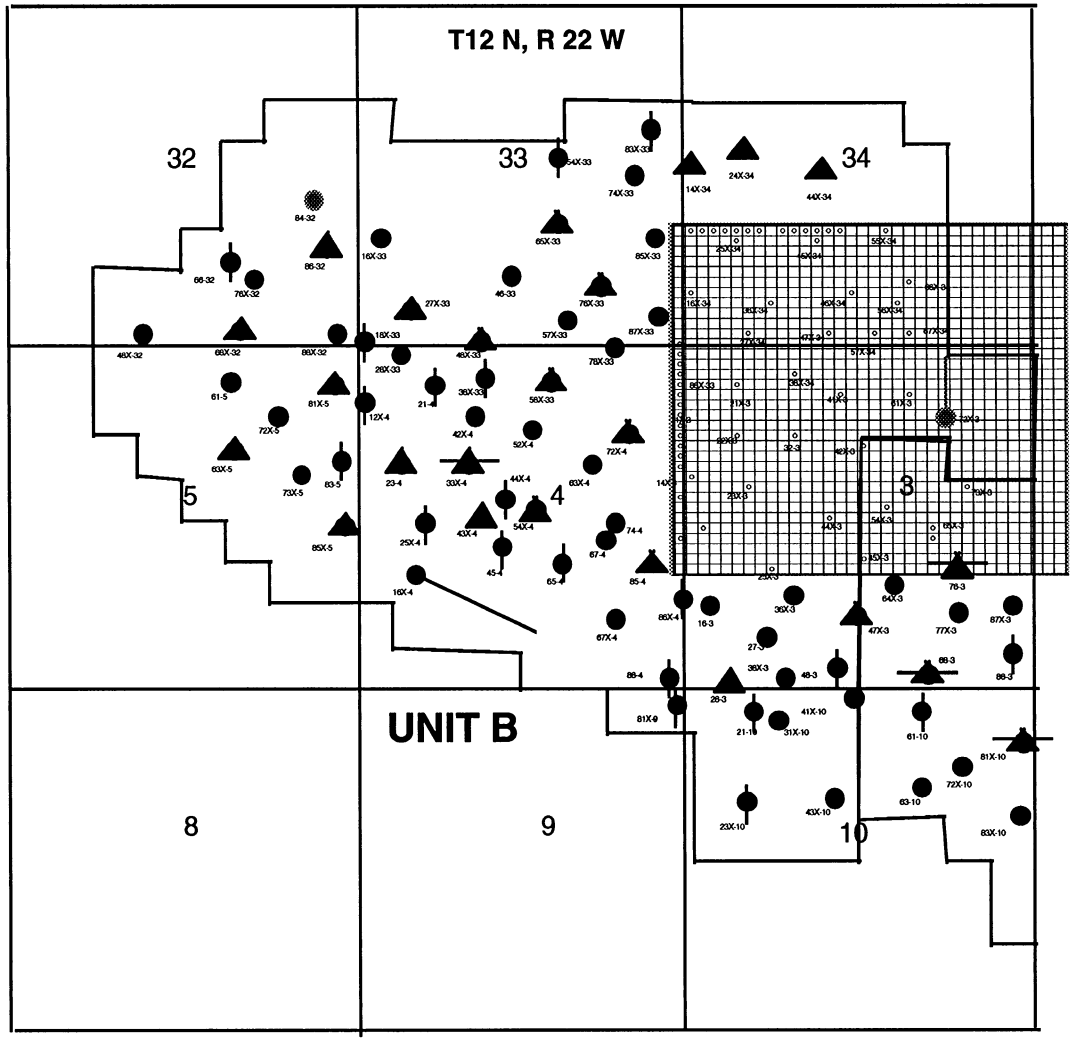

Figure 39: Areal location of partial field model grid.

Fine-Grid Model with Local Grid Refinement

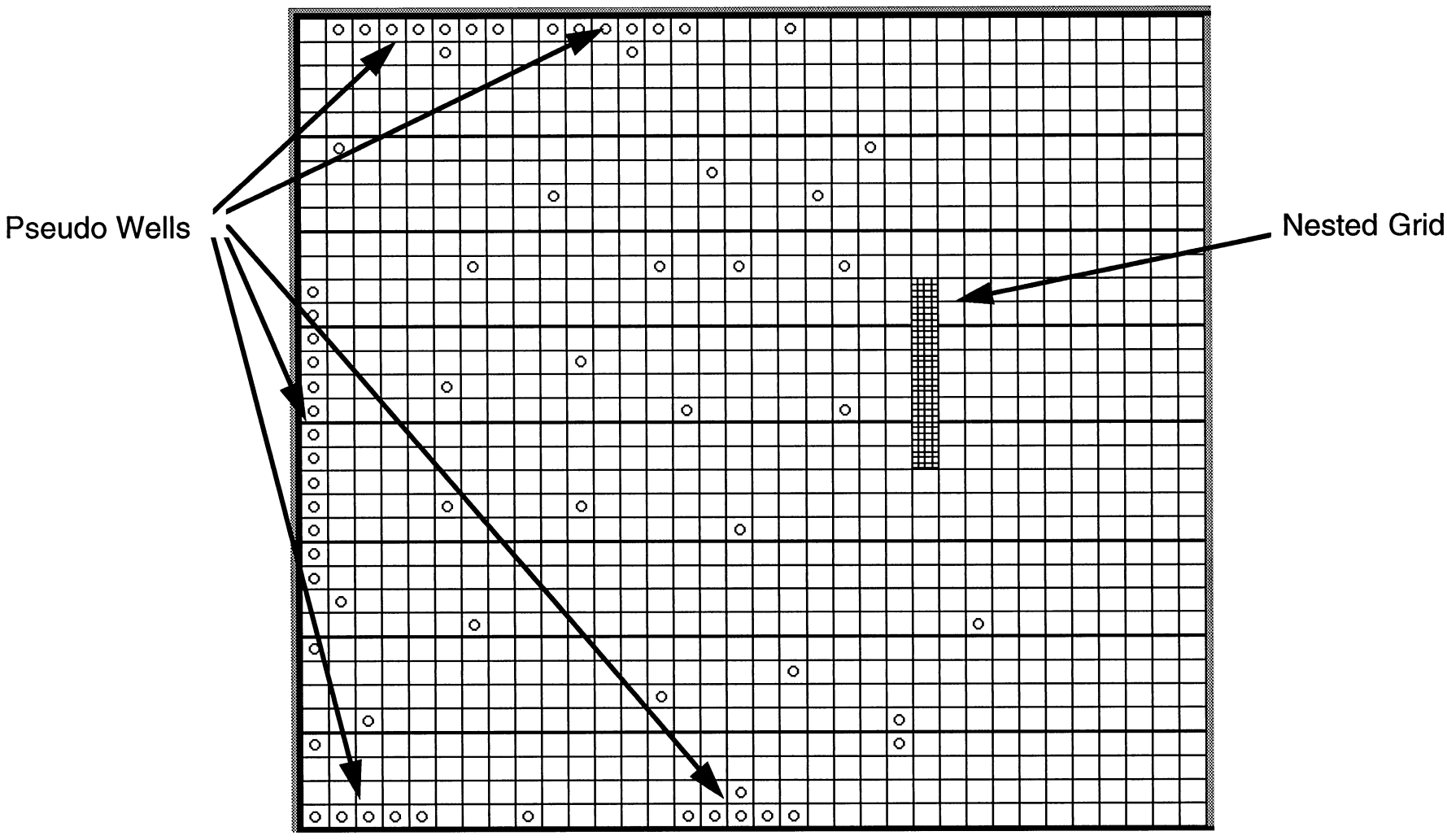

Figure 40: Partial field model grid with local grid refinement.

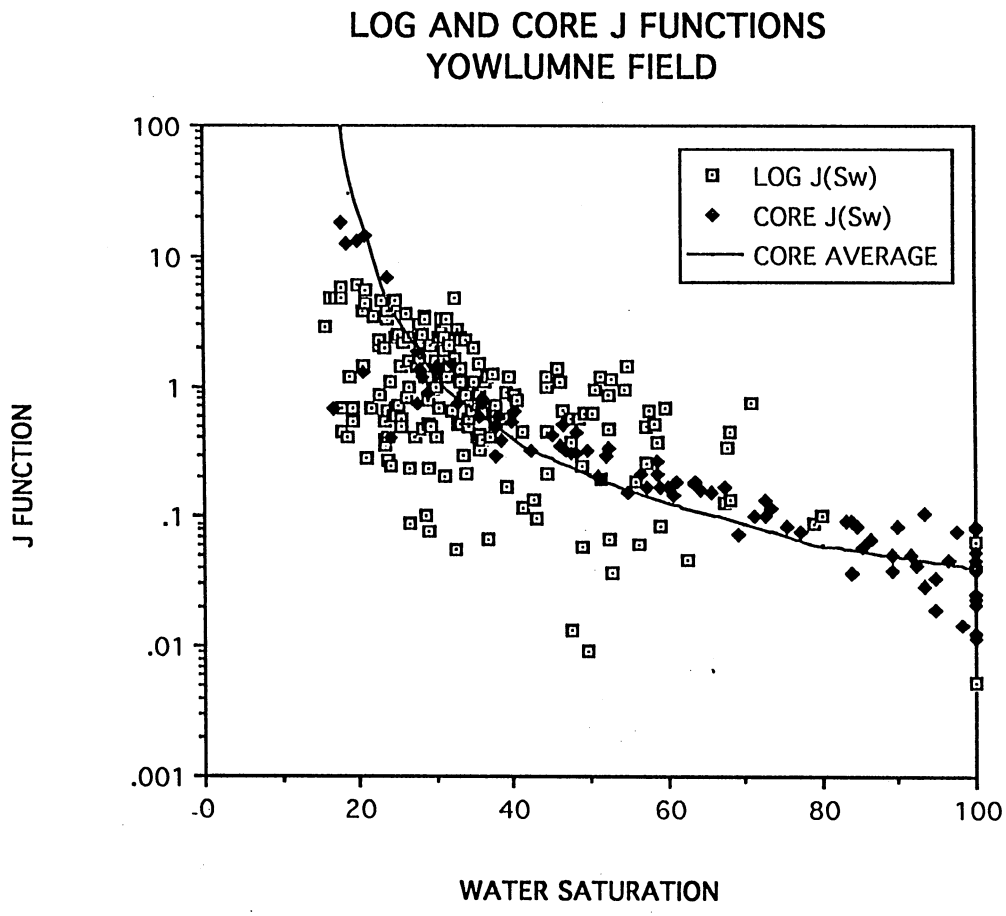

Figure 41: Log and core J-Functions.

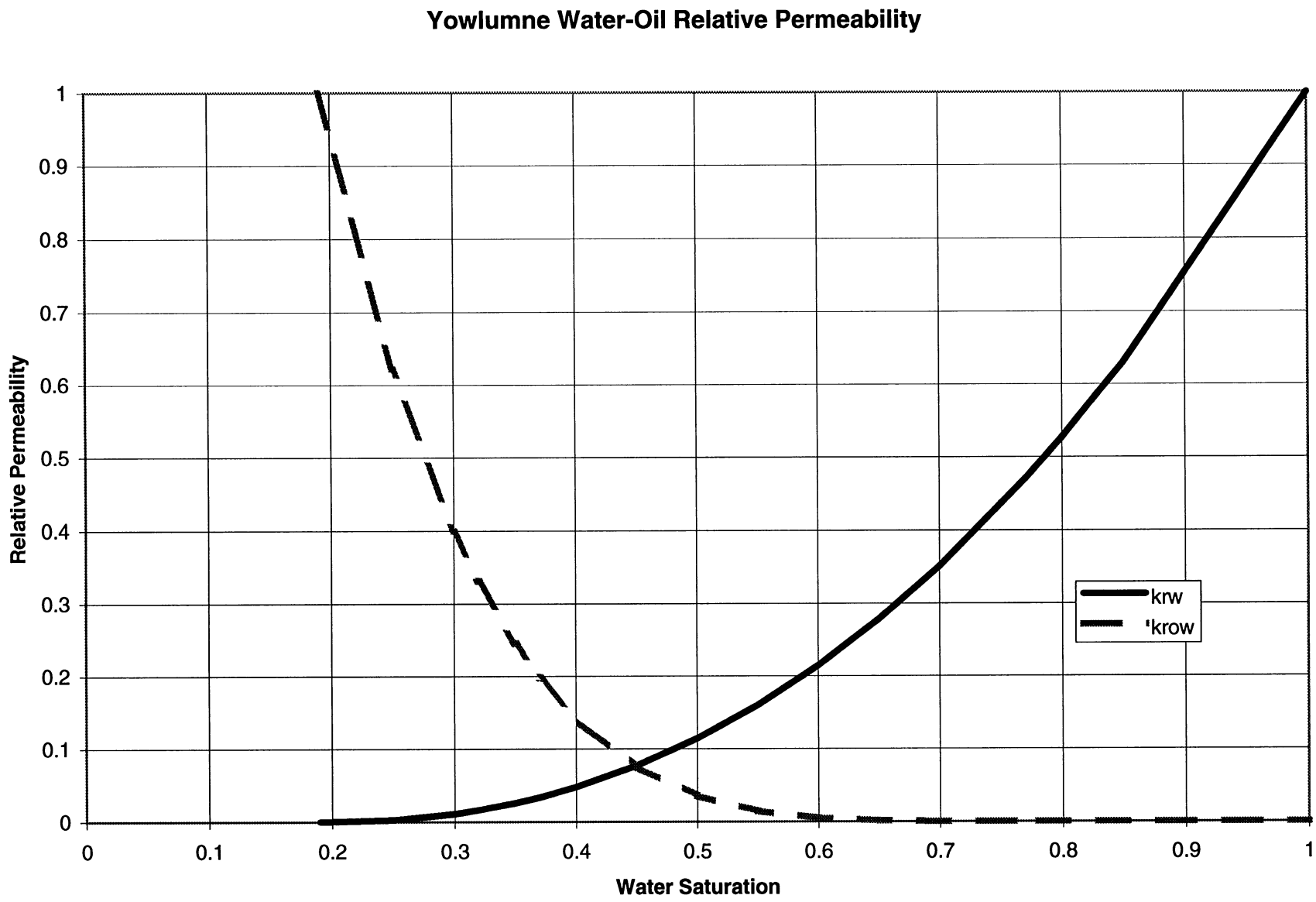

Figure 42: Water-oil relative permeability.

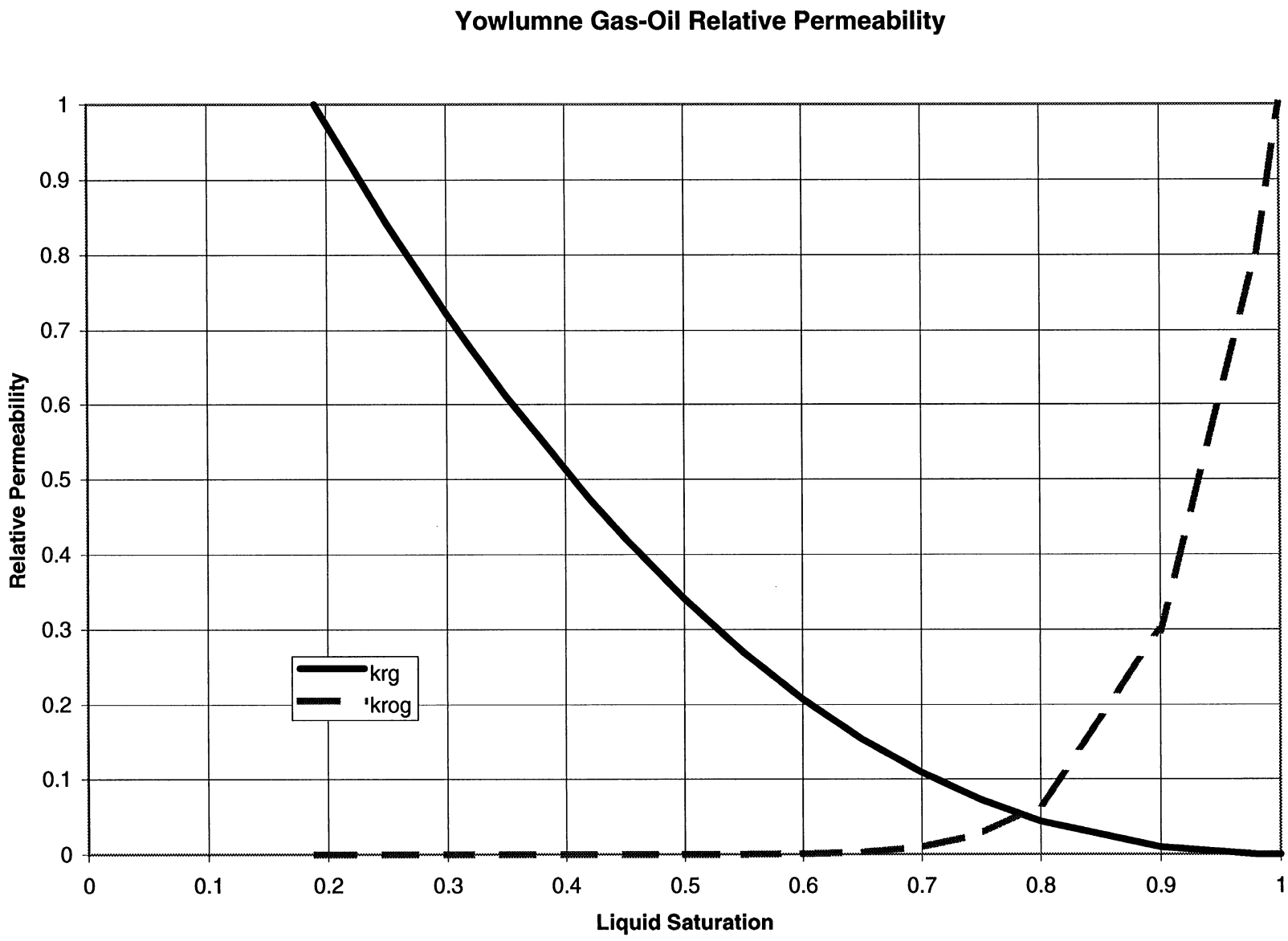

Figure 43: Gas-oil relative permeability.

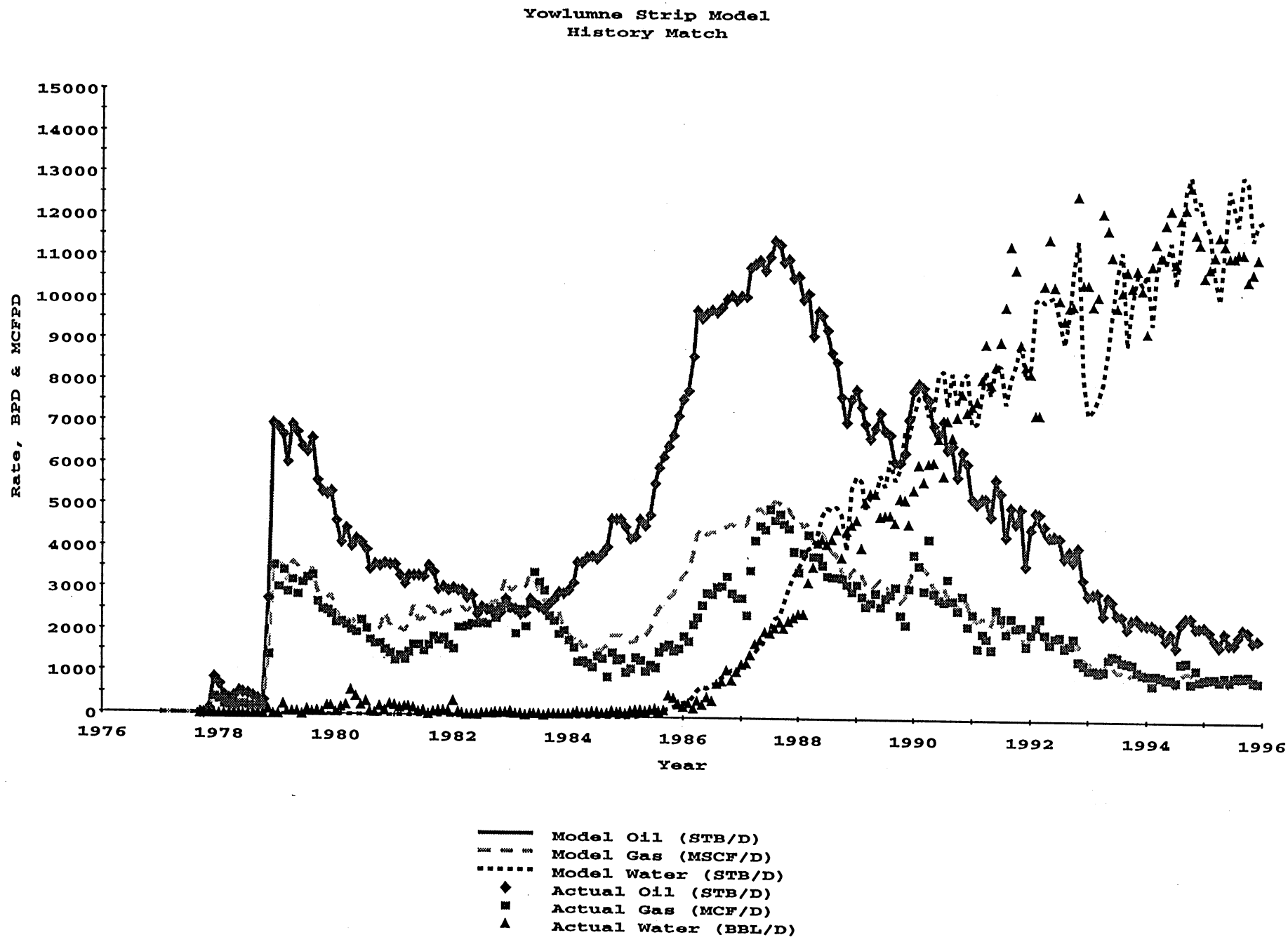

Figure 44: History match of model area production rates.

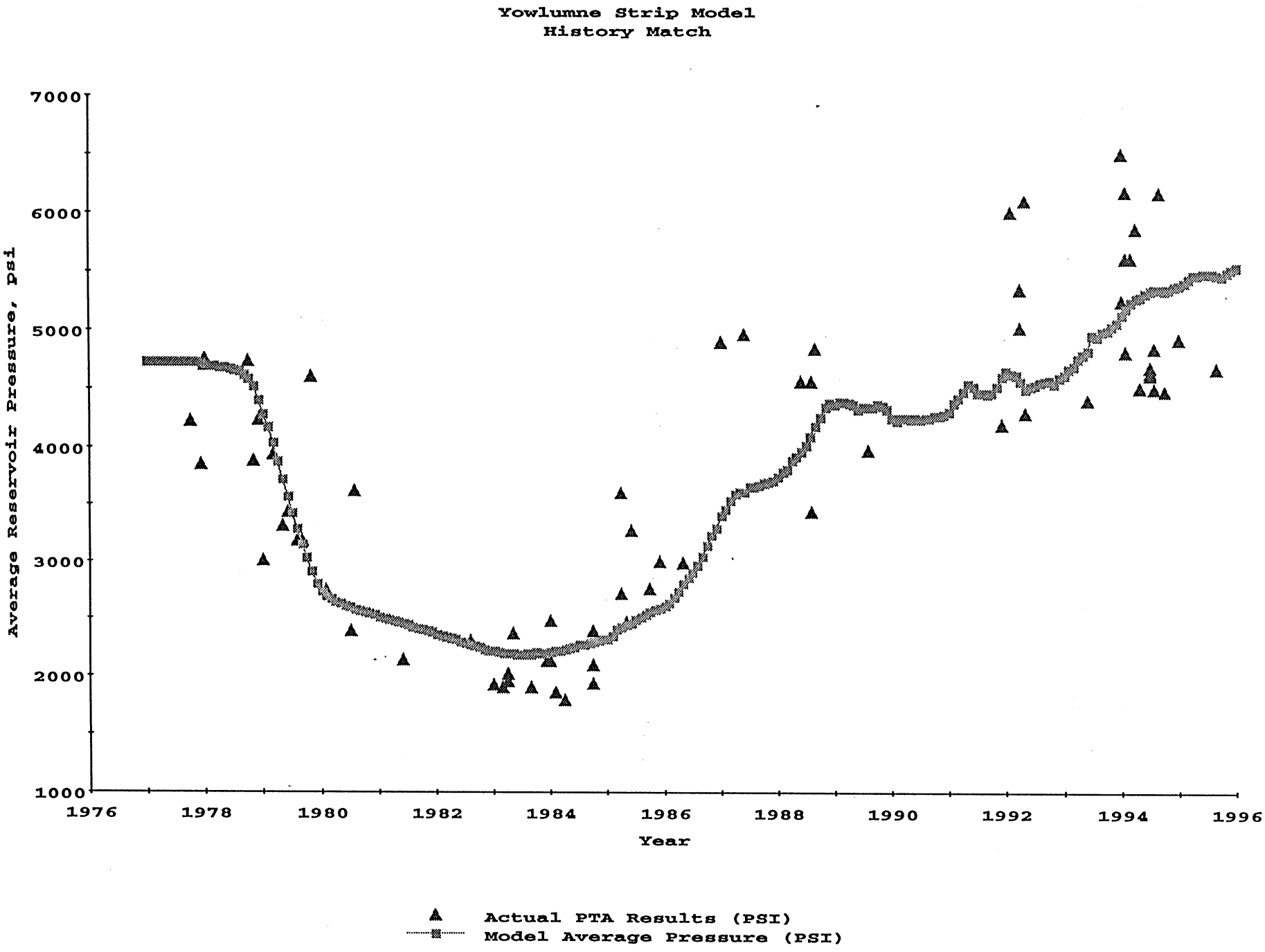

Figure 45: History match of model area pressure.

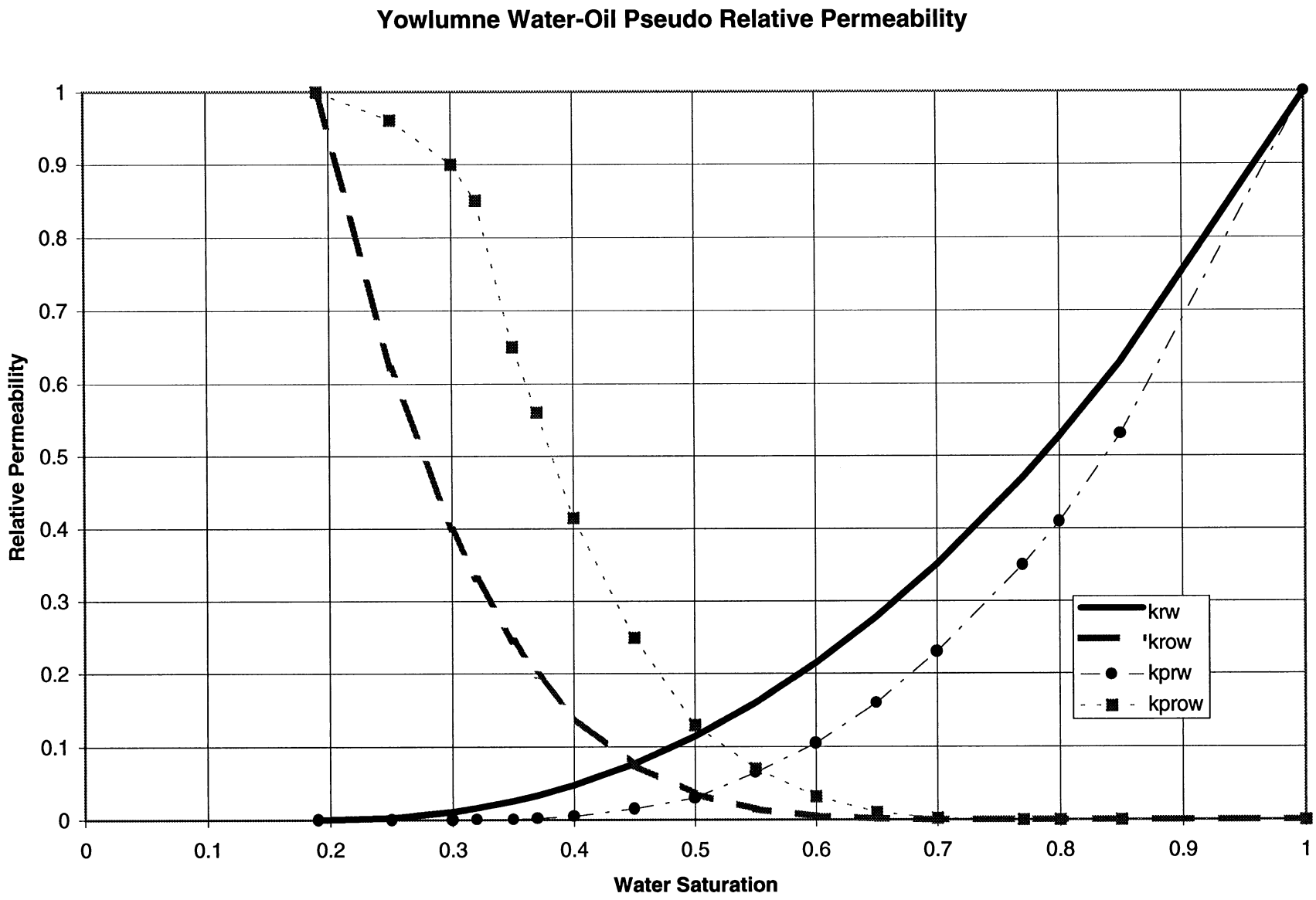

Figure 46: Water-oil pseudo relative permeability.

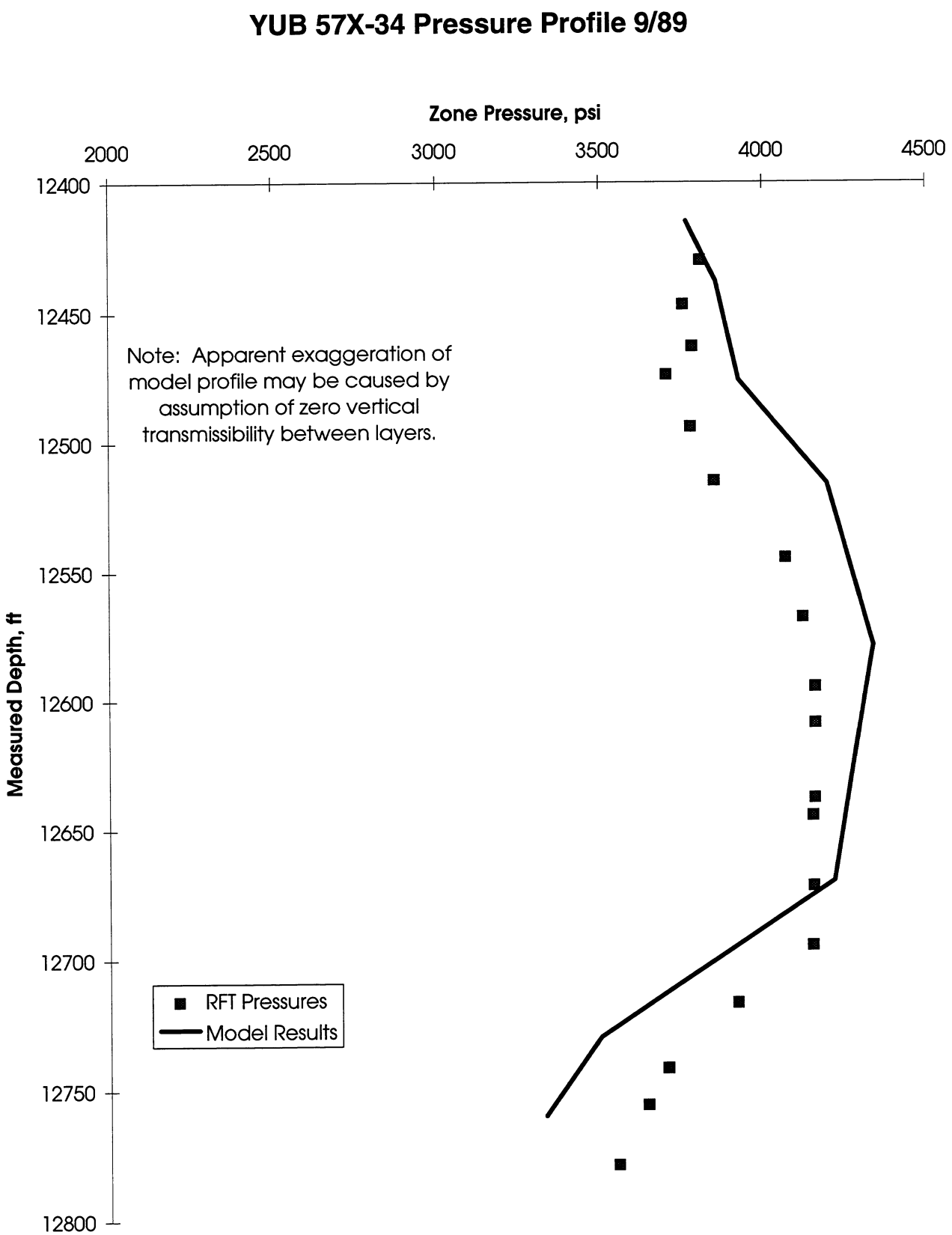

Figure 47: History match of well 57X-34 pressure profile.

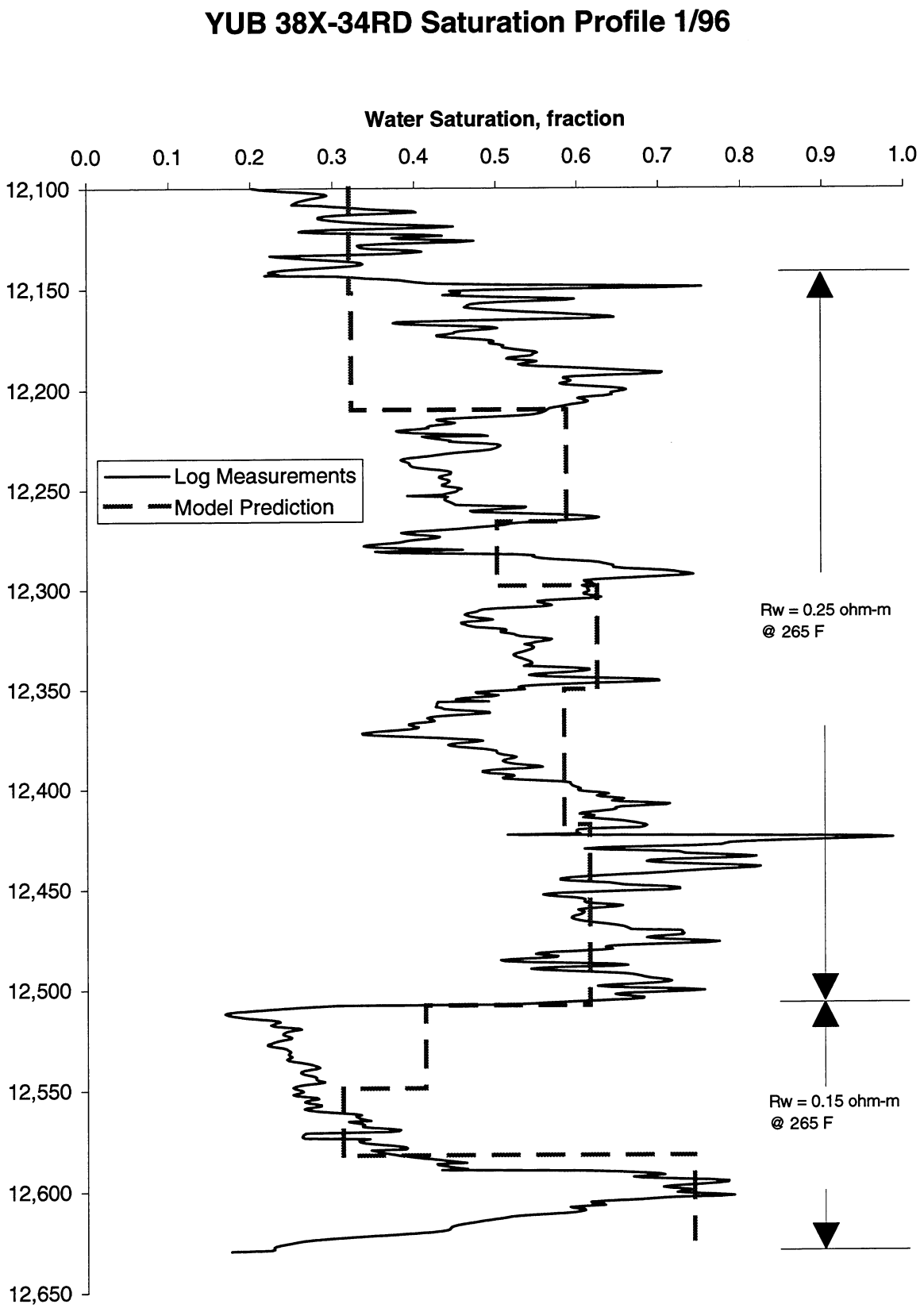

Figure 48: History match of well 38X-34RD water saturation profile.

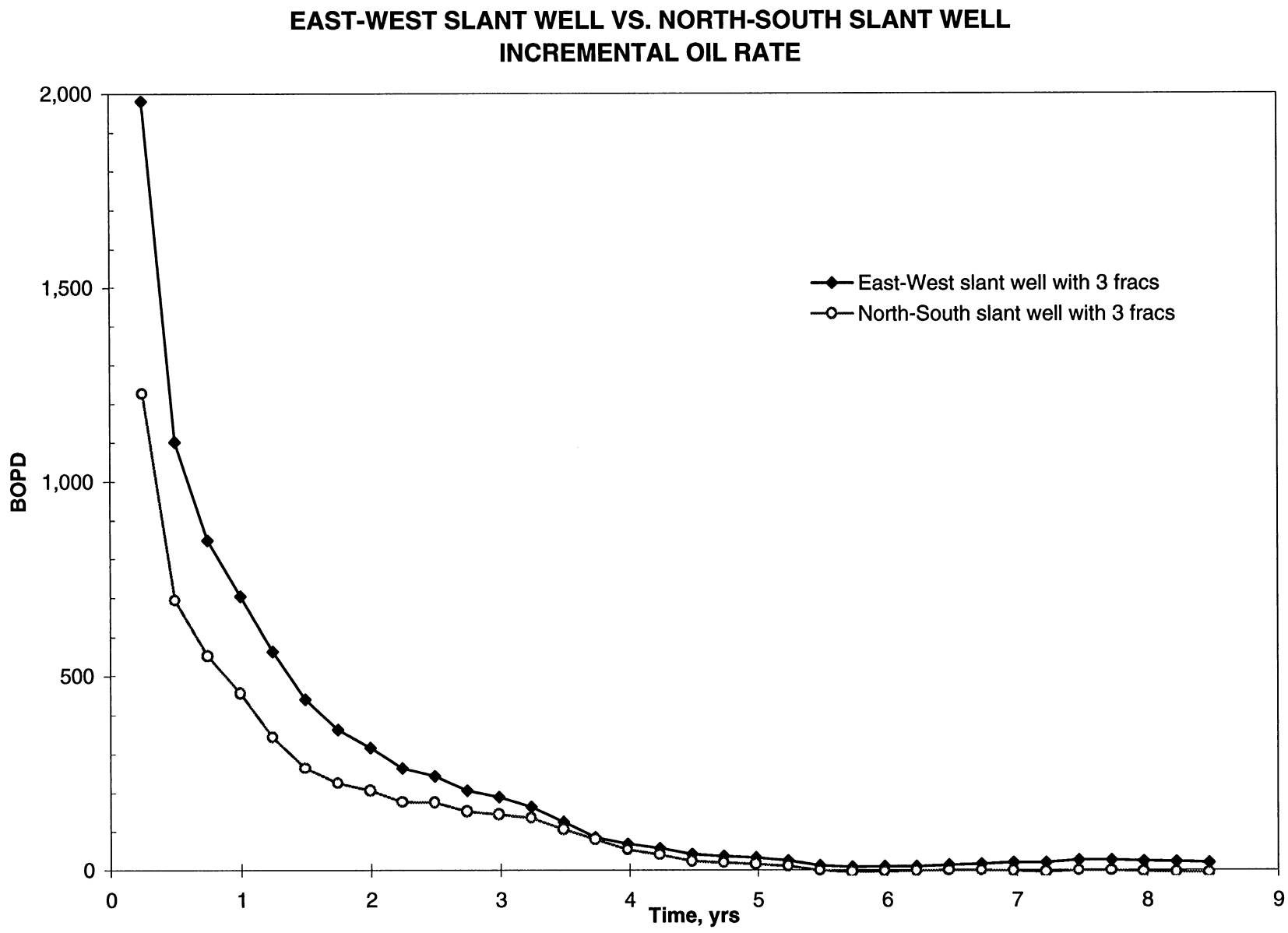

Figure 49: Comparison of incremental production rates for East-West slant well and North-South slant well.

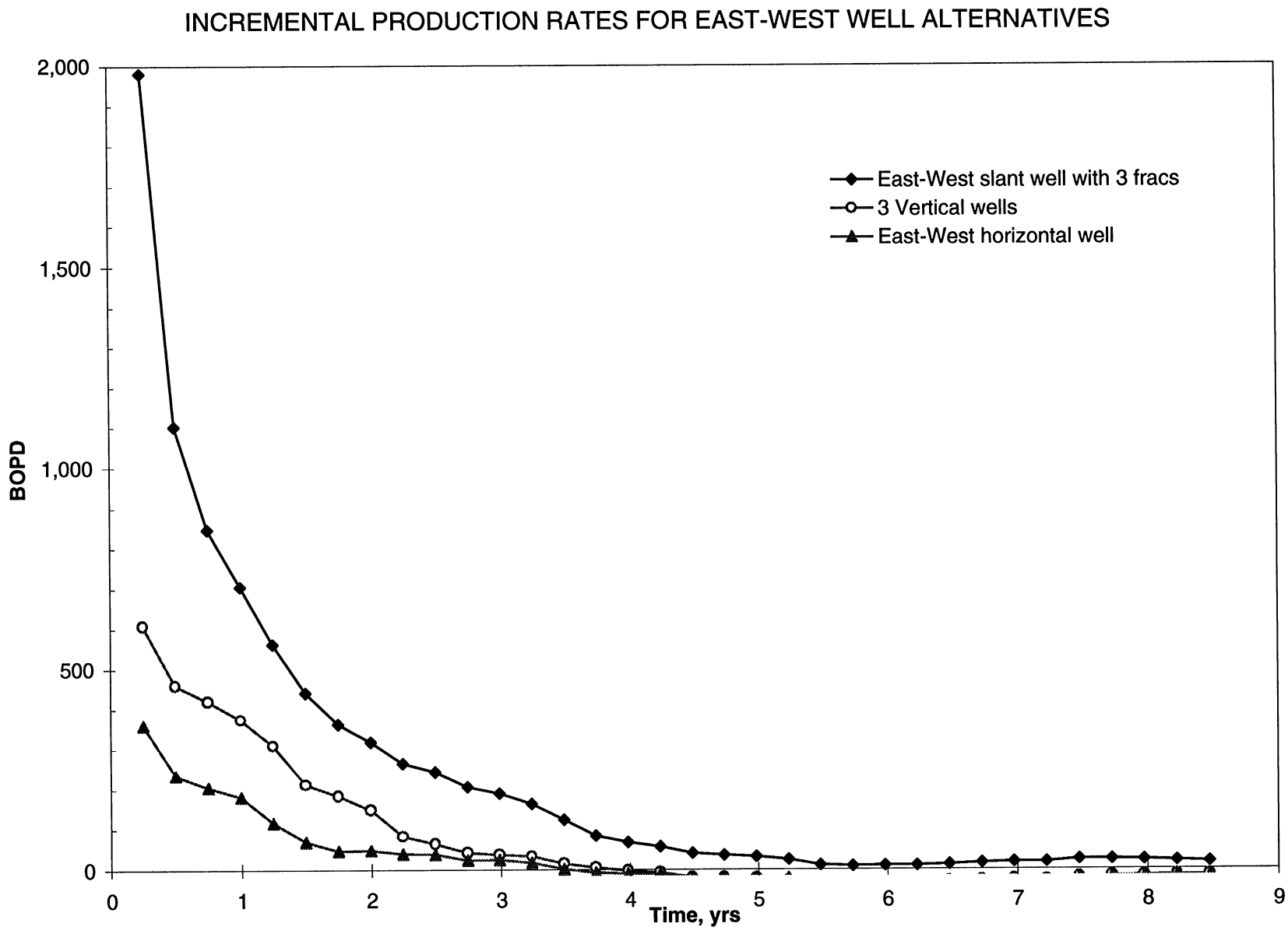

Figure 50: Comparison of incremental production rates for 3 vertical wells, East-West horizontal well, and East-West slant well.

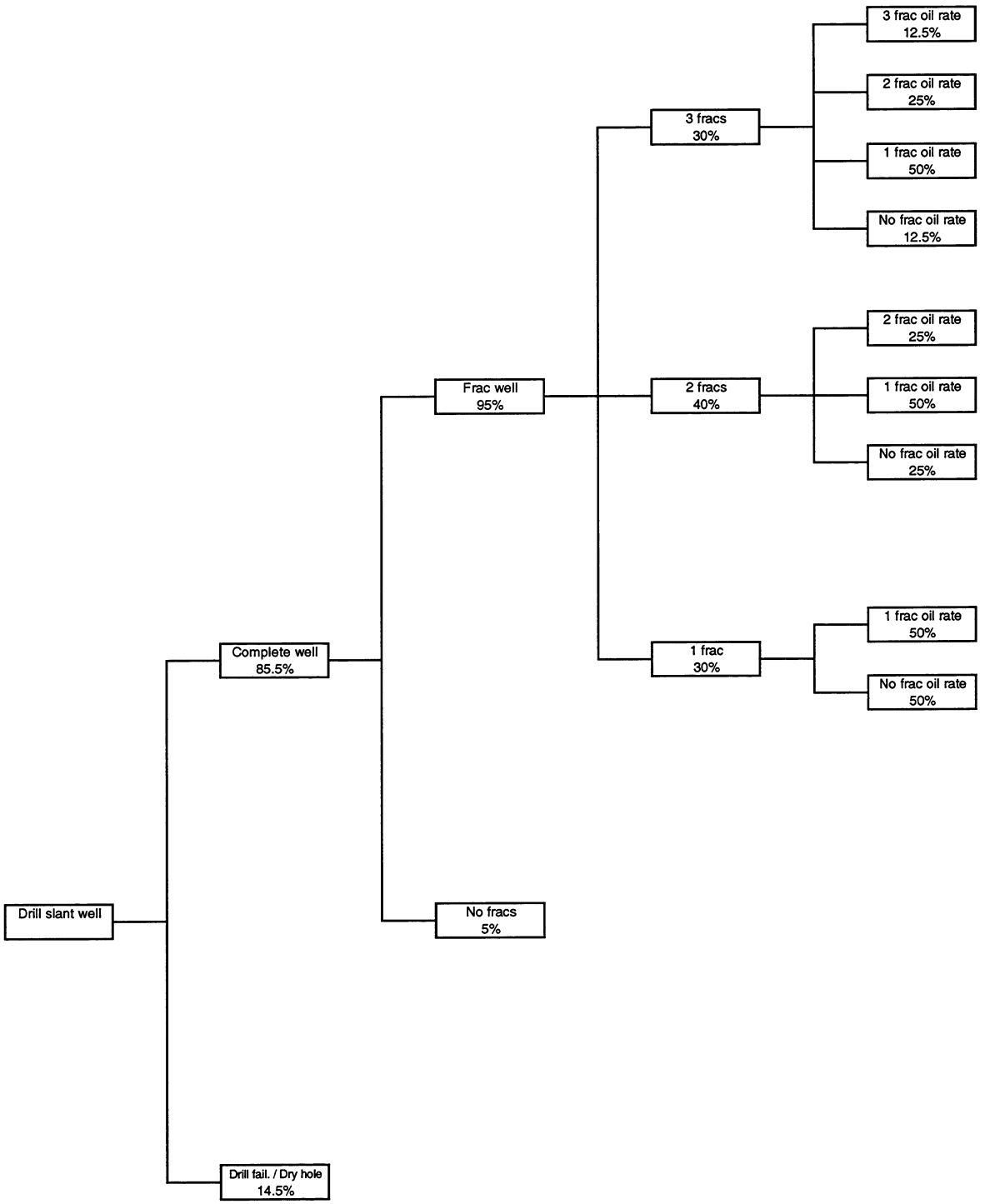

Figure 51: Decision tree used with economic analysis.

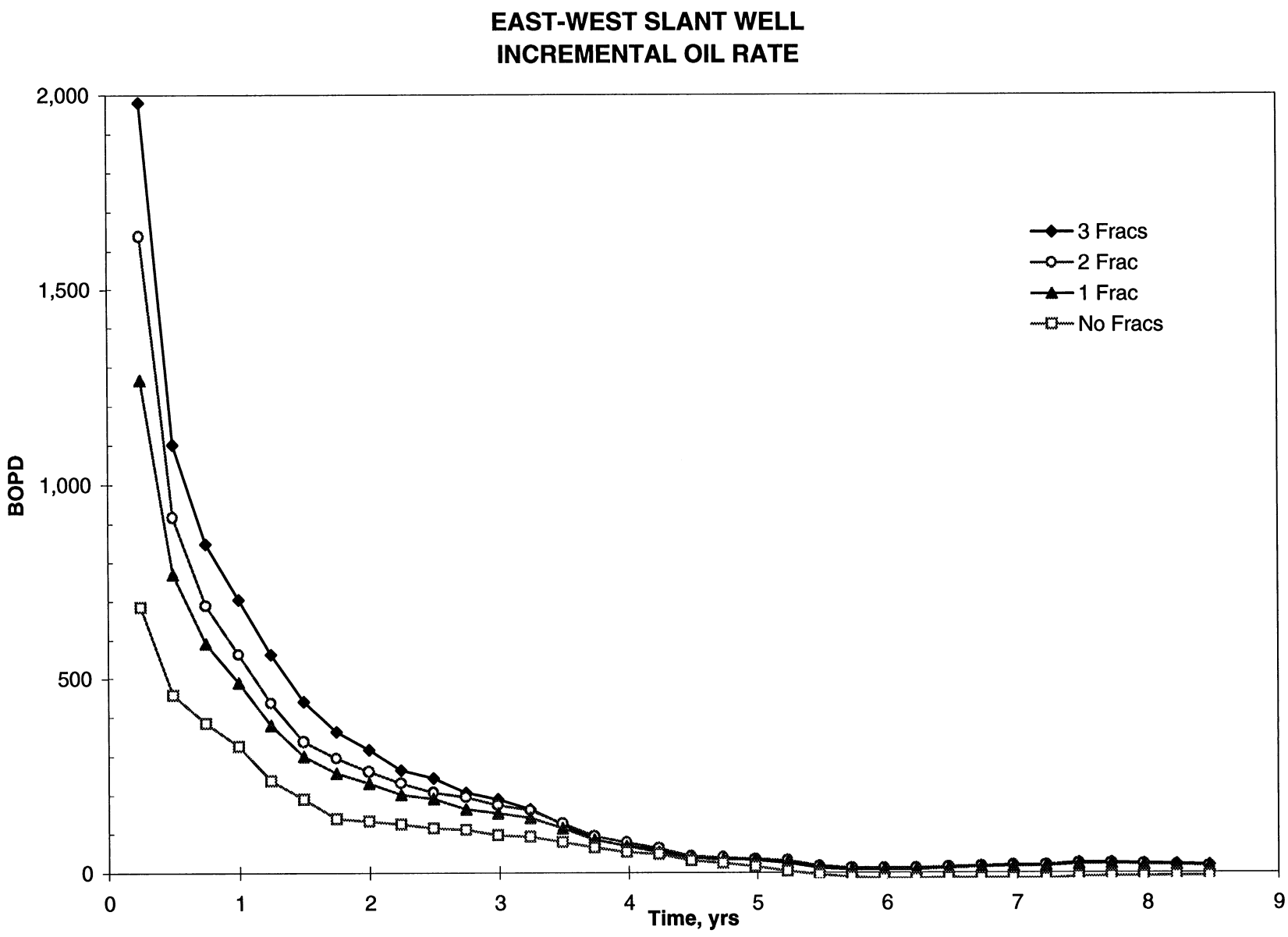

Figure 52: Sensitivity of incremental production rates to the number of fracs for East-West slant well.

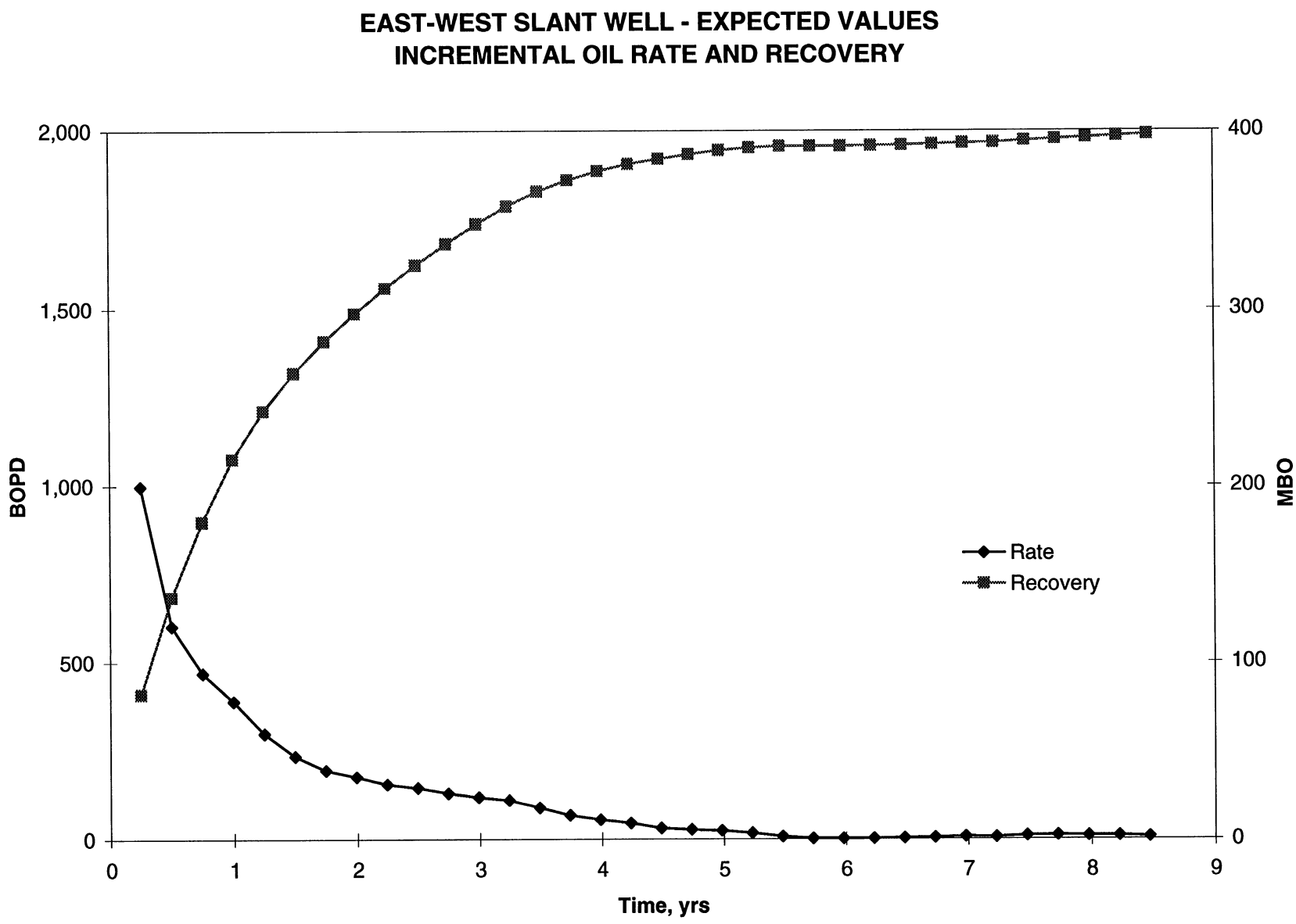

Figure 53: Incremental production rate and recovery for East-West slant well (expected values).

Table 1

Rock Properties Used for Frac Design of Test Well

Zone	Gross Thickness, ft	Net Thickness, ft	Net Pay Thickness, ft	Vsh, fraction	ϕ, %	k, md
Upper Shale	58	0	0	0.69	N/A	N/A
Sand A	84	9	9	0.26	12.30	0.76
Sand B	44	27	26.5	0.14	15.21	8.27
Sand C	23	4	4	0.10	12.87	1.19
Sand D	30	15	15	0.12	12.36	0.62
Sand E	35	22	17	0.07	13.41	1.45
W Sand	13	0	0	0.41	N/A	N/A
Lower Shale	18	0	0	0.53	N/A	N/A

1. Net thickness cutoff: $V_{sh}<0.30$, $\phi>0.11$, k >0.1 md
2. Net pay cutoff: $V_{sh}<0.30$, $\phi>0.11$, k >0.1 md, S_w <0.40
3. ϕ and k consider pay only

Table 2

Mechanical Properties Used for Frac Design of Test Well

Zone	Gross Thickness, ft	** Pressure, psi	** Fracture Gradient, psi/ft	*** Pressure, psi	*** Fracture Gradient, psi/ft
Upper Shale	58	5979	1.142	5979	1.142
Sand A	84	4500	0.956	5060	0.985
Sand B	44	4500	0.947	5060	0.977
Sand C	23	4500	0.946	4500	0.946
Sand D	30	4500	0.943	3560	0.893
Sand E	35	4500	0.939	3560	0.889
W Sand	13	6089	0.980	6089	0.980
Lower Shale	18	5906	0.981	6096	0.981

** assumes uniform pore pressure distribution across sands A-E

*** assumes kh-weighted pore pressure distribution across sands A-E

Table 3

Cores from Project Area Used in Study

well	core top	sand	samples
14X-34RD	11870	B2	17
"	11904	C1	2
"	12055	E1	9
"	12073	E2	5
"		shale/silt	6
22X-3	11813	A	10
"	11831	B1	17
"	11866	B2	23
"	11906	C1	8
"	11933	C2	41
"	12005	D1	21
"	12026	D2	19
"	12065	E1	31
"	12111	E2	26
"		shale/silt	9
45X-3	11725	D1	31
"	11758	D2	42
"	11803	E1	25
"	11836	E2	17
"	11860	W	10
"		shale/silt	5
65X-3	11797	B1	7
"	11805	B2	5
"	11812	C1	6
"	11818	C2	2
"	11821	D1	3
"	11824	D2	3
"	11827	E1	3
"	11830	E2	6
"	11837	W	40
"		shale/silt	1
27X-34	12253	B2	12
"	12281	C1	53
"	12336	C2	51
"		shale/silt	16
46X-34	12660	C1	15
"	12712	C2	20
"	12734	D1	9
55X-34	12098	C1	19
"	12930	C2	58
"	13003	D1	38
"	13041	D2	27
"	13073	E1	37
"	13114	E2	24
"		shale/silt	11
		TOTAL =	840

sand	samples
A	10
B1	24
B2	57
C1	103
C2	172
D1	102
D2	91
E1	105
E2	78
W	50
shale/silt	48
TOTAL =	840

sand	samples
14X-34RD	39
22X-3	205
45X-3	130
65X-3	76
27X-34	132
46X-34	44
55X-34	214
TOTAL =	840

Table 4

Porosity-Permeability Data from Conventional Core Analysis of Well 55X-34

sample	depth (ft)	sand	K (md)	Ø (%)	RQI (microns)	PR	FZI	HU	pore throat (microns)
55x34	12,908.5	C1	25	13.7	0.424	0.159	2.673	13	13.4
55x34	12,909.5	C1	27	12.9	0.455	0.148	3.069	13	16.2
55x34	12,910.5	C1	25	13.0	0.436	0.149	2.916	13	15.3
55x34	12,911.5	C1	18	18.2	0.312	0.222	1.404	11	5.5
55x34	12,912.5	C1	8	14.5	0.230	0.170	1.355	11	6.4
55x34	12,913.5	C1	19	14.5	0.360	0.170	2.121	12	10.1
55x34	12,914.5	C1	17	17.7	0.308	0.215	1.432	11	5.7
55x34	12,915.5	C1	2	12.9	0.133	0.148	0.896	10	4.7
55x34	12,916.5	C1	18	15.0	0.344	0.176	1.950	12	9.0
55x34	12,917.5	C1	9	19.2	0.220	0.238	0.925	10	3.5
55x34	12,918.5	C1	7	13.9	0.217	0.161	1.344	11	6.6
55x34	12,919.5	C1	15	13.3	0.334	0.153	2.175	12	11.2
55x34	12,920.5	C1	8	18.0	0.210	0.220	0.955	11	3.8
55x34	12,921.5	C1	8	12.6	0.251	0.144	1.742	12	9.4
55x34	12,922.5	C1	5	12.4	0.200	0.142	1.414	11	7.7
55x34	12,923.5	C1	1	11.0	0.115	0.124	0.929	10	5.7
55x34	12,924.5	C1	53	17.1	0.553	0.206	2.681	13	11.1
55x34	12,925.5	C1	46	16.8	0.520	0.202	2.574	12	10.8
55x34	12,926.5	C1	12	15.2	0.279	0.179	1.557	11	7.1
55x34	12,927.5		0.1	16.1	0.026	0.192	0.135	7	0.6
55x34	12,928.5		0.3	9.4	0.058	0.104	0.559	9	4.0
55x34	12,929.5		1	11.4	0.113	0.129	0.880	10	5.2
55x34	12,930.5	C2	10	16.1	0.248	0.192	1.290	11	5.6
55x34	12,931.5	C2	7	12.1	0.245	0.138	1.780	12	10.0
55x34	12,932.5	C2	3	16.9	0.123	0.203	0.607	10	2.5
55x34	12,933.5	C2	17	14.2	0.344	0.166	2.077	12	10.1
55x34	12,934.5	C2	19	14.5	0.360	0.170	2.121	12	10.1
55x34	12,935.5	C2	18	17.3	0.320	0.209	1.532	11	6.3
55x34	12936.5	C2	25	14.2	0.417	0.166	2.519	12	12.2
55x34	12937.5	C2	14	18.6	0.273	0.229	1.193	11	4.6
55x34	12938.5	C2	5	11.0	0.211	0.124	1.703	12	10.4
55x34	12939.5	C2	4	9.9	0.201	0.110	1.829	12	12.3
55x34	12940.5	C2	2	12.2	0.129	0.139	0.931	10	5.2
55x34	12941.5	C2	11	12.9	0.290	0.148	1.959	12	10.3
55x34	12942.5	C2	25	15.4	0.400	0.182	2.199	12	9.9
55x34	12943.5	C2	1	11.2	0.112	0.126	0.890	10	5.3
55x34	12944.5	C2	8	13.4	0.240	0.155	1.550	11	7.9
55x34	12945.5	C2	12	14.1	0.290	0.164	1.766	12	8.6
55x34	12946.5	C2	3	13.3	0.153	0.153	0.995	11	5.1
55x34	12947.5	C2	19	14.0	0.366	0.163	2.248	12	11.0
55x34	12948.5	C2	5	10.1	0.231	0.112	2.054	12	13.6
55x34	12949.5	C2	2	16.1	0.120	0.192	0.625	10	2.7
55x34	12950.5	C2	15	15.0	0.314	0.176	1.780	12	8.2
55x34	12951.5	C2	19	13.8	0.369	0.160	2.303	12	11.4
55x34	12952.5	C2	19	14.0	0.366	0.163	2.248	12	11.0
55x34	12953.5	C2	9	20.1	0.213	0.252	0.847	10	3.1
55x34	12954.5	C2	15	20.1	0.271	0.252	1.079	11	3.9
55x34	12955.5	C2	25	14.3	0.415	0.167	2.489	12	12.0
55x34	12956.5	C2	20	14.6	0.368	0.171	2.151	12	10.2
55x34	12958.5	C2	27	14.9	0.423	0.175	2.415	12	11.2

Table 4

Porosity-Permeability Data from Conventional Core Analysis of Well 55X-34

sample	depth (ft)	sand	K (md)	Ø (%)	RQI (microns)	PR	FZI	HU	pore throat (microns)
55x34	12959.5	C2	27	19.5	0.370	0.242	1.526	11	5.6
55x34	12960.5	C2	22	14.4	0.388	0.168	2.308	12	11.0
55x34	12961.5	C2	8	14.4	0.234	0.168	1.393	11	6.7
55x34	12962.5	C2	47	15.3	0.551	0.181	3.048	13	13.8
55x34	12963.5	C2	20	13.6	0.381	0.157	2.420	12	12.2
55x34	12964.5	C2	6	20.9	0.170	0.264	0.645	10	2.3
55x34	12965.5	C2	17	14.2	0.344	0.166	2.077	12	10.1
55x34	12966.5	C2	5	14.8	0.191	0.174	1.097	11	5.1
55x34	12967.5	C2	26	13.7	0.433	0.159	2.726	13	13.6
55x34	12967.5	C2	3	11.7	0.152	0.133	1.145	11	6.6
55x34	12968.5	C2	5	16.3	0.180	0.195	0.923	10	4.0
55x34	12970.5	C2	1	13.7	0.094	0.159	0.593	10	3.0
55x34	12971.5	C2	9	12.4	0.269	0.142	1.899	12	10.4
55x34	12972.5	C2	29	14.6	0.443	0.171	2.590	12	12.2
55x34	12973.5	C2	24	13.7	0.416	0.159	2.619	12	13.1
55x34	12975.5	C2	9	14.4	0.246	0.168	1.464	11	7.0
55x34	12976.5	C2	13	13.9	0.304	0.161	1.882	12	9.3
55x34	12977.5	C2	18	13.6	0.361	0.157	2.296	12	11.6
55x34	12978.5	C2	17	13.9	0.347	0.161	2.152	12	10.6
55x34	12979.5	C2	7	11.4	0.247	0.129	1.917	12	11.3
55x34	12980.5	C2	11	11.0	0.314	0.124	2.542	12	15.5
55x34	12981.5	C2	1	11.5	0.084	0.130	0.646	10	3.8
55x34	12982.5	C2	9	15.3	0.236	0.181	1.305	11	5.9
55x34	12984.5	C2	15	13.8	0.328	0.160	2.046	12	10.2
55x34	12985.5	C2	10	11.8	0.287	0.134	2.145	12	12.3
55x34	12986.5	C2	6	14.5	0.205	0.170	1.209	11	5.8
55x34	12987.5	C2	1	14.3	0.090	0.167	0.541	9	2.6
55x34	12988.5	C2	8	13.6	0.237	0.157	1.503	11	7.6
55x34	12989.5	C2	5	11.3	0.209	0.127	1.644	12	9.8
55x34	12990.5	C2	14	15.1	0.303	0.178	1.701	12	7.8
55x34	12993.5		2	12.9	0.126	0.148	0.852	10	4.5
55x34	12994.5		4	14.4	0.171	0.168	1.019	11	4.9
55x34	12995.5		3	13.2	0.154	0.152	1.011	11	5.2
55x34	12997.5		5	14.2	0.192	0.166	1.161	11	5.6
55x34	12998.5		3	15.2	0.145	0.179	0.809	10	3.7
55x34	13000.5		1	13.1	0.073	0.151	0.485	9	2.5
55x34	13003.5	D1	24	14.2	0.408	0.166	2.468	12	12.0
55x34	13004.5	D1	4	13.0	0.172	0.149	1.153	11	6.0
55x34	13005.5	D1	3	18.5	0.131	0.227	0.576	10	2.2
55x34	13006.5	D1	3	11.3	0.155	0.127	1.214	11	7.2
55x34	13007.5	D1	9	12.4	0.275	0.142	1.941	12	10.6
55x34	13008.5	D1	1	11.9	0.076	0.135	0.564	9	3.2
55x34	13009.5	D1	7	12.1	0.243	0.138	1.762	12	9.9
55x34	13010.5	D1	5	11.7	0.202	0.133	1.522	11	8.8
55x34	13011.5	D1	1	11.6	0.073	0.131	0.553	9	3.2
55x34	13012.5	D1	10	12.4	0.282	0.142	1.993	12	10.9
55x34	13013.5	D1	0.4	9.0	0.069	0.099	0.702	10	5.2
55x34	13014.5	D1	10	12.3	0.283	0.140	2.016	12	11.1
55x34	13015.5	D1	7	12.5	0.235	0.143	1.648	12	8.9
55x34	13016.5	D1	12	12.5	0.308	0.143	2.155	12	11.7

Table 4

Porosity-Permeability Data from Conventional Core Analysis of Well 55X-34

sample	depth (ft)	sand	K (md)	Ø (%)	RQI (microns)	PR	FZI	HU	pore throat (microns)
55x34	13017.5	D1	10	15.1	0.250	0.178	1.404	11	6.4
55x34	13018.5	D1	7	13.9	0.230	0.161	1.427	11	7.0
55x34	13019.5	D1	5	13.9	0.183	0.161	1.136	11	5.6
55x34	13020.5	D1	5	15.4	0.174	0.182	0.957	11	4.3
55x34	13021.5	D1	12	17.6	0.259	0.214	1.215	11	4.9
55x34	13022.5	D1	14	17.7	0.279	0.215	1.299	11	5.2
55x34	13023.5	D1	10	14.4	0.262	0.168	1.556	11	7.4
55x34	13024.5	D1	15	16.5	0.300	0.198	1.516	11	6.4
55x34	13025.5	D1	13	16.4	0.280	0.196	1.426	11	6.1
55x34	13026.5	D1	13	15.7	0.286	0.186	1.535	11	6.8
55x34	13027.5	D1	11	19.8	0.234	0.247	0.948	10	3.5
55x34	13028.5	D1	11	17.4	0.250	0.211	1.186	11	4.8
55x34	13029.5	D1	9	15.9	0.236	0.189	1.246	11	5.5
55x34	13030.5	D1	19	17.0	0.332	0.205	1.622	12	6.7
55x34	13031.5	D1	21	16.7	0.352	0.200	1.757	12	7.4
55x34	13032.5	D1	12	19.7	0.245	0.245	0.999	11	3.7
55x34	13033.5	D1	11	18.4	0.243	0.225	1.077	11	4.2
55x34	13034.5	D1	12	17.1	0.263	0.206	1.276	11	5.3
55x34	13035.5	D1	16	14.8	0.327	0.174	1.880	12	8.8
55x34	13036.5	D1	16	14.9	0.326	0.175	1.859	12	8.6
55x34	13037.5	D1	11	14.5	0.274	0.170	1.613	12	7.7
55x34	13038.5	D1	5	16.4	0.169	0.196	0.861	10	3.7
55x34	13039.5	D1	9	17.0	0.223	0.205	1.088	11	4.5
55x34	13040.5	D1	2	15.2	0.107	0.179	0.595	10	2.7
55x34	13041.5	D2	30	17.0	0.417	0.205	2.038	12	8.4
55x34	13042.5	D2	14	16.2	0.292	0.193	1.511	11	6.5
55x34	13043.5	D2	12	14.9	0.282	0.175	1.610	12	7.5
55x34	13044.5	D2	8	14.1	0.238	0.164	1.452	11	7.1
55x34	13045.5	D2	5	14.4	0.189	0.168	1.124	11	5.4
55x34	13046.5	D2	7	15.7	0.213	0.186	1.146	11	5.1
55x34	13048.5	D2	9	15.5	0.240	0.183	1.306	11	5.9
55x34	13049.5	D2	3	15.4	0.147	0.182	0.809	10	3.6
55x34	13050.5	D2	1	15.1	0.096	0.178	0.542	9	2.5
55x34	13051.5	D2	3	15.4	0.130	0.182	0.713	10	3.2
55x34	13052.5	D2	3	15.9	0.129	0.189	0.685	10	3.0
55x34	13053.5	D2	12	16.4	0.269	0.196	1.370	11	5.9
55x34	13054.5	D2	4	15.2	0.156	0.179	0.868	10	4.0
55x34	13055.5	D2	12	19.2	0.248	0.238	1.045	11	3.9
55x34	13056.5	D2	5	14.9	0.173	0.175	0.986	11	4.6
55x34	13057.5	D2	5	15.3	0.170	0.181	0.943	10	4.3
55x34	13058.5	D2	15	15.8	0.306	0.188	1.631	12	7.2
55x34	13060.5	D2	9	14.8	0.246	0.174	1.416	11	6.6
55x34	13061.5	D2	1	18.9	0.072	0.233	0.310	8	1.2
55x34	13063.5	D2	2	18.6	0.111	0.229	0.485	9	1.9
55x34	13064.5	D2	2	16.0	0.122	0.190	0.641	10	2.8
55x34	13065.5	D2	7	15.0	0.219	0.176	1.239	11	5.7
55x34	13066.5	D2	4	16.7	0.154	0.200	0.767	10	3.2
55x34	13067.5	D2	22	16.3	0.365	0.195	1.874	12	8.1
55x34	13068.5	D2	21	15.7	0.363	0.186	1.951	12	8.7
55x34	13069.5	D2	30	14.7	0.449	0.172	2.604	12	12.2

Table 4

Porosity-Permeability Data from Conventional Core Analysis of Well 55X-34

sample	depth (ft)	sand	K (md)	Ø (%)	RQI (microns)	PR	FZI	HU	pore throat (microns)
55x34	13070.5	D2	26	16.6	0.393	0.199	1.975	12	8.4
55x34	13071.5		0.3	12.8	0.050	0.147	0.344	8	1.8
55x34	13072.5		1	11.5	0.073	0.130	0.561	9	3.3
55x34	13073.5	E1	13	16.7	0.277	0.200	1.383	11	5.8
55x34	13074.5	E1	13	15.7	0.286	0.186	1.535	11	6.8
55x34	13075.5	E1	13	14.5	0.297	0.170	1.754	12	8.3
55x34	13076.5	E1	12	22.6	0.229	0.292	0.784	10	2.6
55x34	13078.5	E1	9	21.7	0.198	0.277	0.715	10	2.4
55x34	13079.5	E1	8	15.0	0.225	0.176	1.277	11	5.9
55x34	13080.5	E1	2	15.5	0.113	0.183	0.618	10	2.8
55x34	13081.5	E1	31	24.9	0.351	0.332	1.057	11	3.2
55x34	13082.5	E1	8	14.9	0.225	0.175	1.287	11	6.0
55x34	13083.5	E1	6	14.4	0.205	0.168	1.219	11	5.8
55x34	13084.5	E1	4	15.2	0.156	0.179	0.868	10	4.0
55x34	13085.5	E1	17	16.2	0.322	0.193	1.665	12	7.2
55x34	13087.5	E1	29	16.0	0.423	0.190	2.220	12	9.7
55x34	13088.5	E1	16	18.1	0.295	0.221	1.337	11	5.3
55x34	13089.5	E1	20	18.1	0.330	0.221	1.494	11	5.9
55x34	13090.5	E1	4	16.8	0.162	0.202	0.803	10	3.4
55x34	13091.5	E1	14	20.6	0.259	0.259	0.998	11	3.5
55x34	13092.5	E1	23	14.9	0.390	0.175	2.229	12	10.4
55x34	13093.5	E1	27	19.1	0.374	0.236	1.582	11	6.0
55x34	13094.5	E1	16	17.5	0.300	0.212	1.416	11	5.7
55x34	13096.5	E1	6	16.8	0.180	0.202	0.890	10	3.7
55x34	13097.5	E1	21	18.5	0.335	0.227	1.475	11	5.7
55x34	13098.5	E1	7	18.8	0.198	0.232	0.855	10	3.3
55x34	13099.5	E1	21	20.5	0.318	0.258	1.233	11	4.4
55x34	13100.5	E1	32	17.1	0.430	0.206	2.083	12	8.6
55x34	13102.5	E1	29	18.5	0.393	0.227	1.733	12	6.7
55x34	13103.5	E1	25	18.4	0.366	0.225	1.624	12	6.3
55x34	13104.5	E1	12	18.6	0.252	0.229	1.104	11	4.2
55x34	13105.5	E1	24	17.5	0.368	0.212	1.734	12	7.0
55x34	13106.5	E1	14	16.9	0.286	0.203	1.406	11	5.9
55x34	13107.5	E1	12	16.9	0.265	0.203	1.302	11	5.4
55x34	13108.5	E1	18	14.7	0.348	0.172	2.017	12	9.5
55x34	13109.5	E1	16	14.6	0.329	0.171	1.924	12	9.1
55x34	13110.5	E1	21	15.1	0.370	0.178	2.083	12	9.6
55x34	13111.5	E1	10	14.0	0.259	0.163	1.594	12	7.8
55x34	13112.5	E1	18	16.2	0.331	0.193	1.713	12	7.4
55x34	13113.5	E1	16	14.0	0.336	0.163	2.063	12	10.1
55x34	13114.5	E2	9	13.2	0.254	0.152	1.668	12	8.6
55x34	13115.5	E2	4	11.2	0.184	0.126	1.462	11	8.8
55x34	13116.5	E2	5	13.8	0.197	0.160	1.228	11	6.1
55x34	13117.5	E2	0.4	16.4	0.048	0.196	0.247	8	1.1
55x34	13118.5	E2	4	13.8	0.172	0.160	1.076	11	5.3
55x34	13119.5	E2	11	13.1	0.288	0.151	1.910	12	9.9
55x34	13120.5	E2	5	17.0	0.162	0.205	0.789	10	3.3
55x34	13121.5	E2	2	12.0	0.116	0.136	0.854	10	4.8
55x34	13123.5	E2	16	19.3	0.286	0.239	1.196	11	4.5
55x34	13124.5	E2	1	11.5	0.103	0.130	0.791	10	4.6

Table 4

Porosity-Permeability Data from Conventional Core Analysis of Well 55X-34

sample	depth (ft)	sand	K (md)	Ø (%)	RQI (microns)	PR	FZI	HU	pore throat (microns)
55x34	13125.5	E2	29	16.6	0.415	0.199	2.086	12	8.8
55x34	13126.5	E2	24	15.4	0.392	0.182	2.154	12	9.7
55x34	13127.5	E2	24	15.4	0.392	0.182	2.154	12	9.7
55x34	13130.5	E2	11	14.5	0.274	0.170	1.613	12	7.7
55x34	13131.5	E2	53	16.7	0.560	0.200	2.792	13	11.7
55x34	13132.5	E2	4	3.9	0.314	0.041	7.721	15	129.4
55x34	13133.5	E2	45	17.2	0.508	0.208	2.446	12	10.0
55x34	13134.5	E2	49	17.0	0.533	0.205	2.604	12	10.8
55x34	13135.5	E2	0.3	2.5	0.107	0.026	4.173	13	110.2
55x34	13136.5	E2	22	13.7	0.398	0.159	2.508	12	12.5
55x34	13137.5	E2	12	9.8	0.348	0.109	3.200	13	21.8
55x34	13138.5	E2	15	12.2	0.348	0.139	2.507	12	13.9
55x34	13139.5	E2	15	10.7	0.372	0.120	3.104	13	19.4
55x34	13141.5	E2	29	13.8	0.455	0.160	2.845	13	14.1

Table 5

Calculation of Pore Throat Diameters from Capillary Pressure Data

well	sample	depth (feet)	perm (md)	porosity (%)	Capillary pressure entry (psi)	Capillary pressure Sat_{50} (psi)	Capillary pressure P_{max} (psi)	core-derived pore throat diameter entry (microns)	core-derived pore throat diameter Sat_{50} (microns)	core-derived pore throat diameter P_{max} (microns)	log Berg (1975) (microns)
27X-34	12A	12,264.0	11.0	13.6	4.0	12.4	35.0	10.4	3.4	1.2	9.0
27X-34	37A	12,289.0	50.0	17.2	0.4	8.0	35.0	104.3	5.2	1.2	10.6
27X-34	41A	12,294.0	50.0	18.6	2.0	7.2	35.0	20.9	5.8	1.2	8.7
27X-34	70A	12,324.0	56.0	17.1	2.4	8.8	35.0	17.4	4.7	1.2	11.4
27X-34	73A	12,327.0	92.0	17.5	2.0	6.0	35.0	20.9	7.0	1.2	13.7
55X-34	2A	12,925.5	12.0	14.8	2.0	11.0	35.0	20.9	3.8	1.2	7.6
55X-34	4B	12,948.0	2.5	9.9	4.8	21.2	35.0	8.7	2.0	1.2	9.7
55X-34	7A	12,983.6	4.5	12.2	0.8	21.6	35.0	52.1	1.9	1.2	7.6
55X-34	9B	12,999.4	3.7	12.9	2.4	32.0	35.0	17.4	1.3	1.2	6.0
55X-34	15A	13,058.0	16.0	16.0	1.6	11.6	35.0	26.1	3.6	1.2	7.2
55X-34	16B	13,077.5	11.0	13.8	1.2	12.4	35.0	34.8	3.4	1.2	8.7
55X-34	19A	13,101.1	41.0	17.0	0.6	8.4	35.0	69.5	5.0	1.2	9.9
55X-34	21A	13,120.4	21.0	17.7	1.2	8.4	35.0	34.8	5.0	1.2	6.4
55X-34	22B	13,129.1	27.0	13.2	0.4	12.0	35.0	104.3	3.5	1.2	15.3
55X-34	23B	13,140.5	12.0	17.3	0.4	9.2	35.0	104.3	4.5	1.2	5.1
							AVERAGE =	43.1	4.0	1.2	9.1

constants for air/brine system (Mian, 1992)

interfacial tension = 72 dynes/cm

contact angle = 0 degrees

entry = capillary entry pressure

Sat_{50} = mercury saturation of 50%

P_{max} = maximum pressure applied during the analysis

Table 6

Ranges of $Log_{10}FZI$ Used to Define Hydraulic Units in Project Study Area

$log_{10}FZI$	Hydraulic Unit
-0.68 to -0.46	8
-0.46 to -0.24	9
-0.24 to -0.02	10
-0.02 to 0.20	11
0.20 to 0.42	12
0.42 to 0.64	13
0.64 to 0.86	14
0.86 to 1.08	15

Table 7

Effect of Overburden Pressure on Porosity and Permeability

			LABORATORY		5,000 PSI		REDUCTION	
well	sample	depth (feet)	perm (md)	porosity (%)	perm (md)	porosity (%)	perm (%)	porosity (%)
27x34	4	12,289.4	68.0	16.7	49.0	15.5	27.9%	7.2%
27x34	7	12,321.4	97.0	18.7	72.0	17.2	25.8%	8.0%
27x34	18B	12,373.4	19.0	19.5	14.0	17.9	26.3%	8.2%
27x34	20B	12,375.2	44.0	17.3	25.0	15.4	43.2%	11.0%
27x34	24B	12,367.3	45.0	17.0	25.0	15.0	44.4%	11.8%
55x34	1	12,909.5	11.0	14.0	6.0	12.6	45.5%	10.0%
55x34	3	12,937.5	16.0	15.2	9.4	13.8	41.3%	9.2%
55x34	5	12,957.5	13.0	15.7	7.5	14.3	42.3%	8.9%
55x34	7	12,983.6	4.9	11.9	2.4	10.9	51.0%	8.4%
55x34	8	12,991.5	4.8	13.2	2.3	12.0	52.1%	9.1%
55x34	9	12,999.4	1.7	11.5	0.7	10.4	58.8%	9.6%
55x34	13	13,037.5	6.9	12.0	1.9	11.3	72.5%	5.8%
55x34	17	13,086.6	13.0	13.5	7.3	12.6	43.8%	6.7%
55x34	22	13,128.1	1.4	9.2	1.1	8.5	21.4%	7.6%
						AVERAGE =	42.6%	8.7%

Table 8

Summary of Reservoir Characteristics of the Yowlumne Sand

PARAMETER	[1]CORE VALUE (uncompacted)	[2]CORE VALUE (compacted)	[3]LOG VALUE
average Ø	16.6%	15.2%	14.0%
Ø range in 90% of samples	9 to 21.5%	8 to 20.5%	8 to 18%
average K_a	44 md	25 md	24 md
K_a range in 90% of samples	0.4 to 105 md	0.2 to 60 md	0.8 to 65 md
from Ø, K_a data:			
average pore throat diameter (calc. from average Ø and K_a)	11 μ	12 μ	12 μ
diameter range in 90% of samples	3 to 18 μ	-	-
from capillary pressure data:			
ave. pore throat diameters (Sat_{50})	4.0 μ	-	-
ave. range of diameters (P_0 to P_{max})	<1.2 to 43 μ	-	-
entire Yowlumne reservoir:			
[4]average gross sand thickness	-	-	320 ft
[4]average net sand/gross sand	-	-	79.4%

[1] Ø and K_a measured in the lab at atmospheric pressure.

[2] calculated Ø and K_a using reductions observed under a confining pressure of 5,000 psi, a pressure analogous to burial pressures at reservoir depth.

[3] log Ø, K_a and pore throat diameter are averaged only for wells and intervals represented by the core-derived values.

[4] average of all wells in project study area

Table 9

Model Fluid Property Table Based on Black Oil Study of Sample from Well 32-3

EQUALLY SPACED FLUID PROPERTY TABLE					
Pressure psi	Oil FVF RB/STB	Gas FVF RB/STB	Solution GOR MSCF/STB	Oil Viscosity cp	Gas Viscosity cp
15	1.0825	219.246	0.00500	1.356	0.01100
315	1.1373	10.395	0.06004	1.088	0.01246
615	1.1834	5.301	0.13749	0.893	0.01365
915	1.2234	3.548	0.21494	0.758	0.01465
1215	1.2595	2.660	0.29238	0.670	0.01553
1515	1.2942	2.124	0.36983	0.615	0.01640
1815	1.3298	1.765	0.44728	0.580	0.01734
2115	1.3687	1.508	0.52473	0.551	0.01843
2415	1.4132	1.315	0.60218	0.515	0.01976
2715	1.4583	1.164	0.67962	0.485	0.02141
3015	1.5032	1.044	0.75707	0.455	0.02348
3315	1.5483	0.945	0.83452	0.425	0.02604
3615	1.5933	0.863	0.91197	0.395	0.02919
3915	1.6383	0.793	0.98942	0.365	0.03301
4215	1.6800	0.733	1.06687	0.335	0.03758
4515	1.7178	0.681	1.14431	0.305	0.04300
4815	1.7520	0.636	1.22176	0.275	0.04934
5115	1.7832	0.596	1.29921	0.245	0.05671
5415	1.8116	0.560	1.37666	0.215	0.06517
5715	1.8375	0.528	1.45411	0.185	0.07482
6015	1.8612	0.500	1.53155	0.155	0.08575
7015	1.9201	0.422	1.78971	0.105	0.13248
8015	1.9639	0.363	2.04787	0.085	0.19753

Table 10

Cost Estimate to Drill, Complete, and Equip Slant Well (M$)

	3 Fracs	2 Fracs	1 Frac	0 Fracs	Mechanical Failure
Drill	2193	2193	2193	2193	2078
Complete	1085	776	309	157	35
Equip	291	291	291	291	0
Microseismic Logging	196	130	65	0	0
Total Outlays	3765	3390	2858	2641	2113

Table 11

Slant Well Operating Expense Estimate (M$)

	Year 1	Year 2	Year 3	Year 4	Year 5	Year 6	Year 7	Year 8	Year 9	Total
Operations surveillance	269	471	480	429	423	439	456	478	335	3780
3rd party consulting and technology transfer	177	104	29	64	25	0	0	0	0	399
Company labor, burden, and overhead	263	167	163	124	172	180	189	199	104	1561
Total Project Costs	709	742	672	617	620	619	645	677	439	5740